

TUNING THE PERFORMANCE OF NANOCARBON-BASED
GAS SENSORS THROUGH NANOPARTICLE DECORATION

by

Shumao Cui

A Dissertation submitted in
Partial Fulfillment of the
Requirements for the Degree of

Doctor of Philosophy
in Engineering

at

The University of Wisconsin-Milwaukee

May 2013

ABSTRACT

TUNING THE PERFORMANCE OF NANOCARBON-BASED GAS SENSORS THROUGH NANOPARTICLE DECORATION

by

Shumao Cui

The University of Wisconsin-Milwaukee, 2013
Under the Supervision of Professor Junhong Chen

Tin dioxide (SnO_2) is a well-known gas sensing material, but it becomes sensitive only at elevated temperatures (e.g., above 200 °C). Nanoparticles (NPs) combined with nanocarbons, such as carbon nanotubes (CNTs) and graphene, form a new class of hybrid nanomaterials that can exhibit fascinating gas sensing performance due to tunable electron transfer between NPs and nanocarbons induced by gas adsorption. Indeed, sensors made of SnO_2 NPs-coated CNTs have shown outstanding room-temperature sensing performance to various gases, including those that are undetectable by either SnO_2 or CNTs alone.

The objectives of this dissertation study are to synthesize various NP-nanocarbon hybrid materials and to fabricate and characterize sensing platforms based on the resulting hybrid nanomaterials. Two simple and efficient methods have been used for the hybrid synthesis. One is a simple NP synthesis and assembly system for NP-nanocarbon hybrid nanomaterials production through combining a mini-arc plasma reactor with electrostatic force-directed assembly. The other is a simple wet-chemical method for direct fabrication of doped SnO_2 NP-decorated reduced graphene oxide (RGO) sheets. In particular, CNT/Ag NP and RGO/Ag NP hybrids have been produced for fast, sensitive, and

selective detection of NH_3 . Furthermore, a ternary hybrid of Ag NPs and SnO_2 NPs-decorated CNTs has been demonstrated and showed better sensing performance than CNT/ SnO_2 NP hybrids likely due to the enhanced gas adsorption and electron transfer. Additionally, hybrid sensors of In-doped SnO_2 NPs on RGO are shown to exhibit high selectivity to NO_2 sensing. Finally, the sensing mechanism for the NP-nanocarbon system has been extensively discussed.

Based on this study, we conclude that the sensing performance (including sensitivity, selectivity, and response time) can be fine-tuned by coating nanocarbons with carefully-selected NPs (pure or doped). An attempt has been made to compare the sensing performance of hybrids based on various types of nanocarbons (e.g., multiwalled CNTs, semiconducting single-walled CNTs, RGO). Nanocarbons with superior semiconducting properties as building blocks of hybrid nanomaterials are shown to exhibit better gas sensing performance. This study provides a scientific foundation to engineer practical room-temperature gas sensors with enhanced performance.

TABLE OF CONTENT

LIST OF FIGURES	vi
LIST OF TABLES	xii
LIST OF ABBREVIATIONS	xiii
CHAPTER 1 INTRODUCTION AND LITERATURE REVIEW	1
1.1 Introduction	1
1.2 Literature review	2
1.2.1 Literature review on gas sensors	2
1.2.2 Literature review on nanoparticles (NPs) and their synthesis methods for gas sensing applications.....	4
1.2.3 Literature review on carbon nanotubes (CNTs) for gas sensing applications	7
1.2.4 Literature review on graphene-based materials for gas sensing applications.....	12
1.2.5 Literature review on hybrid nanostructures for gas sensors	15
1.2.6 Summary and conclusions.....	17
1.2.7 Research objective and dissertation outline.....	18
CHAPTER 2 SYNTHESIS OF PURE AND BINARY NANOPARTICLES.....	20
2.1 Experimental methods	20
2.2 Results and discussion	22
2.2.1 Effect of oxygen-to-argon flow ratio ($Q_{\text{oxygen}}/Q_{\text{argon}}$)	22
2.2.2 Tungsten oxide nanoparticles and nanorods (NPs and NRs).....	24
2.2.3 Tungsten oxide and tin oxide NP mixture	30
2.2.4 Tin dioxide NPs.....	34
2.2.5 Silver NPs.....	39
2.3 Summary and conclusions.....	41
CHAPTER 3 SILVER NANOCRYSTALS–DECORATED CNTs FOR AMMONIA SENSING	42
3.1 Experimental methods	42
3.1.1 Material synthesis and characterization.....	42
3.1.2 Sensor fabrication and structural characterization.....	42
3.1.3 Ammonia sensing measurements	44
3.2 Results and discussion.....	45
3.2.1 MWCNTs/Ag hybrid ammonia sensors	45
3.2.2 SWCNTs/Ag hybrid ammonia sensors.....	55
3.3 Summary and conclusions.....	64
CHAPTER 4 TERNARY HYBRID STRUCTURES BASED ON CNTS FOR GAS SENSING	66

4.1 Experimental methods	66
4.2 Results and discussion	67
4.3 Summary and conclusions	76
CHAPTER 5 SILVER NANOPARTICLES–DECORATED REDUCED GRAPHENE OXIDE (RGO) FOR GAS SENSORS	78
5.1 Experimental methods	78
5.1.1 Preparation of RGO	78
5.1.2 Sensor fabrication and characterization	78
5.1.3 Ammonia-sensing measurement	79
5.2 Results and discussion	80
5.3 Summary and conclusions	93
CHAPTER 6 DOPED SnO ₂ NANOPARTICLES–FUNCTIONALIZED REDUCED GRAPHENE OXIDE FOR GAS SENSORS	94
6.1 Experimental methods	94
6.1.1 Synthesis of hybrids	94
6.1.2 Characterization	94
6.1.3 Gas sensor fabrication and sensing test	95
6.2 Results and discussion	96
6.3 Summary and conclusions	111
CHAPTER 7 SUMMARY AND RECOMMENDATIONS	112
7.1 Nanoparticle synthesis using mini-arc plasma	112
7.2 Silver nanoparticle–decorated CNTs for ammonia sensing	112
7.3 MWCNTs/SnO ₂ /Ag hybrid gas sensors	113
7.4 RGO/Ag NP ammonia sensors	114
7.5 Doped SnO ₂ –decorated RGO for gas sensors	115
7.6 Comparison of various nanocarbon-based materials for gas sensing	116
ACKNOWLEDGEMENT	119
REFERENCES	120

LIST OF FIGURES

Figure 1.1 (a) Schematic diagram showing how a hexagonal sheet of graphite is rolled to form a carbon nanotube. (b) An armchair nanotube and (c) A zig-zag nanotube.[68].....	8
Figure 1.2 SWCNT (top left) and MWCNT (top right) with typical transmission electron micrographs below.[70].....	9
Figure 1.3 Graphene is the basic building block of other forms of carbon; buckyballs (left), nanotubes (center), and graphite (right).[98].....	12
Figure 2.1 Schematic of a mini-arc plasma reactor for nanomaterial synthesis and the setup for subsequent assembly of as-produced nanomaterials.	21
Figure 2.2 Schematic experimental setup for SnO ₂ NP synthesis.	22
Figure 2.3 Photographs of tungsten electrodes (1/16 inch in diameter). The leftmost electrode is a polished tungsten electrode before experiment. The right four images are tungsten electrodes after experiments corresponding to samples A, B, C, and D in Table 2.1, respectively, as marked in the images.	24
Figure 2.4 SEM image, TEM images, and SAED pattern of tungsten oxide produced with $Q_{\text{oxygen}}/Q_{\text{argon}}=2.5$ (sample A in Table 2.1). (a) SEM image and (b) Bright field (BF) low magnification TEM image of as-produced tungsten oxide. The long straight edge in image (b) is the lacey carbon film support. The inset in (b) is an SAED pattern of as-produced NPs. (c) and (d) HRTEM images of tungsten oxide NP and NRs.....	26
Figure 2.5 BF low magnification TEM (a) and HRTEM (b) images of nanomaterials produced with $Q_{\text{oxygen}}/Q_{\text{argon}}=1.5$ (sample B in Table 2.1). (c) HRTEM image of tungsten oxide proto-NRs produced with parameters used for preparing sample C in Table 2.1. (d) BF low magnification TEM image, (e) SAED pattern and (f) HRTEM image of NRs produced with $Q_{\text{oxygen}}/Q_{\text{argon}}=0$ (sample D in Table 2.1). The lattice spacings in the HRTEM image and the diffraction rings in the SAED pattern are consistent with W ₁₈ O ₄₉	29
Figure 2.6 BF low magnification TEM image (a), SAED pattern (b), and HRTEM images (c, d) of tungsten oxide and tin oxide NP mixture. The parameters used here are equivalent to those for sample A in Table 2.1 ($Q_{\text{oxygen}}=5$ lpm, $Q_{\text{argon}}=2$ lpm ($Q_{\text{oxygen}}/Q_{\text{argon}}=2.5$)), current of 38 A and 5 min collection time. (e) is the EDS spectrum of NPs shown in image (a), where C and Cu are from TEM grid, and Al is from the TEM grid holder. 31	31

Figure 2.7 BF low magnification TEM image (a), and HRTEM image (b) of NPs synthesized with $Q_{\text{oxygen}}=5$ lpm and $Q_{\text{argon}}=5$ lpm ($Q_{\text{oxygen}}/Q_{\text{argon}}=1$). The upper electrode is tungsten and the precursor is tin. The inset in (a) is the SAED pattern.	32
Figure 2.8 (a) low magnification TEM image of tin oxide NPs prepared from pure tin with $Q_{\text{oxygen}}=3$ lpm and $Q_{\text{argon}}=2$ lpm. The current was 25A. (b) SAED pattern of the tin oxide NP clusters shown in (a).	34
Figure 2.9 (a) and (b) are low magnification TEM images of tin oxide NPs prepared from SnO. The flow rates are $Q_{\text{oxygen}}=3$ lpm and $Q_{\text{argon}}=2$ lpm with a current of 25 A. (c) and (d) are SAED patterns of the particle clusters at the edge and the particles on the carbon film respectively. After annealing in Ar (1 lpm) with 400 °C for 1 h, those SAED patterns turned into (e) and (f). After another annealing in oxygen (1 lpm) with 400 °C for 1 h, they changed to (g) and (h), respectively. (i) and (j) are SAED patterns of another sample prepared with same parameters but annealed in Ar (1 lpm) with 400 °C for 2 h to illustrate the oxygen effect.	37
Figure 2.10 (a-d) are SAED patterns evolution of SnO ₂ NPs synthesized by modified mini-arc plasma method with different furnace temperature. (e) and (f) are TEM and HRTEM images of SnO ₂ NPs synthesized with 900 °C of furnace temperature.	39
Figure 2.11 Low magnification TEM image (a) and SAED pattern (b) of as-produced Ag NPs. (c), and (d) HRTEM images of Ag NPs. In the synthesis process, the flow rates are $Q_{\text{oxygen}}=0$ lpm and $Q_{\text{argon}}=3$ lpm with a current of 40 A.	40
Figure 3.1 Schematic experimental setup for sensing measurements.	44
Figure 3.2 (a) SEM image of a single MWCNT decorated with Ag NCs connecting two gold electrode fingers. (b) SEM image of the enlarged view of the MWCNT/Ag NP structure as marked in (a). (c) TEM image of MWCNT/Ag NP hybrid structures. The inset is an SAED pattern of the hybrid demonstrating Ag crystallinity. (d) HRTEM image of MWCNT/Ag NP hybrid nanostructures. The inset is the enlarged view of Ag structure as marked on the Ag NC.	46
Figure 3.3 (a) <i>I-V</i> characteristics of MWCNTs before and after Ag NPs decoration. (b) <i>I-V</i> characteristics of MWCNT/Ag NP hybrid sensors in airflow and in 1% NH ₃ flow. (c) The room temperature dynamic sensing response ($\Delta R/R$) before and after Ag NPs decoration. (d) Five sensing cycles of the MWCNT/Ag NP hybrid sensor to 1% NH ₃ , indicating a good stability.	49
Figure 3.4 (a) The dynamic response ($\Delta R/R$) of the MWCNT/Ag NP hybrid sensor when exposed to different concentrations (C) of NH ₃ . (b) Curve fit of the sensor response ($\Delta R/R$) as a function of NH ₃ concentration. The inset is a linear fitting of 1/S ($R/\Delta R$) vs. 1/C.	52

Figure 3.5 Comparison of sensing response to various gases.	53
Figure 3.6 Comparison of sensing performance toward 1% NH ₃ before and after four-month storage in air.	54
Figure 3.7 The dynamic sensing response of MWCNT/Ag NP hybrid sensor after four-month storage in air when exposed to different concentrations of NH ₃ . The concentration unit of NH ₃ is parts per million (ppm).	55
Figure 3.8 (a) SEM image of SWCNTs bridging a gold electrode gap and (b) HRTEM image of SWCNTs.	56
Figure 3.9 (a) <i>I</i> - <i>V</i> and (b) FET characteristics of bare SWCNTs.	56
Figure 3.10 SEM images of SWCNTs before (a) and after (b) Ag NPs deposition.	58
Figure 3.11 (a) Room-temperature dynamic sensing responses of SWCNTs before and after Ag NPs decoration when exposed to 1% NH ₃ . (b) Dynamic sensing response to 1% NH ₃ for bare SWCNTs sensor with low SWCNT loading density.	58
Figure 3.12 SEM images of SWCNTs coated with different loadings of Ag NPs: (a) low loading with 5-min deposition of Ag NPs and (b) high loading with 15-min deposition of Ag NPs.	61
Figure 3.13 (a) Dynamic sensing evolution of SWCNTs with different Ag NP loadings. (b) 3-cycle sensing performance of SWCNT/Ag hybrids with Ag NPs deposition time of 15 min.	61
Figure 3.14 SEM images of SWCNTs between a gold electrode gap before (a) and after (b) SnO ₂ NPs deposition.	63
Figure 3.15 Room-temperature dynamic sensing evolution of SWCNTs before and after SnO ₂ NPs decoration to (a) 1% NH ₃ and (b) 100 ppm NO ₂ . Dynamic sensing response of (c) bare SWCNTs and (d) SWCNT/SnO ₂ hybrids to 100 ppm CO and 1% H ₂	64
Figure 4.1 Schematic view of a device used for conductometric measurements. (b) and (c) are SEM images showing MWCNTs which are bridging two gold electrodes before and after NPs assembly, respectively. (d) is the EDS spectrum of the hybrid structure. Al and Si are from test support stage and Si wafer, and carbon is from the CNT. (e) and (f) are HRTEM image and SAED pattern of MWCNTs coated with both SnO ₂ and Ag NPs.	68
Figure 4.2 <i>I</i> - <i>V</i> curve evolution of MWCNTs at different conditions (with and without NP coating). (b) The dependence of current on gate voltage.	69

Figure 4.3 Sensing responses for bare MWCNTs and MWCNTs with partially covered NPs to (a) 100 ppm NO ₂ and (b) 1% NH ₃ at room temperature.	70
Figure 4.4 Representative sensing response of MWCNTs/SnO ₂ /Ag hybrid structures to 100 ppm NO ₂ at room temperature.	72
Figure 4.5 (a) SEM image of MWCNTs coated with Ag NPs. Inset is an SEM image showing the hybrid structure bridging two gold electrodes. (b) <i>I-V</i> characteristics of MWCNTs and MWCNTs/Ag. (c) and (d) are sensing responses of bare MWCNTs and MWCNTs/Ag structures to 100 ppm NO ₂ and 1% NH ₃ at room temperature, respectively.	73
Figure 4.6 SEM image of MWCNTs with full surface coverage of SnO ₂ NPs.	75
Figure 4.7 <i>I-V</i> curve evolution of the control sample, which was obtained by first coating MWCNTs with SnO ₂ NPs at a high coverage followed by additional coating of Ag NPs.	75
Figure 4.8 Sensing responses of a control sample at room temperature to (a) 1,250 ppm NO ₂ and (b) 1% NH ₃ . For the control sample, MWCNTs were first coated with SnO ₂ NPs at a high coverage and then coated with Ag NPs.	76
Figure 5.1 Schematic illustration of the process to fabricate RGO/Ag hybrid sensor devices and the subsequent sensing measurements.	80
Figure 5.2 (a, b) SEM images of an RGO flake before and after Ag NP deposition bridging a pair of gold electrode fingers. (c) TEM image of an RGO flake decorated with Ag NPs. The inset is an SAED pattern of RGO/Ag hybrids. (d) HRTEM image of RGO/Ag hybrids.	81
Figure 5.3 (a) XPS spectra of RGO/Ag hybrids. (b) High-resolution XPS spectra of Ag 3d from RGO/Ag hybrids.	82
Figure 5.4 Raman spectra of RGO and RGO/Ag hybrids.	83
Figure 5.5 (a) <i>I-V</i> characteristic of RGO/Ag hybrids on gold electrodes and the inset is the FET measurement of the sensor device. (b) The room-temperature dynamic-sensing responses of RGO before and after Ag NP deposition. (c) Dynamic responses of RGO/Ag hybrids when exposed to different concentrations of NH ₃ . (d) Five-cycle responses of RGO/Ag to 1% NH ₃ , indicating a good stability of the sensor.	85
Figure 5.6 FET measurement of pure RGO.	86
Figure 5.7 SEM images of RGO coated with different loadings of Ag NPs.	88

Figure 5.8 Dynamic sensing evolution of RGO/Ag NP hybrids with different Ag NP loadings on the RGO.....	89
Figure 5.9 SEM images of Ag NPs on a gold electrode with deposition time of 1h. Electrical test showed the circuit was still open.....	90
Figure 5.10 Dynamic sensing responses of RGO to NO ₂ before and after Ag NP deposition. (b) Five-cycle sensing behavior of RGO/Ag hybrids followed by the first cycle in (a). (c, d) First cycle and the subsequent five-cycle sensing response, respectively, for another RGO/Ag sample with the same Ag NP loading (15 min deposition).	91
Figure 5.11 Dynamic sensing response to 1% NH ₃ for another RGO/Ag hybrid sensor.	92
Figure 6.1 Schematic illustration for the preparation process of RGO-IDTO nanohybrids.	97
Figure 6.2 (a, b) SEM images of RGO-IDTO. (c, d) TEM images of RGO-IDTO nanohybrids. The inset in image (d) is the SAED pattern of RGO-IDTO. The rings marked with red arcs are indexed to rutile SnO ₂ , and the rings marked with green arc are indexed to graphene. (e) HRTEM image of RGO-IDTO nanohybrids. (f) EDS spectra of RGO-IDTO. Cu and Al are from the sample holder.	98
Figure 6.3 (a, c) low magnification TEM images of RGO-RDITO nanohybrids. (b) SAED pattern indexed to rutile SnO ₂ and G. (d) HRTEM image of RGO-RDITO nanohybrids. (e) EDS spectrum of RGO-RDITO nanohybrids.....	99
Figure 6.4 (a) XRD patterns of RGO-SnO ₂ and RGO-IDTO nanohybrids. (b) XPS spectra of GO, RGO-SnO ₂ , and RGO-IDTO nanohybrids. (c-e) High-resolution XPS spectra of C 1s (c), Sn 3d (d), and In 3d (e) of the RGO-IDTO nanohybrids. (f) Raman spectra of GO and RGO-IDTO nanohybrids.....	101
Figure 6.5 XRD pattern of RGO-RDITO nanohybrids.....	101
Figure 6.6 TEM image (a) and SAED pattern (b) of product prepared by reducing SnCl ₄ on GO using NaBH ₄ and the same procedure for preparing RGO-IDTO nanohybrids.....	104
Figure 6.7 TEM images and SAED patterns of RGO-IDTO nanohybrids prepared with In/Sn=1:1 (a, b), 0.5:1 (c, d), 0.3:1 (e, f), respectively.	104
Figure 6.8 TEM image of nanohybrids prepared by adding Sn into the GO dispersion followed by adding In.....	105
Figure 6.9 TEM images of RGO-RDITO nanohybrids prepared with different amounts of Ru by adding different amounts of RuCl ₃ (0.05 M) solutions (e.g., 1.5 ml, 1.0 ml and 0.5 ml) into 8 mg GO dispersion, while adding the same amount of SnCl ₄	106

Figure 6.10 (a,b) Dynamic sensing response of RGO-IDTO toward different NO_2 concentrations.
(c) Exponential curve of sensitivity as a function of NO_2 concentration. (d) Sensitivity comparison of RGO-IDTO and RGO-SnO₂ nanohybrids to 100 ppm NO_2 109

Figure 6.11 Comparison of sensing responses (a) and sensitivity (b) to various gases..... 110

LIST OF TABLES

Table 2.1 Reactor parameters for preparation of tungsten oxide samples. Same gas flow parameters were used for synthesis of mixed metal oxide samples with addition of Sn precursor, and for tin oxide samples with Sn or SnO precursors and with C-C electrodes.....	23
Table 7.1 Summary of sensitivity, selectivity and response time for various nanocarbon-based materials	117

LIST OF ABBREVIATIONS

0D	zero-dimensional
1D	one-dimensional
2D	two-dimensional
3D	three-dimensional
BFTEM	bright field transmission electron microscope
CNTs	carbon nanotubes
CVD	chemical vapor deposition
DFT	density functional theory
DMF	<i>N,N</i> -Dimethylformamide
EDS	energy-dispersive X-ray spectroscope
ESFDA	electrostatic force-directed assembly
FET	field-effect transistor
G_0	sensor conductance in dry air
ΔG	conductance change before and after test gas exposure
GNR	graphene nanoribbon
GO	graphene oxide
HOPG	highly oriented pyrolytic graphite
HRTEM	high-resolution transmission electron microscope
lpm	liter per minute
MWCNTs	multiwalled carbon nanotubes
NCs	nanocrystals

NPs	nanoparticles
NRs	nanorods
Q_{oxygen}	oxygen flow rate
Q_{argon}	argon flow rate
QDs	quantum dots
R	average sensor resistance in air before test gas exposure
R_g	sensor resistance after exposure to a test gas
RGO	reduced graphene oxide
S	sensor sensitivity
SAED	selected area electron diffraction
SB	Schottky barrier
SEM	scanning electron microscope
SL	sensor selectivity
SWCNTs	single-walled carbon nanotubes
s-SWCNTs	semiconducting single-walled carbon nanotubes
t	response time
TCEs	transparent conductive electrodes
TEM	transmission electron microscope
TIG	tungsten inert gas
VS	vapor-solid
VLS	vapor-liquid-solid
XRD	X-ray diffraction

CHAPTER 1 INTRODUCTION AND LITERATURE REVIEW

1.1 Introduction

Metal oxides (e.g., SnO₂) are attractive for low-cost chemo-resistive gas sensors and have been widely used in various gas sensing applications. These metal oxide sensors typically are sensitive with inadequate selectivity to various gases (e.g., NO₂, NH₃, O₂, and ethanol). However, metal oxide gas sensors are usually operated at elevated temperatures to register sufficient sensitivity, which significantly limits their practical applications. For example, H₂ is a flammable gas and the detection process should avoid high temperatures.

Carbon nanotubes (CNTs) of unique one-dimensional (1D) structure and huge specific surface area have been demonstrated for room-temperature gas sensors; however, the carbon-carbon bonds in CNTs are chemically stable and the interaction between pristine CNTs and gas molecules is relatively weak, resulting in limited sensitivity and poor selectivity of pristine CNT gas sensors. Graphene is attracting growing interests for gas sensing due to its unique structure and intrinsic properties. It was found that graphene is sensitive to gas adsorption on its surface and potentially can be used as gas sensors because of its high specific surface area and high charge carrier mobility. Unfortunately, graphene has the same carbon-carbon bonds as CNTs and its interaction with gas molecules is also weak. Fortunately, nanoparticles (NPs)-decorated CNTs or graphene hybrids have been reported to show good sensing performance at room temperature. These NPs could serve as additional active sites on the nanocarbon surface to adsorb target gas molecules and thus modify the electrical conductance of nanocarbons due to

electron transfer induced by the gas adsorption. In some cases, the NPs could not only enhance the sensitivity but also improve the selectivity and response time due to the specific interaction between the NPs and gas molecules, suggesting NP decoration can tune the sensing performance of nanocarbon-based gas sensors. In this dissertation, various NP-decorated nanocarbon hybrids have been synthesized and integrated into gas sensors to illustrate such a concept.

1.2 Literature review

1.2.1 Literature review on gas sensors

With the development of industry and human activity, air pollution becomes a serious problem. Hazardous gases, such as NO_2 , NH_3 , CO , H_2S , and SO_2 , have harmful effects on humans, animals, and plants. Therefore, development of highly sensitive gas sensors for detecting harmful gases is extremely important in improving environmental quality and protecting humans from exposure to dangerous gases. Gas sensor is a device that transforms gas information (gas composition and concentration) into an analytically useful signal. According to the operation principle, gas sensors can be classified into several types: (1) Thermometric gas sensor,[1] which measures the heat effect of a physical gas mixing or a gaseous chemical reaction. (2) Magnetic gas sensor, which measures the change of paramagnetic properties of an analyzed gas.[2] (3) Mass sensitive gas sensor, which transforms the mass change on a specially modified surface into a change in the property of the support material. The mass change is caused by

accumulation of gas molecules. Generally, mass sensitive gas sensors can be divided into two subtypes: (a) Piezoelectric gas sensor, which measures the frequency change of the quartz oscillator plate caused by adsorption of target gases at the oscillator.[3] (b) Surface acoustic wave gas sensor is based on the change of propagation parameter of a generated acoustic wave affected by gas adsorption on the working surface of a delay line or a resonator.[4] (4) Conductivity gas sensors, which are based on a change in the electrical resistance of the sensing material resulting from interaction with a gas.[5-8] Conducting polymer and metal oxide semiconductor are two commonly used sensing materials in conductivity gas sensors.[9-12] (5) Optical gas sensor measures the changes in optical properties, such as intensity change, spectrum change, lifetime change or wavelength shift, which result from the interaction between gas molecules and the sensing material.[13, 14]

Conductivity gas sensor is a dominant sensor type commonly used for various applications. And metal oxide (e.g., SnO_2 , ZnO) is a commonly used sensing material in a conductivity gas sensor due to its relatively low cost. SnO_2 is the most widely studied material among all oxides for gas sensing applications [15] because SnO_2 is sensitive to a wide range of gases. Other popular sensing materials include ZnO , TiO_2 , WO_3 , In_2O_3 , Fe_2O_3 , CuO , NiO , GeO_2 , Ga_2O_3 , and V_2O_5 . According to the principle of gas sensitivity, metal oxides can often be divided into bulk-sensitive and surface-sensitive materials. For example, the conductivity of TiO_2 increases due to the formation of bulk oxygen vacancies under reducing conditions and thus is categorized as a bulk-sensitive gas sensing material. Although bulk defects affect its conductivity, SnO_2 belongs to the category of surface-sensitive material. The conduction band with its minimum at the

Γ -point and the high mobility of charge carriers can lead to a significant change in the electrical conductivity of the material due to the change in charge carrier concentrations. Therefore, gas adsorption-induced band bending has the potential to result in strong conductivity changes in SnO₂ and thus triggers a gas response signal. In contrast, TiO₂ has an indirect band gap and its conduction band minimum is not at the Γ -point. Consequently, band bending does not dramatically affect the conductivity of TiO₂. [16]

In recent years, nanomaterials have been drawing tremendous attention due to their large surface-to-volume ratio and quantum size effect. Various applications have been developed based on nanomaterials, such as catalysis, [17] solar cells, [18] biosensors, [19] gas sensors, [20] and electronic and optoelectronic devices. [21] Among these applications, gas sensing is an important one. Due to the high surface-to-volume ratio, nanosensors normally exhibit a higher sensitivity than their traditional counterparts. For gas sensors, the well-known “3S” performance criteria are sensitivity, selectivity, and stability. Related research has concentrated on various nanostructures, such as nanoparticles, [22, 23] nanorods, [10] nanowires, [24, 25] nanobelts, [26] nanotubes, [27, 28] nanosheets, [29] nanocubes, [30] nanospheres, [31] and nanoflowers. [32] In addition, gas sensors based on nanomaterials are much smaller than those using bulk materials, leading to low cost, low energy consuming, and high sensitivity.

1.2.2 Literature review on nanoparticles (NPs) and their synthesis methods for gas sensing applications

Nanoparticles are defined as a collection of atoms or molecules binding together forming

a particle with a radius of 1–100 nm. Nanomaterials can be divided into different categories by the number of dimensions. NPs are considered as 0-dimensional (0D) nanomaterials; nanotubes, nanowires and nanorods are classified as 1D nanomaterials and 2D nanomaterials refer to nanosheets (e.g., graphene). Although NPs are considered as a modern discovery, they have already been used in ancient time. For example, Au NPs were used in pigment for ruby colored glass in 17th century.[33] In the past decades, NPs have attracted huge interest due to their potential novel properties offered by their size effect. Various applications were developed based on NPs, such as catalysis,[34] solar cell,[35] gas sensor,[36, 37] biosensor,[38] and drug delivery.[39] Many technologies have been developed to synthesize NPs, including spray pyrolysis,[40] hydrothermal methods,[41] pulsed laser deposition,[42] sputtering,[43] flame method,[44, 45] and thermal deposition.[46]

Wet-chemical method is widely used in materials preparation due to its capability to produce NPs with well-controlled shape, size, and structure. Zheng *et al.* developed a general strategy to synthesize oxide-supported metal NPs as catalysts.[47] Besides the versatility, the method could offer facile control over metal NP properties, such as particle size, particle distribution, and particle loading. Wei *et al.* reported a new wet-chemical route to synthesize FeCo nanocubes.[48] The shape can be controlled by controlling the concentration of the reaction agent and the reaction time. Lu *et al.* successfully prepared core-shell structures of iron oxide NPs uniformly coated with amorphous silica using a sol-gel approach.[49] The coating thickness of silica can be well controlled by changing the concentration of the sol-gel solution. However, NPs maybe contaminated with the

reaction agents and in some studies with toxic chemicals used in the synthesis.

Preparing nanomaterials in dry and clean gaseous surroundings can potentially minimize the sample contamination in contrast to wet-chemical routes. Among various gas-phase processes, the arc plasma method is a useful method for nanomaterial synthesis. High temperature dc arc discharge technique has led to the discovery of fullerene and carbon nanotubes.[50, 51] Besides carbon nanomaterials, arc plasma techniques also have demonstrated potential in synthesizing other metal and metal oxide NPs, such as Sn-Ag mixture,[52] Cu,[53] Au,[54] Al₂O₃,[55] and TiO₂. [56] Less research has been conducted for the growth of 1D nanomaterials using plasma methods. Cvelbar *et al.* synthesized Fe₂O₃ nanowires and nanobelts through oxygen plasma oxidation of bulk iron.[57] Ono *et al.* grew ZnO nanowires in the O₂/Ar plasma with Zn as a source.[58] For NP synthesis, most of the arcs used are transferred arcs as they are effective in producing crystalline nanomaterials by offering high temperature and high quenching rate.

The small size of NPs increases the surface-to-volume ratio, leading to many more atoms sitting on the particle surface and higher activity than larger particles having the same mass. This is a huge advantage for sensor applications. For metal oxide gas sensors, the crystal size is very important to the sensing properties. When the crystal size becomes twice of the Debye length, the space charge region will spread to the entire crystal, leading to high sensitivity to gases, which has been proved by Ogawa *et al.*[59] For example, the sensitivity of tin oxide NPs increases dramatically when the particle sized is reduced to 6 nm. Various NPs have been developed for gas sensor applications. For example, WO₃ NPs were synthesized to detect ethanol and H₂S gases with a lower

detection limit of 200 ppb for ethanol and 20 ppb for H₂S.[60] ZnO NP-based gas sensors have been shown high sensitivity and fast response to NO₂. Lu *et al.* synthesized SnO₂ NPs as small as 5 nm using a mini-arc plasma method;[37] the resulting SnO₂ NP sensor showed fast response and high sensitivity to ethanol vapor.

Another way to improve the characteristics of semiconductor NPs for gas sensing application is introducing dopants in the sensing material. It was revealed that dopants, such as Cu, Fe, Cr, Co, and Al, can enhance the surface-to-volume ratio of doped NPs by decreasing the size and changing the shape.[61, 62] Meanwhile, dopants also can decrease the band gap of metal oxides due to red shift of the band gap.[63] Usually, non-stoichiometric oxide has more oxygen vacancies, leading to a semiconducting nature. Literature has reported on most popular semiconductor SnO₂ doped with various metals including Fe,[64] Pt,[65] Ni,[61] Pd,[65] Cu,[66] and Ru.[67] Those doped SnO₂ nanomaterials were produced by thermal evaporation techniques or wet-chemical methods.

1.2.3 Literature review on carbon nanotubes (CNTs) for gas sensing applications

A carbon nanotube (CNT) can be visualized as a hollow cylinder which is formed by rolling up a sheet of graphite. CNTs were first discovered by Iijima in 1991 in fullerene soot.[50] The atomic structure of carbon nanotube can be described in terms of tube chirality, which is defined as the chiral vector (C_h) and the chiral angle (θ) as shown in Figure 1.1a.[68] The roll-up vector (C_h) depends on two parameters, n and m , which are

the number of steps along the zig-zag carbon bonds of the hexagonal lattice, and vector a_1 and a_2 are unit vectors. Two limiting cases are referred as arm-chair ($\theta=30^\circ$) nanotube (Figure 1.1b) and zig-zag ($\theta=0^\circ$) nanotube (Figure 1.1c). Combined with chiral vectors, zig-zag nanotube is $(n, 0)$, and arm-chair nanotube is (n, n) . The chirality has a significant

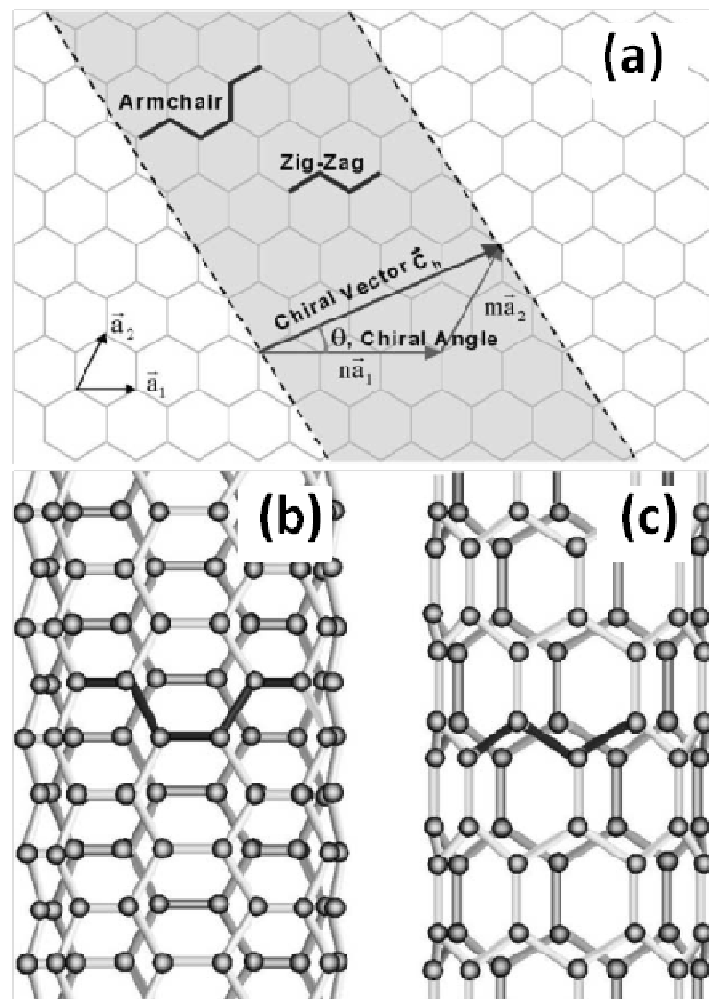


Figure 1.1 (a) Schematic diagram showing how a hexagonal sheet of graphite is rolled to form a carbon nanotube. (b) An armchair nanotube and (c) A zig-zag nanotube.[68]

effect on the property of CNTs. Considering electrical property of a CNT, it can be either metallic or semiconducting depending on the chirality.[69] There are two main types of

CNTs, single-walled carbon nanotube (SWCNT) and multiwalled carbon nanotube (MWCNT) (Figure 1.2).[70] A SWCNT can be considered as a single sheet of graphite rolled up into a hollow cylinder. Meanwhile, MWCNT is much larger and consists of many SWCNTs nested concentrically. The diameter and length of CNTs vary with different synthetic methods. The length is generally dependent on the growth time, but typically is tens of microns. The diameter of SWCNTs is between 0.7 and 3 nm.[71] For MWCNTs, the diameter ranges from 10 to 200 nm.[72]

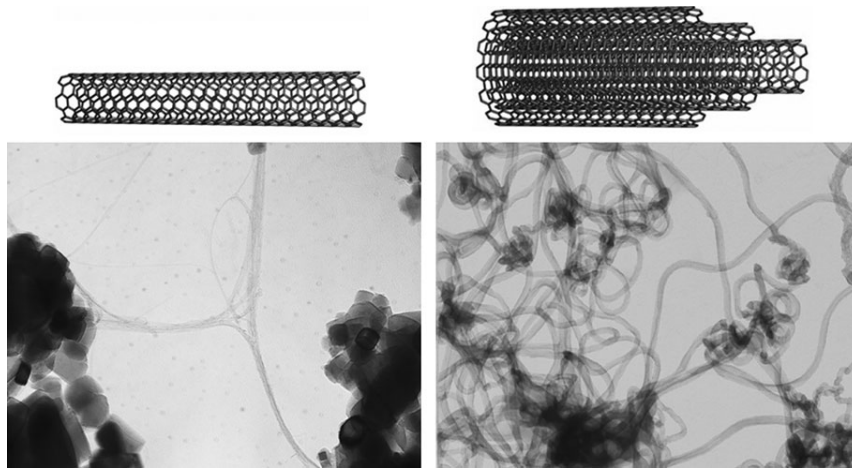


Figure 1.2 SWCNT (top left) and MWCNT (top right) with typical transmission electron micrographs below.[70]

There are three commonly used methods to synthesize CNTs: arc discharge, laser ablation, and chemical vapor deposition (CVD). The first method used to fabricate CNTs was arc discharge. In this method an electric arc discharge is generated between two graphite electrodes under inert atmosphere of helium or argon. A very high temperature is obtained to allow the sublimation of the carbon. In 1991, Iijima reported the preparation of MWCNTs in the course of preparing fullerene, in which the method used was arc

discharge.[50] Later it was found that addition of metal catalyst on one of the electrode produced SWCNTs.[73, 74] Laser ablation is the second method that can produce high quality and high purity CNTs.[75] In this method, a piece of graphite is vaporized by laser irradiation under an inert atmosphere. This will produce nanotubes containing soot on the walls of a quartz tube.[76, 77] After the production, purification by gasification is needed to eliminate the amorphous carbonaceous materials. Both arc discharge and laser ablation methods have the advantage of making high yield SWCNTs (> 70%), but there are also two disadvantages. One is that they need to evaporate carbon atoms from solid state source at a very high temperature (> 3,000 °C). The other is that nanotubes are tangled together which limits their applications. Then, CVD method appeared as a promising approach to prepare CNTs with large scale and ordered production.[78-80] In this process, a layer of metal catalyst, commonly nickel, cobalt, or iron, was deposited on the substrate. Then, a mixture gas (acetylene, methane, or ethylene and nitrogen) was introduced into the reaction chamber. After chemical reactions, nanotubes formed on the substrate through the decomposition of hydrocarbons at 700–900 °C and atmospheric pressure.

CNTs have unique electrical, chemical, and mechanical properties due to their particular 1D structure. CNT can be a good conductor with very low resistance, and their emission properties are far superior to traditional carbon emitters. Theoretical experiments showed that CNTs can carry current 1,000 times higher than copper wires.[81] So it can be used as CNT-based field emitters.[82] Other electronic properties of CNTs also have been exploited as chemically sensitive materials, including gases [83,

84] and proteins,[85] which are gas sensors and biosensors, respectively. Additionally, supercapacitor and hydrogen storage are two potential practical applications of CNTs.[86, 87] CNTs exhibit good mechanical properties as well. They are expected to have high stiffness and high strength owing to the strong carbon-carbon sp^2 bonding.[88] Theoretical and experimental results prove that the strength of CNTs can be 10–100 times higher than the strongest steel at a fraction of steel weight.[68] CNTs also have good thermal and optical properties. Given the properties of pure CNTs, composite based on CNTs is a new class of material. Through the combination with polymers, metals or metal oxides, electrical properties of CNT composites are significantly improved.

Gas sensor is one of the important applications of CNTs. CNTs are promising gas sensing materials because of two main aspects. One is that their thin 1D nanostructure makes them highly sensitive to very tiny external perturbation. The other is their huge specific surface area. Gas molecules adsorb on the CNT surface and act as dopants, which shift the Fermi level of the nanotube or change the band structure of the tube due to the orbital hybridizations for bond formation, thus influencing the conductivity of CNTs.[89] Many experiments have shown the evidence of CNT sensing to various gases, such as O_2 ,[90, 91] NO_2 ,[92] N_2 ,[83] NH_3 . [91] To enhance the sensing performance of CNTs, hybrid structures based on CNTs were developed. For example, CNTs were coated with polymer or decorated with metal oxide NPs to enhance the sensing performance.[68, 93] Investigations have shown that metallic or semiconductor crystals can interact with CNTs and reorganize electron distribution, which finally influence the conductivity change during exposure to gases.[94-96]

1.2.4 Literature review on graphene-based materials for gas sensing applications

Graphene is a single atomic carbon layer with a honeycomb structure. In 2004, Novoselov *et al.* demonstrated a simple method of mechanically extracting single- and few-layer graphene from graphite.[97] They also showed how to use the graphene in devices and measured the transport properties of graphene. Six years later in 2010, they received the Nobel Prize in physics for the work. Since this groundbreaking work on graphene, research in graphene has grown very rapidly. According to the Web of Knowledge, the paper by Novoselov *et al.* has been cited for 13,284 times (accessed by April, 20 2013), which indicates the level of interest in graphene research. In fact, graphene could be regarded as a building block of several other carbon nanomaterials, such as buckyballs (quasi 0D), CNTs (1D), and graphite (3D) as shown in Figure 1.3.[98]

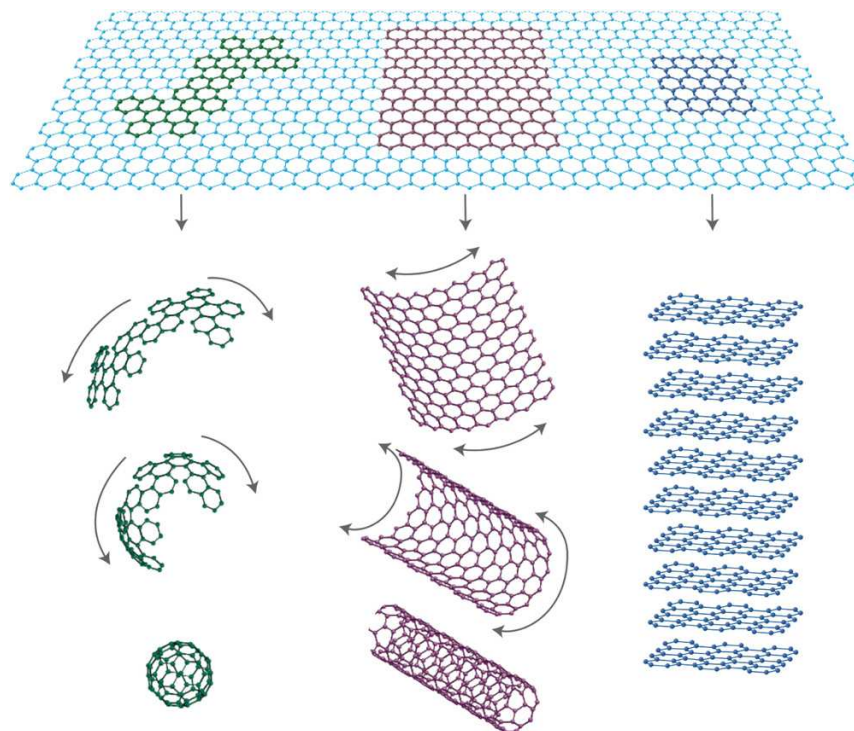


Figure 1.3 Graphene is the basic building block of other forms of carbon; buckyballs (left), nanotubes (center), and graphite (right).[98]

Various methods have been developed to synthesize graphene and graphene-based materials, such as graphene oxide (GO) and reduced graphene oxide (RGO). There are challenges in preparing pure and homogeneously dispersed single-layer graphene in solvents. For example, a key challenge is the aggregation of graphene. Because graphene has high surface area and is hydrophobic, it tends to aggregate into graphite in some solvents. Therefore, prevention of aggregation is critical because most of the unique properties are from the unique single-layer structure. Among those methods, three of them are commonly used. The first one is mechanical exfoliation of graphite to obtain pristine 2D graphene by using adhesive tapes.[97] This method is just a simple peeling process using a scotch tape from highly oriented pyrolytic graphite (HOPG). It was found that the peeled flakes consisted of monolayer and few-layer graphene. The second method is chemical vapor deposition (CVD) which can grow single-layer or few-layer graphene on metal surfaces, such as Ni and Cu.[99-102] Graphene also can be grown on carbon-containing substrates such as SiC.[103] However, oxidation and exfoliation of graphite oxide, followed by chemical reduction, is an effective method to prepare large quantities of graphene at a low cost. RGO is usually prepared by this route.[104] GO has a structure of graphene basal plane decorated with oxygen-containing functional groups such as hydroxyl and epoxy (1,2-ether) groups. For synthesis of GO, Hummers method is the most popular one because of its relatively short reaction time and absence of harmful chemicals such as ClO_2 . [105] Graphene itself is a semimetal.[106] In order to improve the on-off current ratio of transistors based on graphene, graphene with narrow width was synthesized, which was termed as graphene nanoribbon (GNR). It was reported that GNR

with a width less than 10 nm exhibits semiconducting behavior and the on-off current ratio of GNR-based field-effect transistors (FETs) could reach about 10^7 at room temperature.[107]

In the past few years, many exciting properties of graphene were discovered. For example, it has a large specific surface area ($2,630 \text{ m}^2\text{g}^{-1}$) and extremely high carrier mobility ($200,000 \text{ cm}^2\text{V}^{-1}\text{s}^{-1}$).[108, 109] The thermal conductivity of graphene is as high as $5,000 \text{ Wm}^{-1}\text{K}^{-1}$. [110] It only absorbs 2.3% of visible light, which means it has high light transmittance. Therefore, graphene can be used to fabricate transparent conductive electrodes (TCEs) because of its high conductivity and light transmittance.[111] These TCEs can be used in solar cells and many other optoelectronic devices.[112] Because of the large specific surface area and high carrier mobility, graphene and RGO are promising for gas sensors and biosensors.[113, 114] Due to the unique band structure, graphene FET has been synthesized and investigated. For example, a graphene FET operated at a frequency up to 26 GHz has been reported.[115] Besides, various composites have been synthesized based on graphene.[116, 117] For instance, it was reported that Mn_3O_4 /graphene hybrid delivers a high capacity as anode materials for lithium-ion batteries.[118]

RGO is promising for gas sensor applications because there are functional groups on the graphene basal surface, which could be very sensitive to the gas interaction. Research has been carried out on the use of RGO for detection of various gases, such as NO_2 and NH_3 . [113, 119] However, its sensitivity is limited and the recovery time is very long. RGO was also used for hydrogen gas sensing at room temperature; [120] however, the

sensitivity is very low. Pd functionalized multi-layer graphene nanoribbon has been synthesized and used as H₂ gas sensors.[121] This hybrid structure greatly enhanced the sensing performance compared with pure graphene. In addition, graphene-based gas sensors have been reported for detection of H₂S and ethanol.[122, 123] Nevertheless, there is still plenty of room for developing new structures based on graphene or RGO toward gas detection.

1.2.5 Literature review on hybrid nanostructures for gas sensors

As mentioned above, CNT and graphene are attractive for various applications due to their excellent chemical and mechanical properties. They have also been used as potential building blocks of hybrid structures for various applications including gas sensing. Although bare CNTs have sensing responses to gaseous NO₂ and NH₃, [124-128] which are two typical pollutants necessary to be monitored in our living environment and in industries, the sensing sensitivity and selectivity are limited.

To improve the sensor performance, much effort has recently been devoted to developing CNT-based hybrid structures for gas sensors. Among the CNT-based hybrid sensors, CNTs coated with NPs present a new binary system which shows enhanced sensitivity and selectivity to various gases, such as CO,[129] H₂S,[130] H₂,[131] CH₄,[132] ethanol,[133] NO₂,[134] and NH₃. [135] Besides some structural modification by organic materials,[136] CNTs coated with metal or metal oxide NPs are the vast majority of binary systems reported so far because of the beneficial interaction between

NPs and the CNTs.[56, 129, 130, 132, 133, 134-136] The decorated NPs have high surface-to-volume ratio and act as the attractive agent for particular gases, while the underlying CNTs serve mainly as the conducting channels. Based on studies of binary CNT-based sensors, carefully introducing another one or more phases is expected to further improve the sensing performance due to the functional combination of each component and the potential interaction between them. However, till now, few studies were carried out on CNT-based sensor systems with ternary or even more phases. Recently, Ning Du's group used a layer-by-layer assembly method to coat pristine MWCNTs, forming SnO₂/Au/CNTs ternary composites.[24] The as-prepared ternary system showed higher sensing performance to CO at room temperature than Au/SnO₂ and SnO₂/CNTs.

Generally, a noble metal (e.g., Au, Ag) is introduced into a semiconducting CNT system because of its catalytic activity. Some of these metals have beneficial selective interactions with certain gases. For instance, Au is highly active for low temperature CO oxidization.[137] Two possible sensing mechanisms were proposed for noble metal additives, "chemical sensitization" and "electronic sensitization." [138, 139] "Chemical sensitization" proposes that noble NPs activate and dissociate the test gas, and the atomic products diffuse to the surface of sensing semiconductor support (e.g., SnO₂) by the spill-over effect. Then the atomic products react with the negatively charged oxygen adsorbates, accompanying a concentration change of adsorbed oxygen and hence charge transfer. The alternative mechanism, "electronic sensitization," proposes that a charge-depletion layer forms around the promoter (i.e., noble metal) through oxygen

adsorption, and the oxidation state change of the promoter directly affects the electronic state of the semiconductor support, leading to a change in electrical resistance.

Graphene decorated with NPs is a novel class of materials, and it gradually draws the interest of researchers. Although graphene consists of carbon atoms which are the same as in CNTs, its 2D structure is quite different from that of CNTs. Graphene has even higher specific surface area than CNTs. However, FET based on graphene has low on-off current ratio due to its zero bandgap in vacuum. Interestingly, defects on graphene surface can greatly affect the electronic properties of graphene. Therefore, it is possible to tailor graphene's electronic property by introducing nanocrystals on the surface and use the resulting hybrid structures for gas sensing. Studies showed that hybrid structures consisting of Pt and RGO have high sensitivity to hydrogen.[140] In a few other studies, NPs were also deposited on graphene for gas sensing applications. For example, gold NPs decorated RGO was used to detect H₂S and NO₂:[141] SnO₂ NPs were uniformly coated on graphene, which showed selectivity to propanal.[142] Till now, most of the methods used for assembling NPs onto graphene surface are wet-chemical methods. And the research into hybrid structures based on graphene is just at the beginning. There is much room for developing graphene-based hybrid nanostructures for gas sensing applications.

1.2.6 Summary and conclusions

In summary, CNTs, graphene, graphene-based materials and nanoparticles are promising materials in various applications due to their unique structures and properties. In

particular, they exhibit significant potential in gas sensing applications. However, the sensing performance is limited when these materials are used individually. Hybrid structures combining nanoparticles with nanocarbon materials (e.g., CNTs or graphene) can dramatically improve the gas sensing performance, due to not only the unique properties of nanoparticles and nanocarbon materials but also the interaction between them. Exploration on the use of the novel hybrid structures of nanoparticle-decorated nanocarbon materials for tuning the gas sensing performance is still in its infant stage. There is significant room in the synthesis of hybrids in a cost-effective and well-controlled fashion for highly sensitive, selective, and stable gas sensors.

1.2.7 Research objective and dissertation outline

The main research objective of this dissertation is to demonstrate the tunability of sensing performance of gas sensors based on various nanocarbons (e.g., CNTs and RGO) through decorating their surfaces with desirable nanoparticles. Specific tasks of the study include fabrication and testing of highly selective and sensitive gas sensors based on NP-decorated nanocarbon materials using two methods. One method is to synthesize NPs using a mini-arc plasma source, followed by *in situ* assembly of the resulting NPs onto the surfaces of CNTs or graphene. The mini-arc plasma method features a low cost, minimal contamination, and flexibility in obtaining desired NPs through tailoring reactor parameters. Based on this technique, various NPs have been synthesized and characterized in Chapter 2, for instance, pure SnO₂, Ag, and binary WO₃-SnO₂ NPs. The

resulting NPs were *in situ* assembled onto the surfaces of CNTs or graphene, forming two different sensing platforms. Chapter 3 presents hybrids of Ag NPs-decorated MWCNTs and SWCNTs for selective NH₃ sensing. Chapter 4 describes a new ternary system combining Ag NPs with SnO₂ NPs on MWCNTs to demonstrate that Ag NPs can further enhance the sensing performance of MWCNTs/SnO₂ sensors. Inspired from the above studies, Ag NPs were decorated on RGO as a novel sensing platform for NH₃ detection, which is discussed in Chapter 5. Although the mini-arc plasma method has many advantages in fabricating NPs, it is limited in producing NPs in terms of material types. For example, Ru NPs are difficult to be produced with mini-arc plasma because of very high melting temperature of Ru (2,334 °C). To synthesize NPs that are difficult to produce using the mini-arc plasma method, a wet-chemical method was used with its high capability in the control of NP size and morphology. Based on this method, novel hybrids of In- and Ru-doped SnO₂ NPs on RGO were produced for selective NO₂ sensing in Chapter 6, together with discussions on possible sensing mechanisms. A summary of the dissertation study and recommendations for future studies are presented in Chapter 7.

CHAPTER 2 SYNTHESIS OF PURE AND BINARY NANOPARTICLES

2.1 Experimental methods

Figure 2.1 shows a schematic of the experimental setup, which is similar to that described in our previous reports.[116, 143] In brief, aerosol nanoparticles were produced using an atmospheric mini-arc plasma source. The bottom anode made of graphite is machined to form a groove to hold the precursor material. Depending on desired products, the top cathode could be tungsten or graphite. Tungsten oxide NPs were prepared using a graphite cathode with no precursor material on the bottom anode. For Ag NPs synthesis, bulk Ag was used as the source material. Ag nanocrystals are easy to form with fast cooling which has been studied before.[143] For pure tin oxide NPs, a graphite cathode was used with pure tin (99.998% purity, ESPI material) or SnO (99.9% purity, Alfa Aesar) as the precursor. For tin oxide and tungsten oxide composite NPs, a tungsten cathode and pure tin precursor were used. The tungsten cathode was polished to remove the native surface oxide prior to experiments. The arc was driven by a commercial tungsten inert gas (TIG) arc welder (Miller Maxstar 150 STH). An electrostatic field was used to facilitate the collection of charged particles on substrates.[143] Since the final product will be used for sensor applications, the particles should be crystalline. Therefore, amorphous NPs produced from SnO were crystallized through annealing in a tube furnace. The samples with amorphous NPs were introduced into a tube furnace (Lindberg/Blue M TF55035A-1) through quartz tubing. All the samples were annealed at 400 °C. To investigate the effect

of oxygen on the crystallization process, two different atmospheres were used, Ar and O₂.

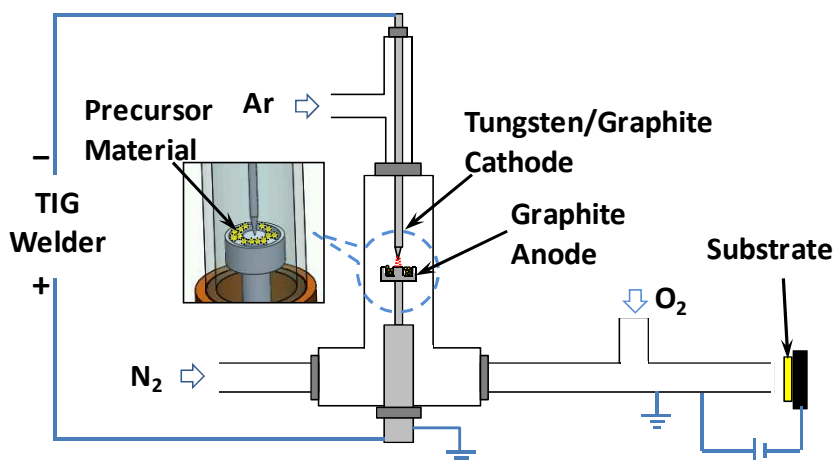


Figure 2.1 Schematic of a mini-arc plasma reactor for nanomaterial synthesis and the setup for subsequent assembly of as-produced nanomaterials.

To directly synthesize SnO₂ crystalline NPs, a modified mini-arc plasma method was used as shown in Figure 2.2. SnO powder (99.9% purity, Alfa Aesar) was used as the source material for SnO₂ synthesis. SnO was evaporated by the mini-arc plasma generated between two graphite electrodes, and carried downstream by pure Ar gas. Pure O₂ was introduced afterwards and mixed with SnO vapor. The mixture went through a tube furnace with a high temperature (800–1,000 °C). Crystalline NPs were formed and collected onto substrate using an electrostatic field which helps the particle collection,[143] because a fraction of NPs were electrically charged by the mini-arc plasma or thermionic emission of electrons from the NPs surfaces.

The morphology and structure of as-produced NPs were characterized by a conventional (phase contrast) Hitachi transmission electron microscope (TEM) (H-9000-NAR) operated at an accelerating voltage of 300 kV. High-resolution TEM

(HRTEM) and selected area electron diffraction (SAED) were carried out to verify the nanostructure of the particles. Scanning electron microscope (SEM) was used to characterize the morphology of the nanomaterials.

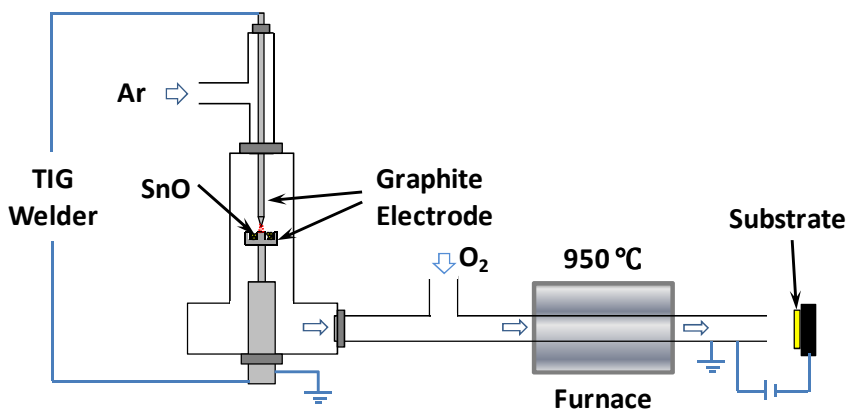


Figure 2.2 Schematic experimental setup for SnO₂ NP synthesis.

2.2 Results and discussion

2.2.1 Effect of oxygen-to-argon flow ratio ($Q_{\text{oxygen}}/Q_{\text{argon}}$)

Although the reactor pressure was maintained at the atmospheric pressure, our experiments indicate that oxygen can back flow to the mini-arc region in the reactor from the inlet of the oxygen gas due to convection and diffusion. This is confirmed by monitoring a tungsten cathode in the reactor under different synthesis conditions. The tungsten cathode surface was polished before arc generation as shown in Figure 2.3. Table 2.1 lists the conditions of a series of experiments designed for inspecting the influence of oxygen on the reactor. No precursor was used in this series of experiments. Only tungsten cathode and graphite anode were present in the reactor. All parameters were fixed except

for the gas flow rates. The results show that the higher the ratio of $Q_{\text{oxygen}}/Q_{\text{argon}}$ used, the more seriously the tungsten cathode was oxidized as indicated by the color change of the tungsten cathode surface. As shown in Figure 2.3, with the highest $Q_{\text{oxygen}}/Q_{\text{argon}}$ ratio of 2.5, the W surface is completely black except the little tip area. Because the temperature around the tip was very high, tungsten oxide on that region of the electrode was evaporated to the gas phase since tungsten oxide vaporizes significantly when temperature is higher than 750 °C.[30] As the ratio of $Q_{\text{oxygen}}/Q_{\text{argon}}$ decreased, the surface of the W cathode became lighter, indicative of less oxidation. With no oxygen introduced into the system, the W surface has the lowest oxidization degree, but the surface was still oxidized when compared with the initial polished tungsten likely due to the leakage of oxygen into the reactor from the surrounding of the system as the reactor was not sealed very well. So it is anticipated that oxygen concentration is different in the reactor chamber with different ratios of $Q_{\text{oxygen}}/Q_{\text{argon}}$, which affects the formation and morphology of nanomaterial products.

Table 2.1 Reactor parameters for preparation of tungsten oxide samples. Same gas flow parameters were used for synthesis of mixed metal oxide samples with addition of Sn precursor, and for tin oxide samples with Sn or SnO precursors and with C-C electrodes.

Sample	Electrodes	Precursor	Ar flow rate(L/min)	O ₂ flow rate(L/min)	Flow ratio of O ₂ /Ar	Current (A)	Reaction time (min)
A	W-C	NONE	2	5	2.5	38	5
B	W-C	NONE	2	3	1.5	38	5
C	W-C	NONE	3	3	1	38	5
D	W-C	NONE	2	0	0	38	5

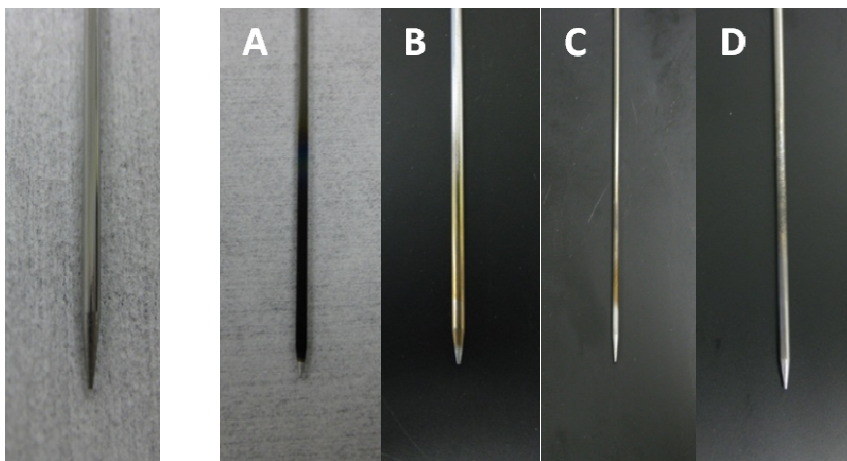


Figure 2.3 Photographs of tungsten electrodes (1/16 inch in diameter). The leftmost electrode is a polished tungsten electrode before experiment. The right four images are tungsten electrodes after experiments corresponding to samples A, B, C, and D in Table 2.1, respectively, as marked in the images.

2.2.2 Tungsten oxide nanoparticles and nanorods (NPs and NRs)

It is possible to fabricate tungsten oxide nanostructures even without any precursor material when using a tungsten cathode because of the nature of the electrode materials. In the present experiments, the tungsten cathode itself served as the source material. The tungsten cathode surface was oxidized by the oxygen in the reactor, and then evaporated by high temperature generated by the arc. Upon cooling at the low temperature region, the vapor forms tungsten oxide nanocrystals. Figure 2.4a is a representative SEM image showing an overview of as-produced NPs. Since the nanocrystals are very small, multiple bright-field TEM images with a higher magnification were taken from each sample (such as Figure 2.4b). The tungsten oxide materials that were produced have different morphologies depending on the synthesis parameters. With Q_{argon} of 2 lpm, Q_{oxygen} of 5 lpm ($Q_{\text{oxygen}}/Q_{\text{argon}}=2.5$) and a current of 38 A, two different morphologies of tungsten oxide, NPs as well as NRs, were observed simultaneously in sample A, as shown by the

TEM image in Figure 2.4b. The statistical results on NPs and NRs are derived by counting NPs and NRs that are clearly visible and separate in several TEM images. We do not count within the agglomerated clusters to avoid subjective judgments and projection errors. Both SEM and TEM images show that these agglomerates contain both rods and clusters, allowing us to assume that measurements obtained from the dispersed particles are representative for the overall samples. For sample A, the percentage of NPs is approximately 82% with about 18% NRs. The size of most NPs was between several nanometers and 50 nm. Very few larger NPs about 100 nm were also found in the sample. The inset of Figure 2.4b shows the SAED pattern of the product mixture of NPs and NRs. The continuous polycrystalline rings of the SAED pattern clearly indicate that the particles are crystalline and deposited in random orientations on the lacey carbon support film. An HRTEM image of one NP is shown in Figure 2.4c, illustrating that most of its nanovolume consists of an ordered single crystal lattice, with a partially disordered region at one end of the particle (bottom right in the image). The measured lattice spacings of 0.381 nm and 0.377 nm in the ordered region are in agreement with (002) and (020) planes of monoclinic WO_3 , respectively. The defective region is dominated by oxygen vacancies in random sites, leading to separation and rotation of the sub-blocks of WO_3 . In contrast to the NPs, the NRs appear well ordered throughout their volume, as shown in the HRTEM image in Figure 2.4d. Tungsten oxide observed in this unique NR morphology has previously been identified as non-stoichiometric monoclinic $\text{W}_{18}\text{O}_{49}$.^[116] The lattice spacing of the growth plane in the $\text{W}_{18}\text{O}_{49}$ NR is 0.378 nm, corresponding to the (010) plane. This result is consistent with the finding that $\text{W}_{18}\text{O}_{49}$ is most likely to

grow along $\langle 010 \rangle$ direction because of the relatively higher surface energy of the (010) plane.[116]

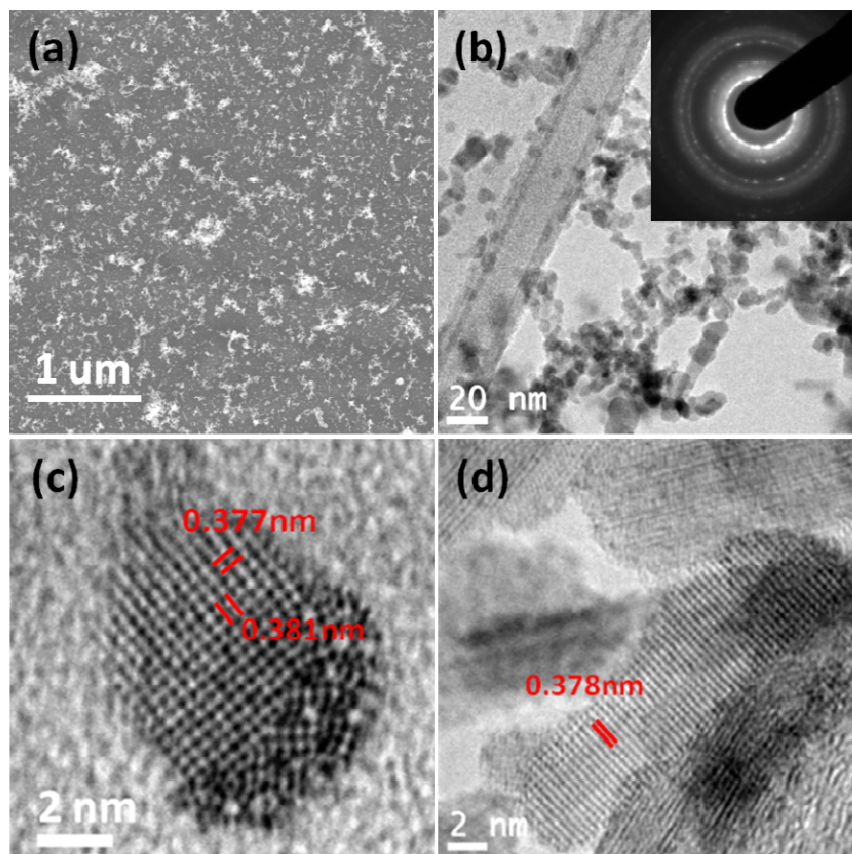


Figure 2.4 SEM image, TEM images, and SAED pattern of tungsten oxide produced with $Q_{\text{oxygen}}/Q_{\text{argon}}=2.5$ (sample A in Table 2.1). (a) SEM image and (b) Bright field (BF) low magnification TEM image of as-produced tungsten oxide. The long straight edge in image (b) is the lacey carbon film support. The inset in (b) is an SAED pattern of as-produced NPs. (c) and (d) HRTEM images of tungsten oxide NP and NRs.

When Q_{argon} was maintained at 2 lpm, but Q_{oxygen} was reduced to 3 lpm ($Q_{\text{oxygen}}/Q_{\text{argon}}=1.5$), larger quantities of NRs (about 61% of as-produced nanomaterials) were produced as shown in the BFTEM micrograph of sample B in Figure 2.5a. Based on an HRTEM image of the NRs (Figure 2.5b), the measured lattice spacings are still consistent with $W_{18}O_{49}$. When the parameters of sample C ($Q_{\text{oxygen}}=3$ lpm and $Q_{\text{argon}}=3$ lpm ($Q_{\text{oxygen}}/Q_{\text{argon}}=1$)) were used in the NP synthesis, tiny crystalline tungsten oxide

proto-NRs was fabricated. HRTEM image of the NRs is shown in Figure 2.5c. The NRs are 2–3 nm in diameter and about 5 nm in length. When Q_{oxygen} was further reduced to zero and Q_{argon} of 2 lpm ($Q_{\text{oxygen}}/Q_{\text{argon}}=0$) was kept in the system, almost all the tungsten oxide product in sample D was of NR morphology. From the low magnification TEM image in Figure 2.5d and HRTEM image in Figure 2.5f, it can be seen that the NRs, quite uniformly distributed on the substrate, have a short axis of 2–10 nm and a long axis between several nanometer to tens of nanometer. The SAED pattern in Figure 2.5e exhibits only two strong diffraction rings, which are identified as the (010) plane and (020) plane of monoclinic $W_{18}O_{49}$. Similar SAED patterns were observed in other regions of the sample. The lack of reflections corresponding to WO_3 suggests that all of the nanostructures formed with $Q_{\text{oxygen}}=0$ are oxygen-deficient $W_{18}O_{49}$ NRs.

Clearly, decreasing the ratio of $Q_{\text{oxygen}}/Q_{\text{argon}}$ leads to not only the change in the stoichiometry of produced nanomaterials from WO_3 to $W_{18}O_{49}$, but also the transition of product morphology from NPs to NRs. Since only Q_{oxygen} was changed and all other synthesis parameters were maintained constant, it is reasonable to conclude that oxygen quantity affects the composition and shape of the product nanomaterials from the arc reactor. In these experiments, the tungsten cathode itself served as the source material. Tungsten oxide was first formed on the surface of tungsten cathode, and then was evaporated to the gas phase. According to previous studies, WO_3 can sublime easily at low temperatures[30] and decompose under high temperature forming non-stoichiometric WO_{3-x} . [144] Crystallization of tungsten oxide occurred when the vapor was quenched. Higher $Q_{\text{oxygen}}/Q_{\text{argon}}$ ratio results in more oxygen in the reactor chamber, boosting the

nucleation of WO_3 rather than non-stoichiometric WO_{3-x} and leading to WO_3 spheres in the gas phase, consistent with other studies.[145, 146] However, in a low oxygen environment, oxygen loss would happen to WO_3 , and growth of a particular non-stoichiometric tungsten oxide, $\text{W}_{18}\text{O}_{49}$, is favorable. This $x=0.272$ sub-oxide phase of WO_{3-x} has ordered oxygen vacancies, leading to different unit cell dimensions and observed lattice periodicities. $\text{W}_{18}\text{O}_{49}$ prefers growing into one-directional NR in the gas phase because of the anisotropic property of the building blocks.[147]

The mechanism of NP formation in the gas phase includes nucleation, particle growth, particle coagulation, and particle coalescence.[145] It is obvious that there was no heterogeneous nucleation site around the source material. Therefore tungsten oxide NP formation was a homogeneous nucleation and growth process, which is consistent with the earlier study.[146] In our experiments, tungsten oxide vapor was quenched very rapidly, leading to a supersaturated atmosphere for homogeneous nucleation. Then the particles grew to a larger size through coagulation. When the concentration of the condensed material is low, the molecule or NP collision frequency is low, leading to very fine NPs. A high quenching rate also can boost fine NPs because of short growth time, which can be evidenced in Figure 2.4c. Both ordered and disordered region exist in the same small NP, which also implies a short growth time. Since Ar flow was used in the system to dilute and quench vapor, both of the above mechanisms are responsible for the fine NP formation. A few large particles also formed in the sample, which is ascribe to the coalescence growth. Considering the growth mechanism for tungsten oxide NRs, it appears to be vapor-solid (VS) growth. Vapor-liquid-solid (VLS) growth mechanism has

been used to explain the NR formation, which is evidenced by a droplet at the tip of NRs.[148] However, the morphology of NRs shown in Figure 2.4d and Figure 2.5 suggests that there is no droplet or catalyst at the NR tip.

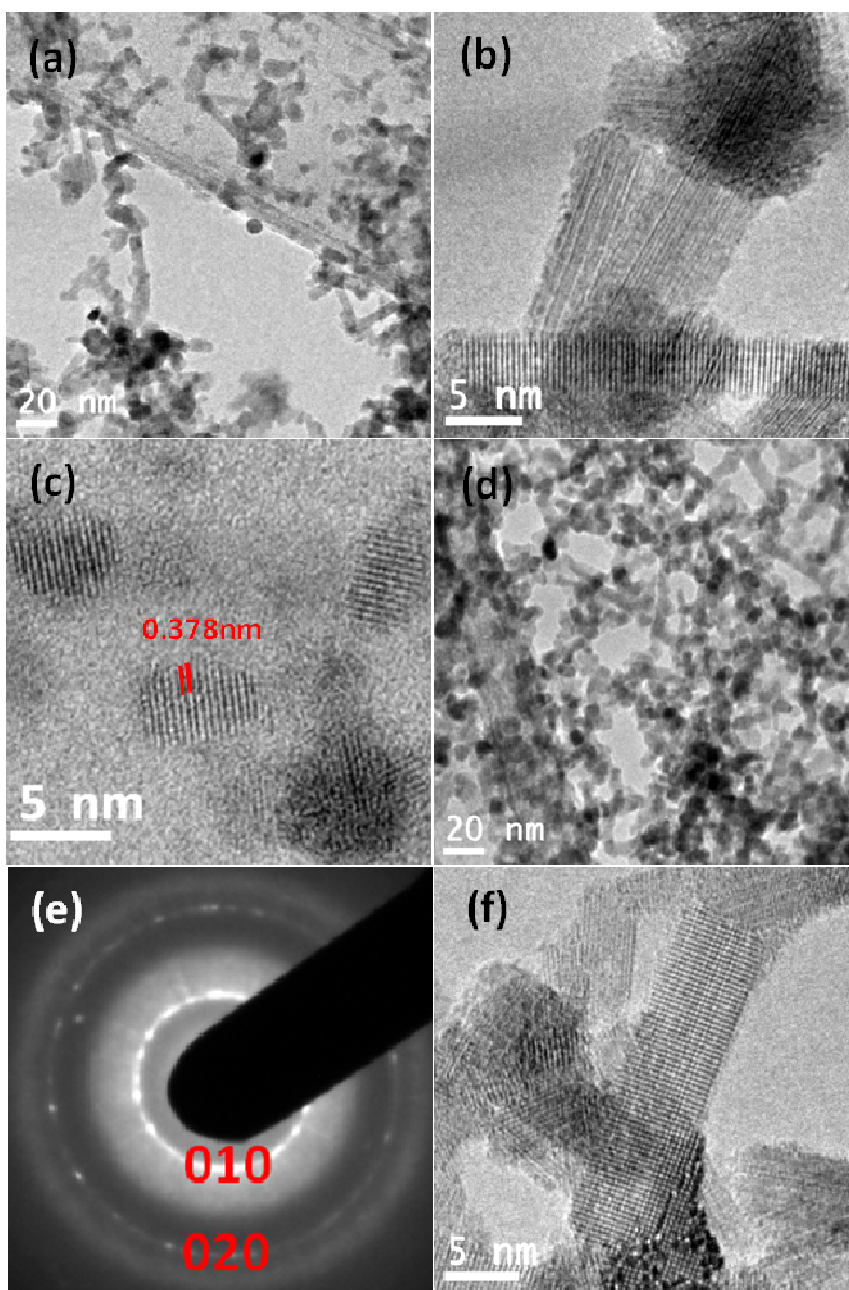


Figure 2.5 BF low magnification TEM (a) and HRTEM (b) images of nanomaterials produced with $Q_{\text{oxygen}}/Q_{\text{argon}}=1.5$ (sample B in Table 2.1). (c) HRTEM image of tungsten oxide proto-NRs produced with parameters used for preparing sample C in Table 2.1. (d) BF low magnification

TEM image, (e) SAED pattern and (f) HRTEM image of NRs produced with $Q_{\text{oxygen}}/Q_{\text{argon}}=0$ (sample D in Table 2.1). The lattice spacings in the HRTEM image and the diffraction rings in the SAED pattern are consistent with $W_{18}O_{49}$.

2.2.3 Tungsten oxide and tin oxide NP mixture

The mini-arc synthesis system is capable of producing tungsten oxide and tin oxide NP mixtures with pure tin as the precursor and tungsten as the cathode. Figure 2.6a shows a BFTEM image of NP mixtures of tungsten oxide and tin oxide synthesized with Q_{argon} of 2 lpm and Q_{oxygen} of 5 lpm ($Q_{\text{oxygen}}/Q_{\text{argon}}=2.5$). As shown in the image, the particles are mostly round with particle sizes between several nanometers and about 30 nm. A few large particles with diameters greater than 100 nm were found. Compared with Figure 2.4b (prepared without Sn), the SAED pattern in Figure 2.6b has diffraction rings (highlighted in green arcs) corresponding to SnO_2 (110) and (101), in addition to rings (red arcs) from tungsten oxide. Figure 2.6c shows an HRTEM image of a WO_{3-x} NP which is spherical and has lattice spacings of 0.384 nm and 0.366 nm corresponding to (022) and (200) planes of monoclinic WO_3 , respectively. Figure 2.6d shows the HRTEM image of an NP mixture consisting of a bigger WO_{3-x} NP (~10 nm) coated with smaller SnO_2 NPs (about 2 nm in diameter). The EDS spectrum (Figure 2.6e) indicates that there are only W, Sn, and O in the product, confirming a mixture of tin oxide and tungsten oxide NPs. Since WO_3 and Sn were evaporated into the gas phase at the same time, a mixture vapor formed. After reaction in the oxygen atmosphere at a high temperature followed by crystallization, SnO_2 and WO_{3-x} NPs form a NP mixture in the gas phase. Therefore, usually the two types of NPs mixed together when collected onto a substrate.

These uniformly mixed NPs can be used to produce gas sensors with enhanced sensing performance.[149]

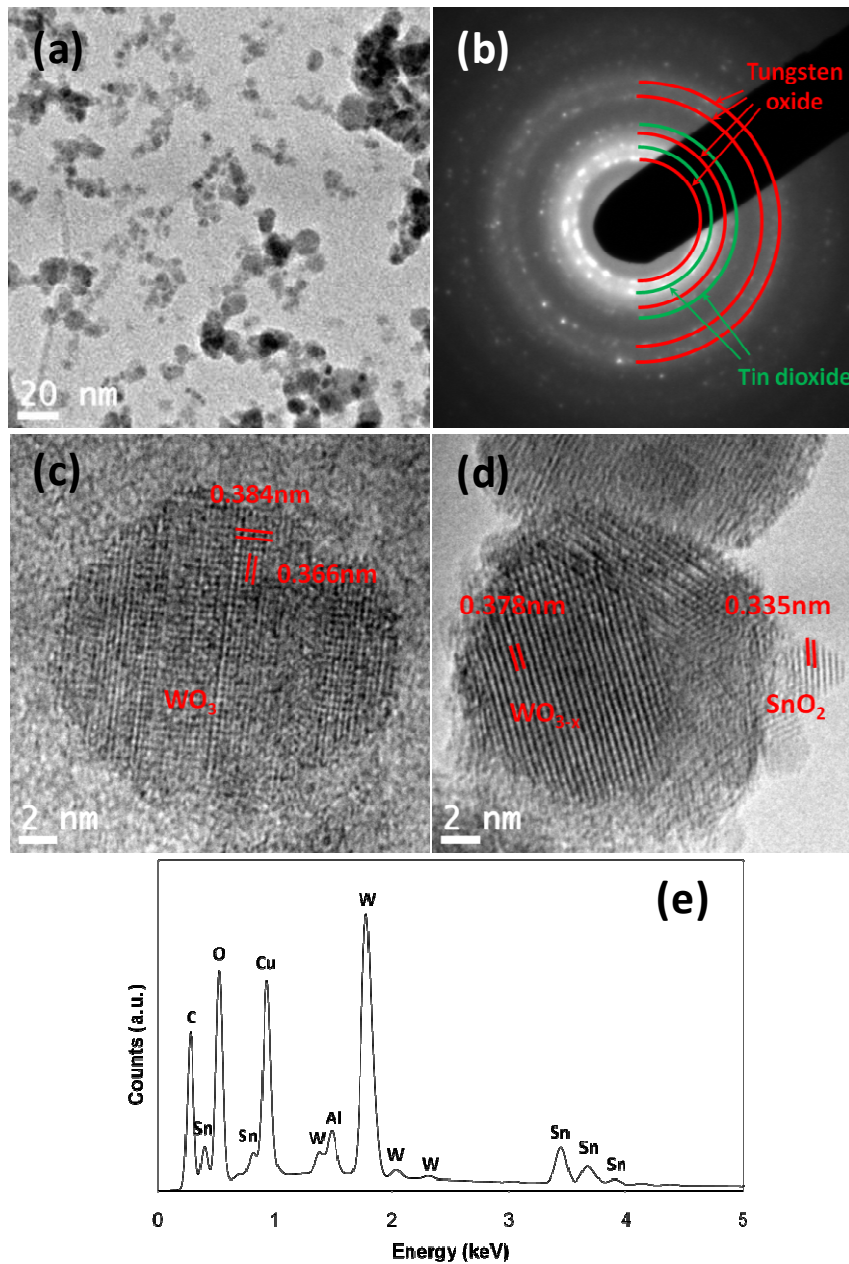


Figure 2.6 BF low magnification TEM image (a), SAED pattern (b), and HRTEM images (c, d) of tungsten oxide and tin oxide NP mixture. The parameters used here are equivalent to those for sample A in Table 2.1 ($Q_{\text{oxygen}}=5$ lpm, $Q_{\text{argon}}=2$ lpm ($Q_{\text{oxygen}}/Q_{\text{argon}}=2.5$)), current of 38 A and 5 min collection time. (e) is the EDS spectrum of NPs shown in image (a), where C and Cu are from TEM grid, and Al is from the TEM grid holder.

When Q_{argon} was increased to 5 lpm and other parameters remained the same ($Q_{\text{oxygen}}/Q_{\text{argon}}=1$), the as-produced NPs are in random shape and the interface is blurry (Figure 2.7a). The resulting SAED pattern (inset of Figure 2.7a) indicated that most of the particles were amorphous, with just a few crystalline particles, as seen from the broad diffuse rings and few sharp spots. Combined with HRTEM characterization (Figure 2.7b), these crystalline particles were determined to be tungsten oxide (WO_{3-x}). Thus it can be concluded that a high flow rate of argon will actually hinder the crystallization of NPs in the gas phase, with stronger impact on tin oxide than on tungsten oxide.

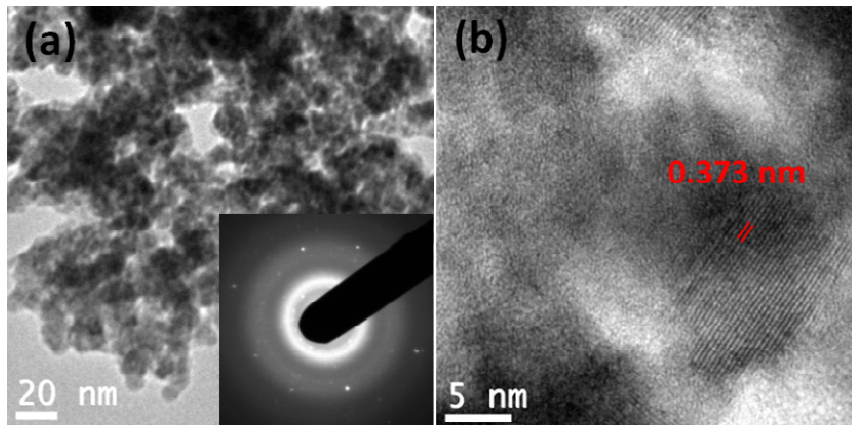


Figure 2.7 BF low magnification TEM image (a), and HRTEM image (b) of NPs synthesized with $Q_{\text{oxygen}}=5$ lpm and $Q_{\text{argon}}=5$ lpm ($Q_{\text{oxygen}}/Q_{\text{argon}}=1$). The upper electrode is tungsten and the precursor is tin. The inset in (a) is the SAED pattern.

Several factors should be considered for the formation of amorphous NPs. One important factor is the vapor quenching rate. Quenching will saturate the aerosol vapor, thereby initiating the crystal nucleation. Further crystal growth and aggregation will form larger particles and particle clusters.[143, 150] However, if the cooling rate is too fast, the vapor would have insufficient time to crystallize and form long-range order structures;

instead, it is frozen with the disordered status. In our experiment, Ar gas carried the aerosol flow from the arc region toward downstream. Consequently, the temperature decreased quickly because of the heat transfer through the tubing. Increasing Ar flow rate results in a shorter residence time and increasing cooling rate of aerosol vapor in the reactor chamber. This means that the quenching rate will be too high to form aerosol crystals, resulting in the amorphous structure of product NPs.

Oxygen partial pressure could be another factor affecting the formation of amorphous NPs. Until now, there have been no reports about how oxygen partial pressure can affect the formation or nucleation of oxide crystals, for the materials synthesized here. Our experiments suggest that oxygen indeed plays an important role in the nucleation of oxide in the gas phase. In the previous section it was shown that crystalline tungsten oxide proto-NRs were synthesized with parameters of sample C (Table 2.1 and Figure 2.5c) in the absence of a precursor. However, after adding pure tin in the system as the precursor, keeping other parameters the same as sample C, completely amorphous materials were synthesized and tungsten oxide proto-NRs were not observed. In this case, oxygen concentration was the same before and after adding the tin precursor in the reactor chamber. But when tin was added, it competes for oxygen with tungsten, and tungsten oxide got less oxygen than that in the case without tin, leading to amorphous particles. Therefore, oxygen concentration is another important aspect in the formation of amorphous phase, which is in agreement with previous literature.[151]

Finally, particle size may also contribute to the amorphous phase. According to the oxidation study of nano-sized tin NPs, oxidation induced amorphization occurred in

nanophase tin because of the ultrafine size of the particles. It was reported that nucleation of the crystalline oxide on the surface of nanophase tin particles seems to be strongly suppressed since long-range ordering of atoms is hindered by the lattice distortion accompanying crystallographic imperfections.[152] In our experiment, tin precursor was evaporated into vapor, and was oxidized in an even ultrafine phase. Consequently, due to the ultrafine size, the resulting material has a high chance of forming amorphous phase.

2.2.4 Tin dioxide NPs

To produce pure tin dioxide, a graphite cathode was used instead of tungsten. Figure 2.8a shows the BFTEM image of as-produced SnO_2 NPs using pure tin as the precursor. The particle size is less than 20 nm while some particles form clusters on the edge of the carbon film. An SAED pattern of such a particle cluster is shown in Figure 2.8b. All rings are consistent with tetragonal structure SnO_2 , which agrees with previous reports.[153, 154]

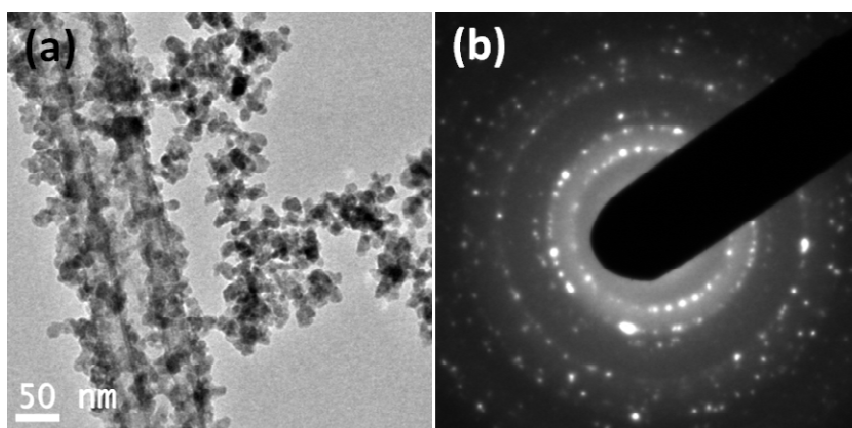


Figure 2.8 (a) low magnification TEM image of tin oxide NPs prepared from pure tin with $Q_{\text{oxygen}}=3$ lpm and $Q_{\text{argon}}=2$ lpm. The current was 25A. (b) SAED pattern of the tin oxide NP clusters shown in (a).

Interestingly, the particles on the interior of the carbon film are amorphous, while the crystalline particles form clusters attached around the edge of the carbon film. The reason of this phenomenon is not clear at present. Further investigation is warranted to understand such a phenomenon. Low degree crystalline SnO₂ particles have been fabricated in gas phase condensation processes by other group.[155] Possible reasons for amorphous NP formation were discussed already. We believe that the clusters were formed in the gas phase, not as single particle collection on the substrate. To prove this, we have performed experiments with significantly reduced NP concentration and a small number of individual crystalline tin oxide particle clusters was still observed. If these particles were individual particles before collection (as-synthesized), they would have distributed uniformly as single particles. This particle aggregation in the gas phase has also been observed by other groups.[156]

Several groups have reported on the use of SnO as a precursor to produce SnO₂, because SnO can easily evaporate at relatively low temperatures.[157-159] We also used SnO as the precursor to synthesize SnO₂ NPs with the mini-arc plasma. Compared with NPs synthesized using pure Sn as the precursor, many more particles were obtained on the substrate for the same assembly time as shown in Figure 2.9a. Some NP clusters form because of the high concentration of particles in the gas phase. Figure 2.9b shows a magnified view of the image in Figure 2.9a on the edge of the substrate, and indicates that the particle size is uniform and less than 10 nm. Figures 2.9c and d show SAED patterns of the particle clusters sitting at the TEM grid carbon film edge and right on top of the

carbon film, respectively. Interestingly, NP clusters are semi-crystalline, but the NPs on the top of the carbon film are totally amorphous in agreement with the result obtained using tin as the precursor.

Since amorphous SnO_2 is insulating, it is not suitable for sensing applications. Upon annealing in a tube furnace for 1 h at 400 °C in either Ar or O_2 atmospheres, the crystallinity of the particles was enhanced and the oxygen effect on particle crystallization was confirmed. Annealing in Ar caused the clustered NPs at the edge of the lacey carbon film to become more crystalline (Figure 2.9e), and some of the particles on the film became crystalline (Figure 2.9f). The rings and spots in the SAED patterns are all indexed to rutile SnO_2 . Further annealing treatment with O_2 for another 1 h led to a well crystalline structure as shown in Figure 2.9g and h. To investigate the effect of annealing gaseous environment, another comparison experiment was carried out using the similar parameters (2 h at 400 °C) but with argon instead of oxygen. The SAED patterns in Figure 2.9i and j show that most particles became crystalline, but the presence of some amorphous particles was evidenced by blurring of the rings. In addition, the diffraction rings are not as sharp as those in Figure 2.9g and h, suggesting that oxygen could affect crystallization in the annealing process. Therefore, from the results above, the particles as produced contain some crystalline SnO_2 , but are predominantly amorphous SnO_2 . However, through annealing treatments, the amorphous SnO_2 NPs can become crystalline. Annealing in oxygen atmosphere makes the crystallization process faster and transforms amorphous particles into better crystals.

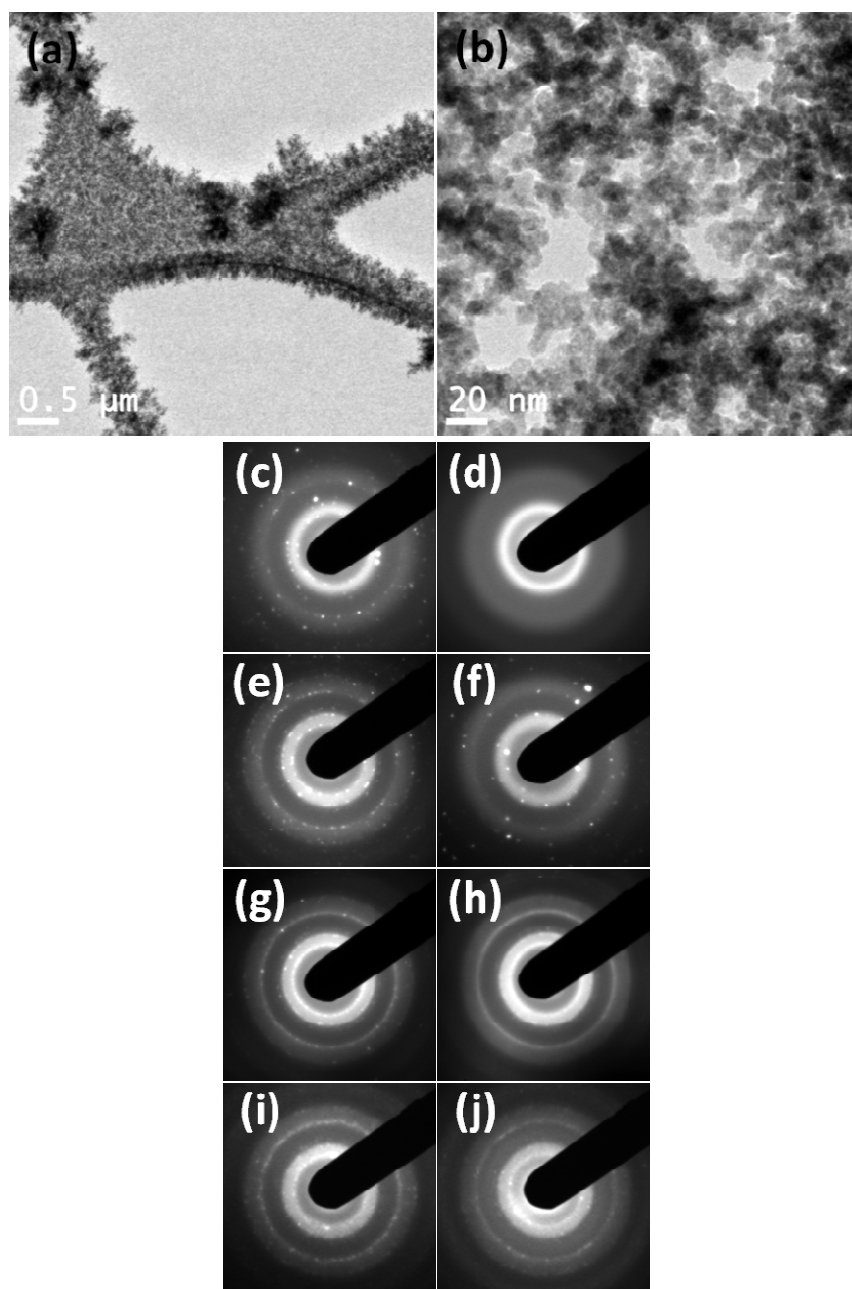


Figure 2.9 (a) and (b) are low magnification TEM images of tin oxide NPs prepared from SnO. The flow rates are $Q_{\text{oxygen}}=3$ lpm and $Q_{\text{argon}}=2$ lpm with a current of 25 A. (c) and (d) are SAED patterns of the particle clusters at the edge and the particles on the carbon film respectively. After annealing in Ar (1 lpm) with 400 °C for 1 h, those SAED patterns turned into (e) and (f). After another annealing in oxygen (1 lpm) with 400 °C for 1 h, they changed to (g) and (h), respectively. (i) and (j) are SAED patterns of another sample prepared with same parameters but annealed in Ar (1 lpm) with 400 °C for 2 h to illustrate the oxygen effect.

To get crystalline SnO₂ NPs directly at the collection, a modified mini-arc plasma setup was used, which includes a furnace in the system (Figure 2.2). The results show that the crystallization of as-produced SnO₂ NPs is significantly affected by tube furnace temperature. For a given variables except furnace temperature, the initial particles are amorphous with room temperature in the furnace. As shown in Figure 2.10a, there is no clear ring in the SAED pattern of the particles, which means no crystal forms. Gas phase condensation method has been used for amorphous SnO₂ synthesis.[25, 160] Several reasons are responsible for amorphous phase formation according to literatures, such as quenching rate, oxygen concentration,[151] and ultrafine particle size.[152] But we believe quenching rate is too fast for SnO₂ vapor to form crystals in our experiments, because with annealing in gas phase by a tube furnace, the NPs became crystalline. When 800 °C was used in the tube furnace, the particles form very tiny crystals, which suggest that the crystals are at the status of nucleation. So the SAED pattern shows thin and weak rings (Figure 2.10b). With further increasing temperature to 900 °C, the SAED pattern of the particles is clear and the rings are much sharper, which means relative bigger crystalline particles formed (Figure 2.10c). 1,000 °C was also used for particles synthesis. From SAED pattern in Figure 2.10d, the particles are even better for crystallization. Both SAED patterns (Figure 2.10c and d) are from rutile-structured SnO₂, which is consistent with other reports.[13, 25, 161] Figure 2.10e and f are bright field TEM and HRTEM images of NPs synthesized with annealing temperature of 900 °C. As shown in the images, the particles distributed uniformly and with some agglomeration. The single crystal size is about 5 nm and the lattice fringe of 0.335 nm is indexed as (110) planes of rutile SnO₂.

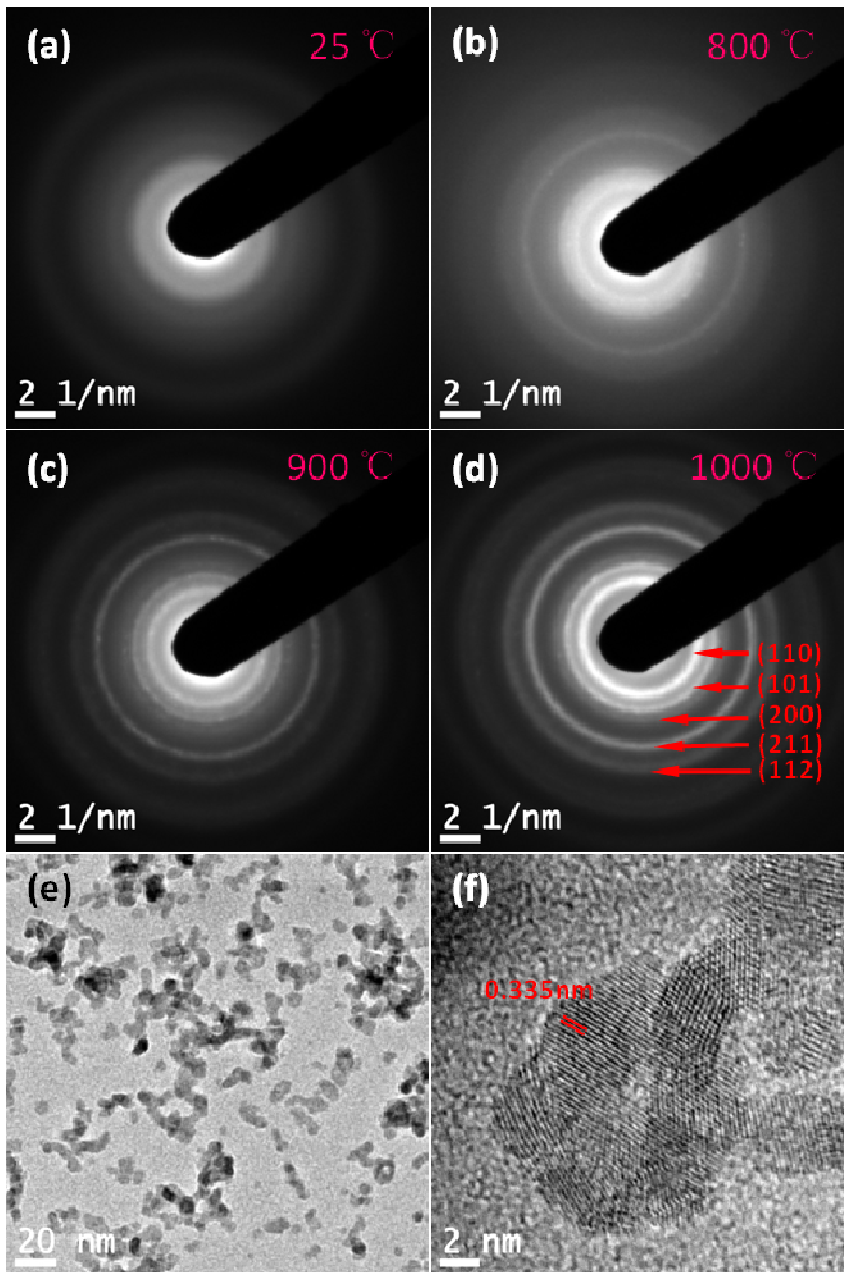


Figure 2.10 (a-d) are SAED patterns evolution of SnO₂ NPs synthesized by modified mini-arc plasma method with different furnace temperature. (e) and (f) are TEM and HRTEM images of SnO₂ NPs synthesized with 900 °C of furnace temperature.

2.2.5 Silver NPs

Noble metal materials NPs, like Ag, also can be produced using a mini-arc plasma source

with both electrodes made of graphite. A low magnification TEM image of as-produced Ag NPs is shown in Figure 2.11a. The NP sizes are in the range of 1–10 nm with good uniformity. The continuous rings in the SAED pattern (Figure 2.11b) show good crystallinity of the NPs and they are indexed to (111), (200), (220) and (311) planes of Ag

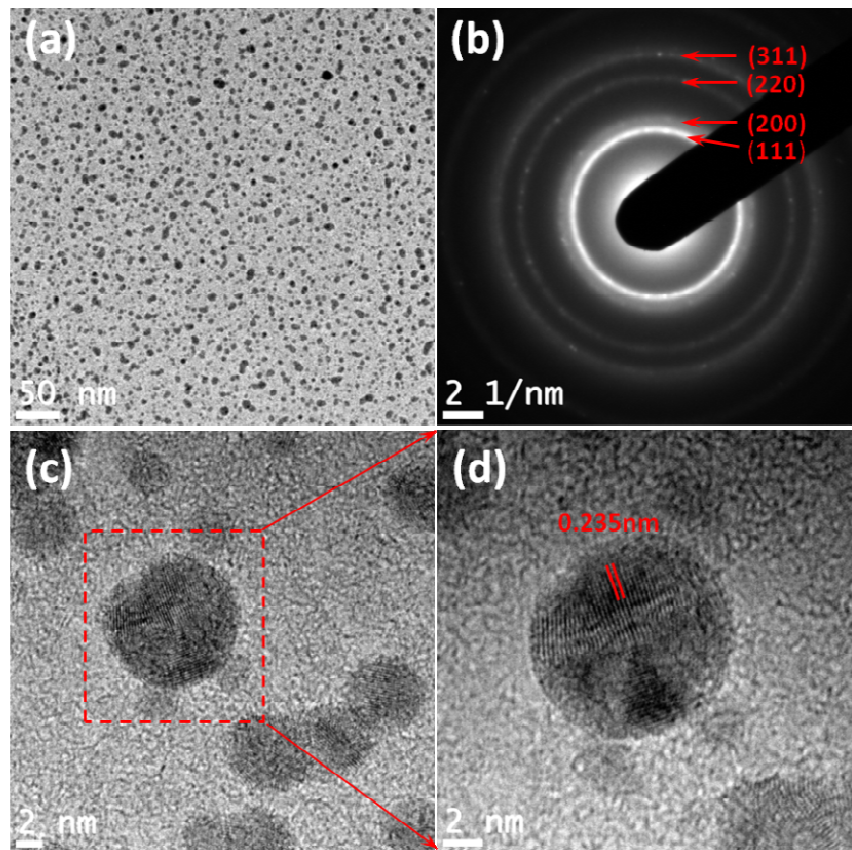


Figure 2.11 Low magnification TEM image (a) and SAED pattern (b) of as-produced Ag NPs. (c), and (d) HRTEM images of Ag NPs. In the synthesis process, the flow rates are $Q_{\text{oxygen}}=0$ lpm and $Q_{\text{argon}}=3$ lpm with a current of 40 A.

nanocrystal from the center ring outwards. Some NPs aggregated together on the carbon film support as shown in Figure 2.11c. There are two possible reasons for this. One is that the particle collision in the gas phase because of random motion. The other reason is the relatively long deposition time. With long time deposition, the new coming NPs may

deposit on top or next to previous ones, forming NP chains. All individual particles have a spherical shape because of homogeneous growth in the gas phase. The lattice spacing of 0.235 nm from (111) plane of crystalline Ag can be seen clearly in the HRTEM image of Figure 2.11d.

2.3 Summary and conclusions

Several types of nanomaterials, including silver NPs, tungsten oxide NPs, tungsten oxide NRs, tin oxide NPs, and mixture of tungsten oxide and tin oxide NPs, have been synthesized using a mini-arc plasma source. These nanomaterial products can potentially be used for gas sensing applications. Oxygen was found to be present in the mini-arc plasma reactor through convection and diffusion when oxygen was used as an oxidant to synthesize oxide particles. And the amount of oxygen in the reactor significantly affected composition and morphology of product nanomaterials. Lean oxygen environment produced more $W_{18}O_{49}$ NRs using tungsten cathode as the source material while amorphous particles were synthesized with a high argon flow rate and the presence of a precursor material. Possible reasons for the amorphous particle formation include high quenching rate, low oxygen partial pressure, and ultrafine particle size. Annealing in oxygen atmosphere can more efficiently transform amorphous tin oxide NPs into crystalline ones than in argon atmosphere. This study provides a thorough understanding of the nanomaterial synthesis process using a mini-arc plasma source and also sheds light on gas-phase nanomaterial synthesis in general. It is anticipated that results from this study can be used to tailor reactor parameters for desired nanomaterial products.

CHAPTER 3 SILVER NANOCRYSTALS-DECORATED CNTs FOR AMMONIA SENSING

3.1 Experimental methods

3.1.1 Material synthesis and characterization

To synthesize hybrid structures of Ag nanocrystals-decorated carbon nanotubes (MWCNTs/Ag, SWCNTs/Ag), Ag nanocrystals (NCs) were produced by physical vapor deposition using a mini-arc plasma reactor.[147] The mini-arc plasma was generated between two carbon electrodes, and small pieces of Ag (purity: 99.999%) cut from an Ag wire were used as the precursor material. After Ag was vaporized by the mini-arc plasma source, the Ag vapor was carried by an Ar flow (3 lpm) downstream and quenched through natural cooling in the copper tubing to form Ag NCs in the gas phase. The as-produced Ag NCs were directly deposited onto CNTs on gold electrodes using an electrostatic force-directed assembly (ESFDA) process.[162] After deposition, the CNTs/Ag hybrid sensor was annealed at 200 °C for 1 h in Ar flow (1 lpm) to improve the contact between Ag NCs and MWCNTs.

The morphology and crystal structure of the MWCNT/Ag NP hybrids were studied with an SEM (Hitachi S4800) and an HRTEM (Hitachi H-9000-NAR) with 0.18 nm point and 0.11 nm lattice resolution when operated at an accelerating voltage of 300 kV.

3.1.2 Sensor fabrication and structural characterization

Sensor devices were fabricated using a similar process as reported before.[163, 164]

Interdigitated gold electrodes with finger width and inter-finger spacing of 2 μm and a thickness of 50 nm were fabricated using e-beam lithography on a silicon substrate with a SiO_2 thin top layer. To bridge the gold electrodes with MWCNTs, MWCNTs (20–30 nm in diameter, Alpha Aesar) were first uniformly dispersed in *N,N*-Dimethylformamide (DMF) by ultrasonication. Then a tiny drop (1 μl) of MWCNTs suspension was drop cast on the gold electrodes. After DMF evaporated, MWCNTs were left, connecting the gold fingers. The amount of MWCNTs on gold electrodes can be controlled by adjusting the dispersion concentration. With a low concentration, only a few MWCNTs were found bridging the gold electrode fingers. Further annealing treatment at 200 $^\circ\text{C}$ for 1 h in Ar flow (1 lpm) was carried out to remove the residual DMF and to improve the contact between MWCNTs and gold electrodes.

Semiconducting SWCNTs (s-SWCNTs) were assembled on gold electrodes using a dielectrophoresis process.[165] An arbitrary waveform function generator (Keithley 3390) was used to supply the ac voltage. First, s-SWCNTs (IsoNanotubes-S, 98%, 0.01 mg ml^{-1} , NanoIntegris) was diluted in DI water and sonicated for 10 min, forming a 0.2 $\mu\text{g ml}^{-1}$ uniformly distributed dispersion. Then a 3 μl droplet of the dispersion was drop cast on the electrodes. An ac voltage of 2 V (sine wave) at a frequency of 1 MHz was applied to the electrodes for 3 min. After the dielectrophoresis, the electrode was rinsed with DI water and dried with an air gun. A further annealing treatment at 350 $^\circ\text{C}$ for 1 h in Ar flow (1 lpm) was carried out to improve the contact between s-SWCNTs and gold electrodes.

3.1.3 Ammonia sensing measurements

A sensor was placed into an air-tight sensing test chamber with electrical feedthroughs (Figure 3.1). A constant dc voltage was applied to the electrodes bridged by CNT/Ag NP hybrids. Ammonia was detected by monitoring and recording the change of electrical current passing through CNTs using a Keithley 2602 source meter (Keithley, Cleveland, OH). One typical sensing test cycle has three continuous sequential steps: First, a clean dry air flow (2 lpm) was introduced into the sensing chamber as a background. Then, a test gas of NH_3 diluted in air was injected into the chamber with the same flow rate (2 lpm) to register a sensing signal. Finally, a clean dry air flow (2 lpm) was introduced again for sensor recovery. Multiple testing cycles were performed by continuously repeating the same test for several times. The concentration of NH_3 was varied between 0.125% and 1%.

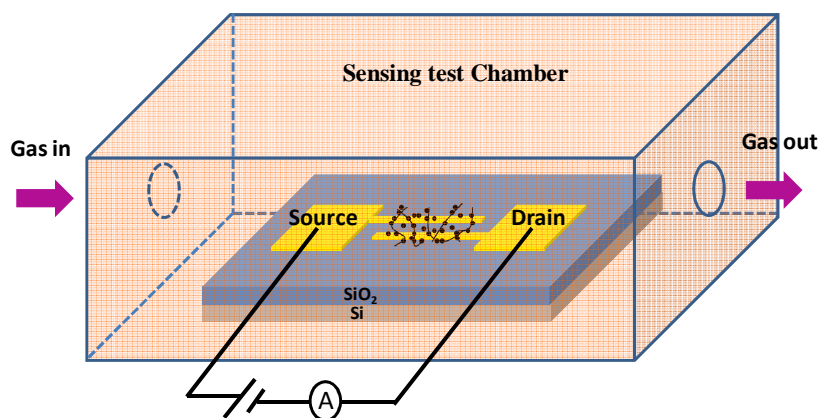


Figure 3.1 Schematic experimental setup for sensing measurements.

3.2 Results and discussion

3.2.1 MWCNTs/Ag hybrid ammonia sensors

Figure 3.2a shows the SEM image of a typical MWCNT/Ag NP hybrid bridging a pair of gold electrode fingers in a realistic sensor device. The two gold electrode fingers acted as source and drain electrodes during the electrical measurements, and the MWCNT/Ag NP hybrid was the conducting channel as well as the active sensing material. Since MWCNTs have relatively larger diameters than SWCNTs, the resistance of MWCNTs is low. MWCNTs typically show more metallic behavior than SWCNTs because of the decreasing energy band gap with the increasing diameter.[163, 166] In this study, a small number of MWCNTs was used. Figure 3.2b is a close-up view of the MWCNT/Ag NP segment boxed in Figure 3.2a, showing the detailed morphology of the MWCNT/Ag NP hybrid structure. A TEM image of the hybrid structure is shown in Figure 3.2c. It is evident that Ag NCs decorate MWCNTs in a non-continuous manner, and the NCs distribution is quite uniform. The size of Ag NCs ranges from several nanometers to about 10 nm. The inset in Figure 3.2c shows an SAED pattern of the hybrid proving that the Ag nanoparticles are crystalline. Besides the innermost ring, which belongs to MWCNTs, the other four bright rings are indexed to cubic fcc (111), (200), (220), and (311) lattice planes of Ag metal from the inside to the outside.[143] Figure 3.2d shows an HRTEM image of an individual MWCNT decorated with Ag NCs. The measured lattice spacing of 0.235 nm for the NCs corresponds to (111) plane of Ag. The smaller nanoparticles are single crystal, the larger ones exhibit stacking faults often seen in colloidal gold and silver NCs. In addition to the rounded edges, the nanoparticles have some flat facets

corresponding to the most densely packed $\{111\}$ surface plane terminations.

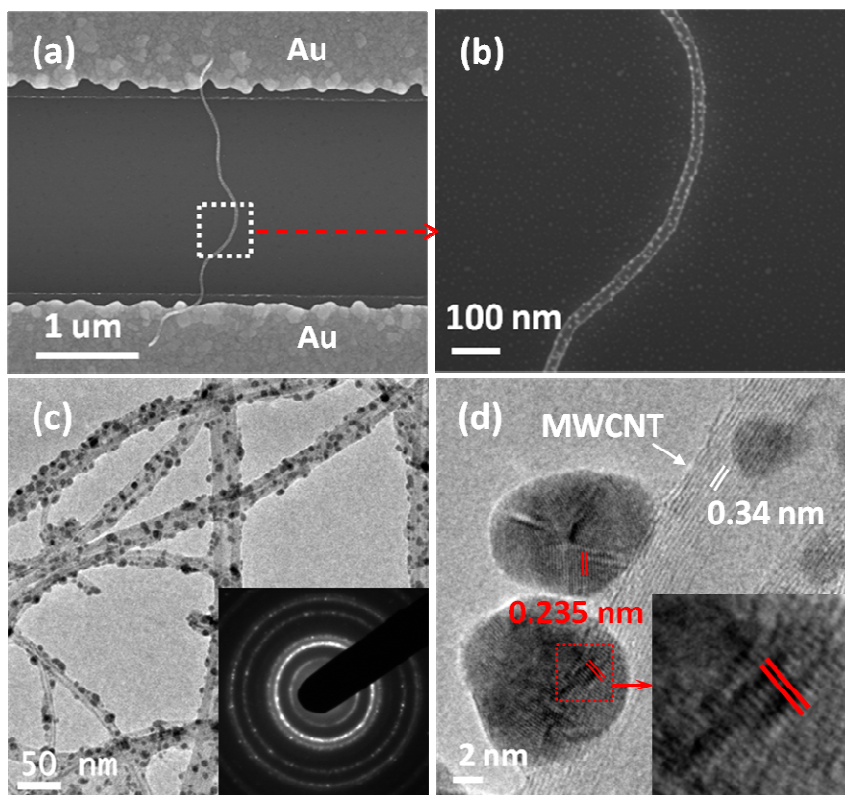


Figure 3.2 (a) SEM image of a single MWCNT decorated with Ag NPs connecting two gold electrode fingers. (b) SEM image of the enlarged view of the MWCNT/Ag NP structure as marked in (a). (c) TEM image of MWCNT/Ag NP hybrid structures. The inset is an SAED pattern of the hybrid demonstrating Ag crystallinity. (d) HRTEM image of MWCNT/Ag NP hybrid nanostructures. The inset is the enlarged view of Ag structure as marked on the Ag NC.

Figure 3.3a shows the I - V characteristics of MWCNTs before and after Ag NPs deposition. The straight lines (linear I - V relation) indicate that the contacts between the MWCNTs and the gold electrodes are Ohmic, which is consistent with our previous report.[163] In our experiments, annealing treatment at 200 °C for 1 h in Ar flow was performed after the MWCNT deposition to improve the electrical contacts. According to the literature,[167] MWCNTs show more metallic behavior than SWCNTs, and the

outermost shell of MWCNT is responsible for the electrical transport. Therefore, even with a smaller contact area compared with the use of additional Pt or Au deposition to enhance the CNT–electrode contact, charge carriers can still flow smoothly between MWCNTs and gold electrodes after the annealing.

Therefore, the Schottky barrier (SB) between the MWCNT and the electrodes was minimized in our sensor and the main mechanism of sensing is a direct charge transfer between the adsorbed gas molecules and the MWCNTs/Ag.[168] Based on the measurements, the resistance of bare MWCNTs is ~ 3.4 k Ω , indicating typical good conductance of MWCNTs. After Ag NPs deposition on the MWCNTs and annealing in an Ar atmosphere, the resistance of MWCNTs decreased to a value of ~ 3.1 k Ω . Knowing from microscopic images that Ag NPs do not form interconnected conducting pathways along MWCNTs, it is logical to attribute the decrease in resistance to a net charge transfer between the Ag NPs and MWCNTs. It is well known that Ag is a catalytic material and can dissociate and chemisorb O₂ in the presence of oxygen molecules under atmospheric conditions.[16] Thus, nano-scopic electron depletion zones form around Ag NPs because of surface oxidation, which gives rise to so-called nano-Schottky barriers. The work function of these regions (5.4 eV–5.6 eV) [169] is higher than those of MWCNTs (4.7 eV–4.9 eV) [16], which allows a net electron transfer from MWCNTs to Ag NPs and causes a decrease in the electrical resistance.[170]

Ammonia sensing tests were performed in an air-tight chamber at room temperature. A constant dc bias of 2 mV was applied between the source and drain electrodes, and the current passing through the MWCNTs/Ag was recorded. As shown in Figure 3.3b, the I – V

characteristics of the sensor exhibit linear behavior both in the airflow and in the NH_3 flow, indicating that the Ohmic contact between the hybrid and the gold electrode is not disturbed by the gas flow. The linear I - V curve in NH_3 flow (dashed red line) has a smaller slope than that in airflow (solid blue line), indicating the resistance of the MWCNT/Ag NP hybrid increased after exposure to NH_3 due to the gas molecule adsorption and a net charge transfer between gas molecules and the hybrid. To compare the sensing performance of MWCNTs before and after Ag NPs deposition, bare MWCNTs were tested first against NH_3 . Then the same sensor was tested again after being coated with Ag NPs. The dynamic response of both bare MWCNTs and MWCNT/Ag NP hybrids to 1% NH_3 is shown in Figure 3.3c. The sensitivity (S) is defined as $\Delta R/R = (R_g - R)/R$, where R is the average sensor resistance in the air before test gas exposure, while R_g is the sensor resistance after exposure to a test gas. From Figure 3.3c, it can be seen that a maximum sensitivity of $\sim 2.8\%$ is achieved for bare MWCNTs with 10 min exposure to 1% NH_3 . For MWCNT/Ag NP hybrids, however, the sensitivity is $\sim 9.0\%$ with the same exposure time, and it reaches $\sim 8.0\%$ instantly. This sensitivity of MWCNT/Ag NP hybrids for 1% NH_3 exceeds that of Ag mesowire arrays for NH_3 sensing, which showed $\sim 5\%$ response to NH_3 with $>1\%$ concentration.[171] For Ag film prepared with the same method as Ag mesowires, the sensitivity was $<5\%$.[171] Therefore, the MWCNTs/Ag sensor has high sensitivity toward NH_3 , and Ag NCs play a critical role in enhancing gas sensitivity.

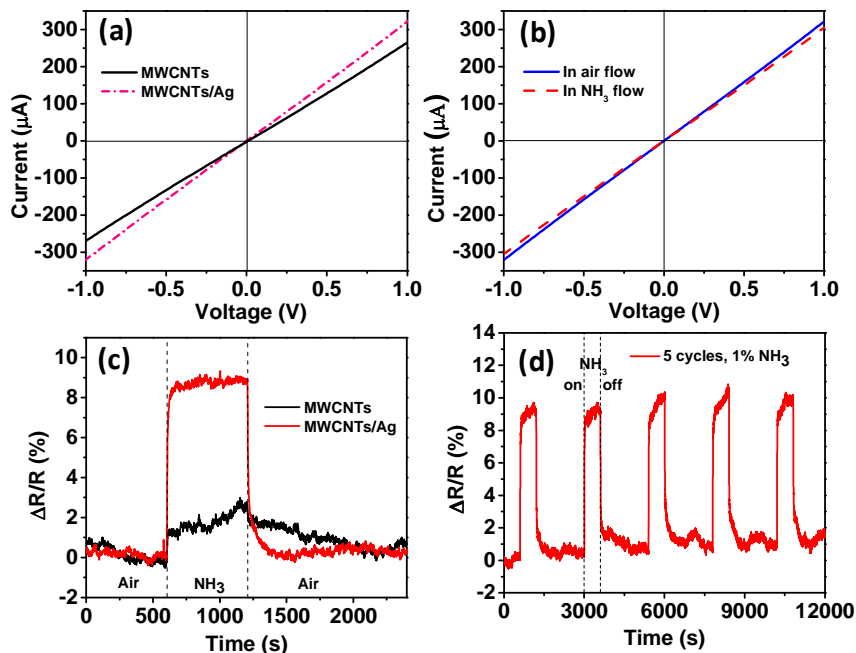


Figure 3.3 (a) I - V characteristics of MWCNTs before and after Ag NPs decoration. (b) I - V characteristics of MWCNT/Ag NP hybrid sensors in airflow and in 1% NH_3 flow. (c) The room temperature dynamic sensing response ($\Delta R/R$) before and after Ag NPs decoration. (d) Five sensing cycles of the MWCNT/Ag NP hybrid sensor to 1% NH_3 , indicating a good stability.

The sensing mechanism of MWCNT/Ag hybrids was studied. Previous theoretical studies showed that NH_3 interacts weakly with pristine CNTs with little charge transfer, in agreement with the low sensitivity results in this work.[168, 172, 173] Therefore, the Ag NPs could strengthen the NH_3 sensing performance of the hybrid structure by acting as the dominant active adsorption regions for NH_3 in our hybrid sensor. For atmospheric pressure and room-temperature operation of such a sensor, it is important to consider the effects from oxygen, especially because silver is a semiprecious metal. Based on the literature, oxygen molecules can be dissociated and adsorb on a clean Ag surface resulting in an oxide monolayer structure.[174] An extra negative charge is taken by the oxygen because the electro negativity of oxygen is higher than that of Ag.[175] These oxygen ions lead to electron depletion regions (nano-Schottky barrier) at the Ag NP surfaces,

providing more effective adsorption sites for ammonia. Since the electron affinity of silver (2.0–2.5 eV) is high, NH_3 (electron donor) is more likely to interact with Ag atoms on the oxidized Ag surface.[175] Thus, the oxidation state of Ag was reduced by the charge transfer, which leads to the electronic state change and a conductance change in the MWCNTs channel, which is called “electronic sensitization.”[138] Since the MWCNT is a p-type semiconductor in atmosphere, the charge transfer from Ag into the MWCNT causes depletion of holes in MWCNTs and an increase in the electrical resistance.

For gas sensors, sensing response time is one of the most important properties. We have extracted the sensing response time of our sensor by defining the response time as the time needed for the sensor to change over 63.2% of the maximum sensitivity (corresponding to one time constant in a first-order dynamic system). An analysis of Figure 3.3c shows that the response time for the MWCNTs/Ag hybrid sensor is ~7 s. It is comparable with that of an Ag mesowire NH_3 sensor (~5 s) for gas concentrations above 1% [171]. It is also comparable with the ultrafast room-temperature NH_3 sensor made of reduced graphene oxide (RGO), which has a response time of ~10 s.[176] But the RGO sensor has to be gated with a positive voltage (e.g., +40 V). Otherwise, the response is on the order of minutes.[177, 178] In contrast, the response time is ~344 s for the bare MWCNTs sensor. So it is clear that Ag NCs dramatically improve the sensing response. MWCNTs have very high carrier mobility ($>100,000 \text{ cm}^2/\text{Vs}$),[179] and the electronic state of MWCNTs would change rapidly with the change of the Ag oxidation state (Otherwise, the response for any gas is slow). Therefore, the response time could be

mainly determined by the charge transfer between the gas molecules and Ag NPs. The fast response of our sensor suggests that NH_3 can easily adsorb on an Ag surface with a fast charge transfer. This also can be evidenced by a relatively flat response plateau after the rapid increase upon gas exposure, indicating that the Ag surface are saturated with NH_3 molecules after a short period of time.

The sensor recovery process was carried out in dry air. From Figure 3.3c, it can be seen that the sensor can recover to the initial state within 5 min. We have analyzed other sensing cycles, and the average time for full recovery was about 7 min, which is much shorter than that (12 min) of the positively-gated RGO NH_3 sensor.[176] For an RGO without a positive gate, it will take hours or days to complete the full recovery.[177, 178] Here, we defined the recovery time as the time needed for the sensor to recover over 63.2% of the maximum sensitivity. According to the data analysis for our sensor, the recovery times are ~15 s and ~410 s for the MWCNT/Ag NP hybrid and bare MWCNTs, respectively. Generally, it takes a very long time (more than overnight with our experiments) for the CNTs to recover to its initial state at room temperature, which could be attributed to the high binding energy between NH_3 molecules and CNT defects and the adsorbed oxygen.[168, 172] However, in the MWCNT/Ag NP hybrid sensor, Ag NPs could occupy these sites and become the dominating sensing element. The fast recovery speed suggests that the desorption barrier on the Ag surface is low for NH_3 molecules, probably because of the low binding energy. To study the stability of the MWCNT/Ag NP hybrid sensor, five sensing cycles (as shown in Figure 3.3d) to 1% NH_3 were performed at room temperature. The sensing behavior appears quite repeatable.

Figure 3.4a shows the dynamic response ($\Delta R/R$) of the MWCNT/Ag NP hybrid sensor when exposed to different concentrations (C) of NH_3 . The sensitivity increases monotonically from $\sim 5\%$ – 9% with increasing gas concentrations from 0.125% – 1% . Figure 3.4b plots the derived sensor response as a function of NH_3 concentrations. It can be seen that the sensor sensitivity increases rapidly when the gas concentration is relatively low. At higher gas concentrations, it becomes saturated probably because of lacking Ag surfaces for further gas adsorption. This curve can be well described by the following equation:[180]

$$S = \frac{\alpha}{1 + \frac{\beta}{C}}$$

where $\alpha = 0.1115$, which is a constant without unit, and $\beta = 1.7148 \times 10^{-3}$, which is a constant with the same unit as concentration (%). The linear fitting of $1/S$ versus $1/C$ is shown in the inset of Figure 3.4b, which can be explained with the Langmuir isotherm.[180, 181] When the concentration is in the lower region (about $<0.4\%$ in our case), the equation could be simplified as $S = (\alpha/\beta) \times C$, which suggests that the sensitivity and the concentration have a linear relationship. Meanwhile, high concentrations of ammonia tend to lead to a saturated response behavior.

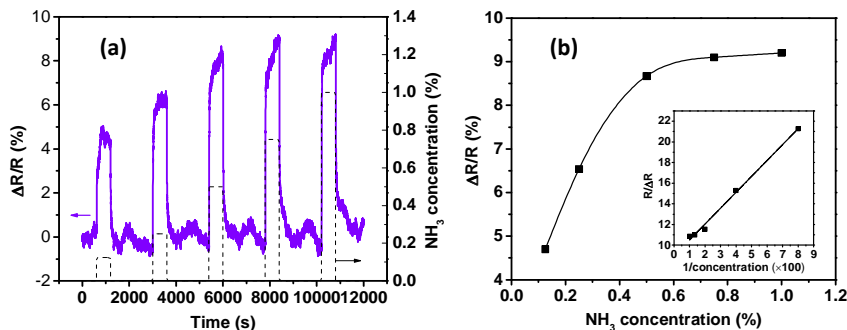


Figure 3.4 (a) The dynamic response ($\Delta R/R$) of the MWCNT/Ag NP hybrid sensor when exposed to different concentrations (C) of NH_3 . (b) Curve fit of the sensor response ($\Delta R/R$) as a function of NH_3 concentration. The inset is a linear fitting of $1/S$ ($R/\Delta R$) vs. $1/C$.

Selectivity is also an important property of a gas sensor. To understand the selectivity of our sensor, we measured the sensing response of the same MWCNT/Ag NP hybrid sensor to several other gases, including reducing gases such as H_2 and CO and an oxidizing gas such as NO_2 . The sensing test cycle is the same as that of measuring NH_3 . Our results show that the MWCNT/Ag NP hybrid sensor has excellent selectivity to NH_3 among all test gases. As shown in Figure 3.5, the sensor has negligible response to both 1% H_2 and 100 ppm CO. This result indicates that NH_3 is preferable for our MWCNT/Ag NP hybrid sensor among common reducing gases, which act as electron donors. Nitrogen dioxide is an oxidization gas and an electron acceptor. The sensing response to 100 ppm NO_2 shows that the resistance of the MWCNT/Ag NP hybrid sensor decreases, suggesting a charge transfer from the hybrid to NO_2 molecules. The sensitivity gradually increased to an absolute value about 4% within 10 min exposure at room temperature.

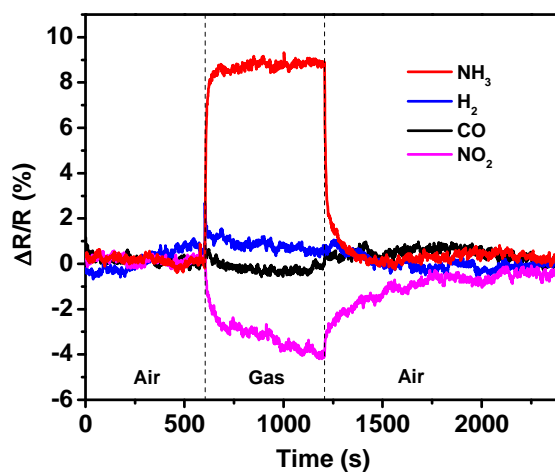


Figure 3.5 Comparison of sensing response to various gases.

The reliability of the MWCNT/Ag NP hybrid sensor was studied by comparing its original sensing performance with its performance after four-month storage in air. As shown in Figure 3.6, the sensor still responded well toward NH_3 with slight degradation after four months, which indicates that the sensor is relatively stable in air. The same sensor after four-month storage was also tested against different concentrations of NH_3 . The result (Figure 3.7) shows that the sensor can detect a concentration as low as 10 ppm, and the sensitivity gradually increased with increasing NH_3 concentrations ranging from 10 ppm to 10,000 ppm (1%).

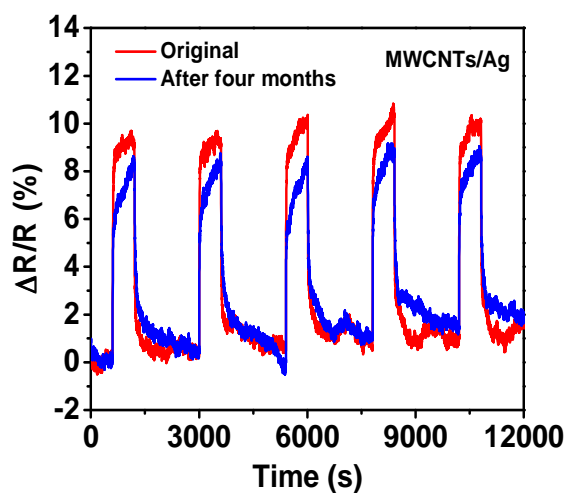


Figure 3.6 Comparison of sensing performance toward 1% NH_3 before and after four-month storage in air.

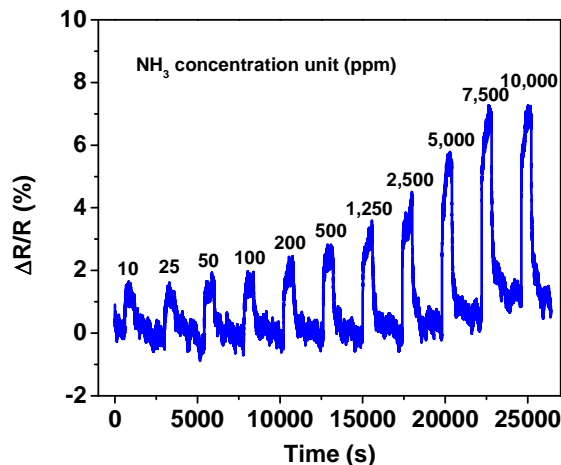


Figure 3.7 The dynamic sensing response of MWCNT/Ag NP hybrid sensor after four-month storage in air when exposed to different concentrations of NH₃. The concentration unit of NH₃ is parts per million (ppm).

3.2.2 SWCNTs/Ag hybrid ammonia sensors

Based on the study of MWCNT/Ag NP hybrids, Ag can dramatically enhance the sensing performance of MWCNTs. However, MWCNTs exhibit more metallic than semiconducting behavior. It is well known that semiconducting SWCNTs have excellent FET properties, and a small electron transfer induced by gas adsorption can cause a significant change in charge carrier concentration of SWCNTs. Therefore, SWCNT/Ag NP hybrids are expected to have even higher sensitivity and SWCNT/Ag hybrids were synthesized for ammonia detection in this study.

After SWCNTs were assembled on the electrodes, the morphology of SWCNTs was characterized by SEM. Figure 3.8a shows an SEM image of typical SWCNTs bridging a pair of gold electrode fingers in a sensor device. The SWCNTs were also characterized using HRTEM (Figure 3.8b), which shows that these SWCNTs are about 2 nm in

diameter as indicated by the red arrows. The I - V characteristic of SWCNTs is shown in Figure 3.9a, and the slightly non-linear curve is likely due to the Schottky contact between the semiconducting SWCNTs and gold electrodes. The work functions of SWCNTs and gold are 4.5 eV and 5.3 eV, respectively.[182] The difference of the work functions between SWCNTs and gold electrodes causes electron transfers across the interface, leading to an electric field formation around the interface thus a Schottky barrier (SB). The resistance of the device is $9.8 \times 10^5 \Omega$. The FET characteristic indicates p-type semiconducting behavior and a very high on-off current ratio (80.5). The device could be completely shut off at a gate voltage of 25 V (Figure 3.9b).

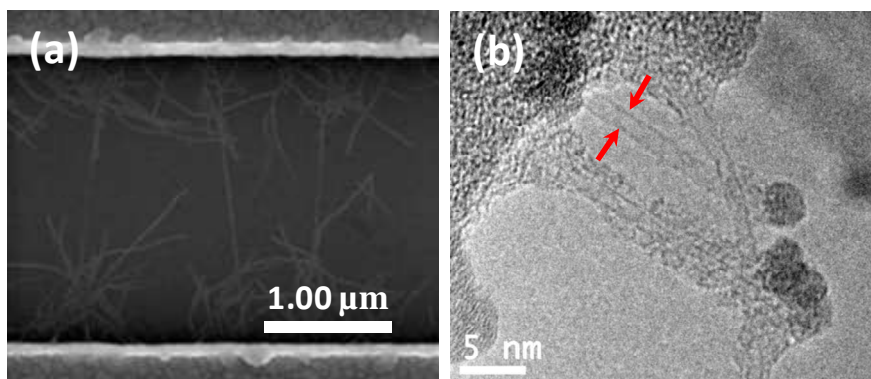


Figure 3.8 (a) SEM image of SWCNTs bridging a gold electrode gap and (b) HRTEM image of SWCNTs.

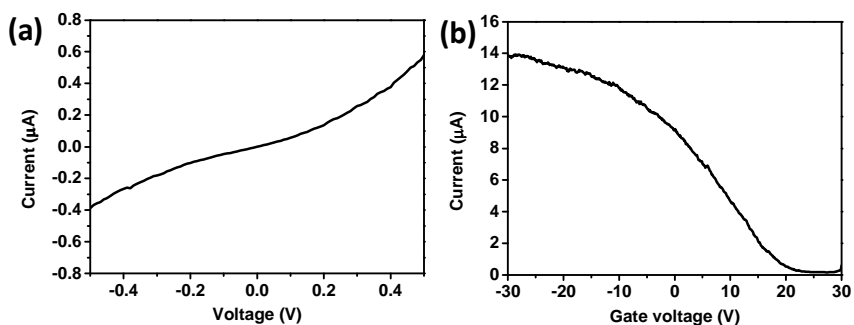


Figure 3.9 (a) I - V and (b) FET characteristics of bare SWCNTs.

Figure 3.10 shows SEM images of SWCNTs before and after Ag NP decoration. It is evident that the Ag NPs distribute homogeneously/uniformly on the surface of SWCNTs. The dynamic sensing responses for SWCNTs before and after Ag NP decoration are compared in Figure 3.11a, and the results demonstrate that the sensitivity of SWCNTs decreased dramatically from 3.18 to 0.36 after the Ag deposition for 15 min, which is opposite to the sensitivity enhancement of Ag NPs on MWCNTs. Calculations have been carried out to predict the interaction between various gas molecules and the sidewalls of pristine SWCNTs, and some molecules, such as NH_3 , interact weakly resulting in a minimum electron transfer with the nanotube sidewalls.[173] However, experimental observations indicated a significant charge transfer from ammonia to SWCNTs.[126] A desorption energy of about 1 eV/molecule was found for NH_3 due to the defects on the sidewalls of SWCNTs.[183] Therefore, the defect sites seem more active than pristine sidewalls and contribute significantly to the observed sensing response. Figure 3.11a also demonstrates our SWCNTs have a significant response toward 1% NH_3 likely due to the defects on the sidewalls. However, the Ag NP deposition leads to a decreased sensing response of SWCNTs, which can be attributed to two aspects. One is that the NH_3 binding energy on Ag NPs (0.36 eV)[184] is lower than that on defect sites (0.53 eV)[185] and the other is that some of the defect sites are occupied by Ag NPs so that the number of adsorption sites on SWCNTs is reduced after the Ag NP deposition. Therefore, less electron transfer occurs from NH_3 to SWCNTs through Ag NPs after adsorption, leading

to less reduction in the charge carrier concentration in SWCNTs, thus less change in the electrical conductance.

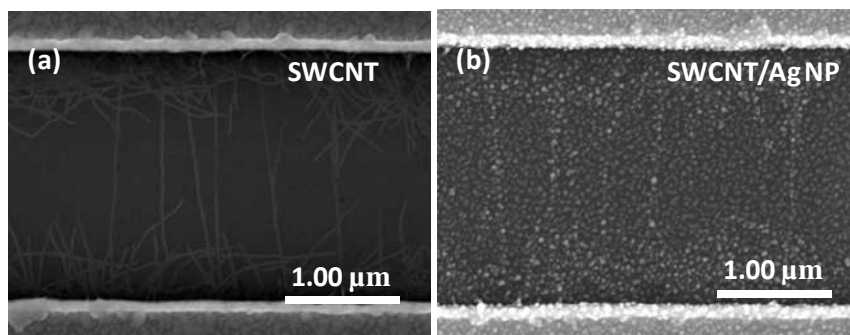


Figure 3.10 SEM images of SWCNTs before (a) and after (b) Ag NPs deposition.

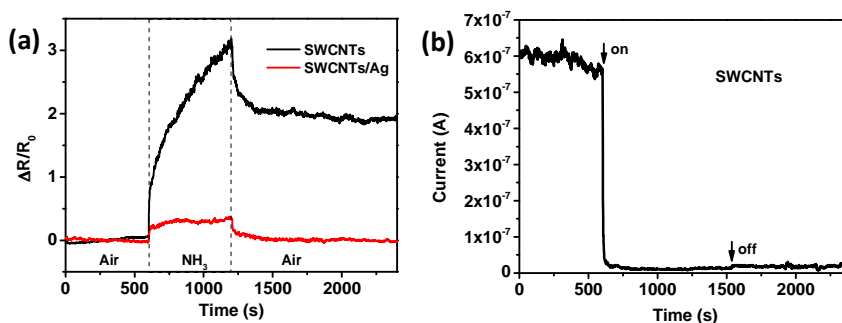


Figure 3.11 (a) Room-temperature dynamic sensing responses of SWCNTs before and after Ag NPs decoration when exposed to 1% NH_3 . (b) Dynamic sensing response to 1% NH_3 for bare SWCNTs sensor with low SWCNT loading density.

The effect of Schottky barrier at the interface of gold electrodes and SWCNTs on gas sensing has been measured and it was found that SB modulation dominated the gas sensing performance at room temperature.[168] The work function of Au electrode is reduced when NH_3 molecules are adsorbed on the SWCNT/Au interface. Then the electric field at the interface is changed, leading to an increase of SB. However, there was also study reporting that the SB has a negligible effect on the conductance change of

SWCNT networks for NH_3 sensing.[185] In this study, we used SWCNT networks in the sensors, and both the SB- and gas-induced electron transfer between SWCNTs and NH_3 molecules is responsible for the sensing signal. SB-dominated sensor typically features long recovery time and more signal noise.[168] However, our sensing signal is quite smooth and the sensing response recovered fast for Ag NP-decorated SWCNTs sensors, which suggests that the electron transfer mechanism dominates the sensing performance for our sensors.

According to a previous report, when a small fraction (~2%) of carbon atoms in SWCNT were oxidized to introduce defects, the charge transfer increased by 1,000% upon gas adsorption.[172] This indicates that a small number of defects can significantly modulate the gas sensing performance of SWCNTs likely due to the high binding energy on defect sites and high semiconducting property. However, the defects in MWCNTs cannot obviously enhance the sensitivity which is reflected from our experimental results that MWCNTs have a low sensitivity for both NH_3 and NO_2 .[186] An adsorption energy of 0.173 eV was reported for NH_3 on MWCNTs,[187] which is much lower than that on Ag NPs (0.36 eV). Therefore, the NH_3 adsorption capability on MWCNTs is enhanced by Ag NPs deposition. Thus, Ag NPs on MWCNTs can enhance the sensitivity, which is opposite to Ag NPs on SWCNTs.

Fortunately, the response time and recovery of the SWCNT sensor were both improved by Ag NP decoration. Based on the analysis, the response times are 210 s and 12 s for bare SWCNTs and SWCNT/Ag hybrids. Therefore, Ag NPs definitely improved the response speed of SWCNTs, which is consistent with MWCNT/Ag hybrid sensors.

For the sensor recovery, the binding energy of NH_3 on bare SWCNTs is sufficiently high so that the adsorbate remains attached to SWCNTs for a very long time in normal atmosphere.[188] To further prove this, another sample was assembled and tested against 1% NH_3 using the same process (Figure 3.11b). The sensor had a significant response under exposure to NH_3 . However, the recovery was negligible in air flow. Even after several days, there was still no obvious recovery. Typically, ultraviolet light can be used to accelerate the desorption of adsorbates.[189] In this study, because Ag NPs occupy defect sites on SWCNTs and become dominant active sites, the desorption energy is dependent on the Ag surfaces. According to our theoretical study, low binding energy was found for NH_3 on Ag surfaces,[184] resulting in a low desorption barrier and thus fast recovery. Therefore, the SWCNT/Ag hybrid sensor recovered to its initial status in a few minutes (Figure 3.11a).

Based on our results, the sensitivity of SWCNTs was significantly influenced (reduced) by the surface occupation of Ag NPs. To further investigate the effect of Ag loading densities on the sensor performance, the sensing responses were measured for one sensor with two different Ag loadings of 5-min and 15-min deposition time, respectively. Figure 3.12 shows the SEM images of devices with different Ag NP loadings. The loading density obviously was increased with longer deposition time. The images indicate that Ag NPs distribute uniformly over the entire surface of SWCNTs. The dynamic sensing responses, shown in Figure 3.13a, indicate that sensors with a higher loading density of Ag NPs have lower sensitivity but improved recovery, which is consistent with the trend of the SWCNT sensing with and without Ag NPs. It is also evident that the

defects on the sidewalls of SWCNTs play a significant role in the sensing response. With a higher density of Ag NPs, more defects are occupied and a lower sensitivity results. Here, the response times are 3 s and 6 s for SWCNTs loaded with Ag NPs of 5-min and 15-min deposition time, respectively, which further confirms the fast sensor response after the Ag NPs deposition.

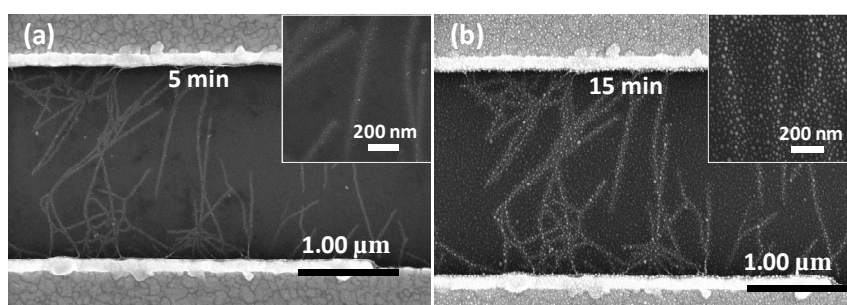


Figure 3.12 SEM images of SWCNTs coated with different loadings of Ag NPs: (a) low loading with 5-min deposition of Ag NPs and (b) high loading with 15-min deposition of Ag NPs.

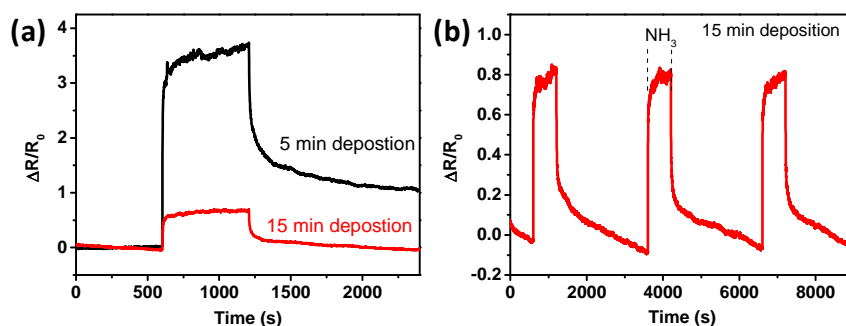


Figure 3.13 (a) Dynamic sensing evolution of SWCNTs with different Ag NP loadings. (b) 3-cycle sensing performance of SWCNT/Ag hybrids with Ag NPs deposition time of 15 min.

Although the sensitivity (0.83) for Ag NP loading of 15-min deposition decreased greatly compared with that (3.5) of 5-min Ag NP deposition, it is still much higher than that (0.09) of MWCNT/Ag hybrid ammonia sensors with a similar Ag loading density.[184] This can be explained by the intrinsic electrical behavior of MWCNTs and

s-SWCNTs. Compared with MWCNTs, s-SWCNTs show excellent semiconducting behavior and have a much lower charge carrier (holes) concentration. Therefore, the Fermi level shifts caused by the electron transfer correspond with a substantial change of charge carrier densities in SWCNTs and thus a significant change in electrical conductance. However, MWCNTs exhibit more metallic behavior, and the same electron transfer does not lead to a substantial change in the density state at Fermi level and thus the charge carrier concentration.[126] To study the stability of SWCNT/Ag hybrid sensors, three-cycle sensing performance was measured for 1% NH₃ using the same sensor with Ag NP loading of 15-min deposition (Figure 3.13b). The sensing responses are quite consistent and repeatable.

To further investigate the influence of defects on the sensing performance, SWCNTs were decorated with SnO₂ NPs synthesized by a physical vapor deposition method using a mini-arc plasma as the source as described in Chapter 2. Figure 3.14 shows SEM images of SWCNTs with and without SnO₂ NPs. The sensing response of SWCNT/SnO₂ hybrids was measured for 1% NH₃ and the result indicates that SnO₂ NPs also reduce the sensitivity of SWCNTs (Figure 3.15a), which is not surprising because SnO₂ is relatively insensitive to NH₃. [186] The defect sites on SWCNTs are occupied by the SnO₂ NPs, leading to the significant decrease in sensitivity. NO₂ is another pollutant that bare SWCNTs are very sensitive to.[126] We also found that SnO₂ NPs are sensitive to NO₂ and can enhance the sensitivity of MWCNTs.[186] However, according to the sensing response in this study, the sensitivity of SWCNT/SnO₂ is lower than that of bare

SWCNTs (Figure 3.15b), which suggests the adsorption energy of NO_2 on defects is also higher than that of NO_2 on SnO_2 NPs.

Our sensing results also show that SWCNTs are insensitive to H_2 and CO . Figure 3.15c shows the dynamic sensing response of SWCNTs toward 100 ppm CO and 1% H_2 and there is no response upon exposure to the test gases (Figure 3.15c). When the SWCNTs are decorated with SnO_2 NPs, a response occurs with an increased resistance (Figure 3.15d), indicating the electron transfer is from gas molecules to p-type SWCNTs. Here, the SnO_2 NPs serve as the active sites to interact with H_2 and CO , which agrees well with our previous report.[164]

Therefore, we can conclude that the defects on SWCNTs are very sensitive to NH_3 and NO_2 . The binding energy between the defects and NH_3/NO_2 is much higher than that between NH_3/NO_2 and Ag/SnO_2 NPs, resulting in decrease in sensing response to NH_3 after the NP deposition on SWCNTs. However, for gases that SWCNTs are insensitive to, such as H_2 and CO , the active NPs on SWCNTs can enhance the sensing performance.

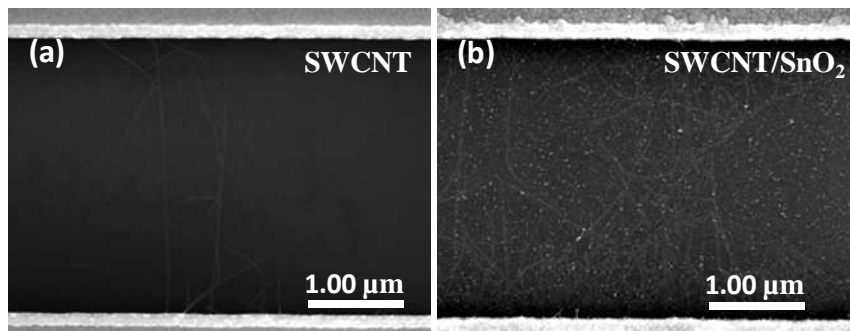


Figure 3.14 SEM images of SWCNTs between a gold electrode gap before (a) and after (b) SnO_2 NPs deposition.

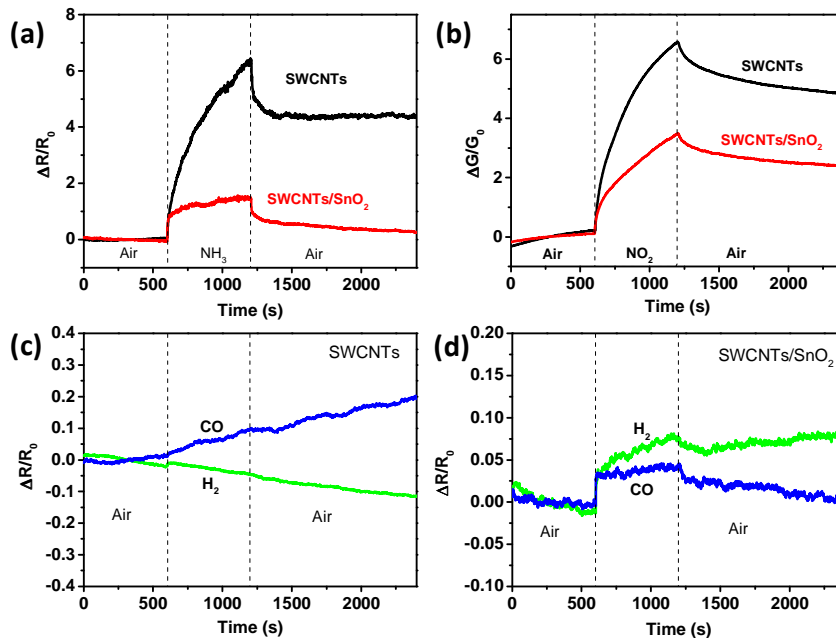


Figure 3.15 Room-temperature dynamic sensing evolution of SWCNTs before and after SnO₂ NPs decoration to (a) 1% NH₃ and (b) 100 ppm NO₂. Dynamic sensing response of (c) bare SWCNTs and (d) SWCNT/SnO₂ hybrids to 100 ppm CO and 1% H₂.

3.3 Summary and conclusions

We have demonstrated fabrication and application of CNT/Ag hybrid structures for room-temperature NH₃ gas sensors. The as-produced MWCNT/Ag hybrid sensor showed much higher sensitivity than MWCNTs alone. Fast sensing response and recovery were also achieved by the deposition of Ag NPs on MWCNTs. The Ag NPs work as the dominant active sites for NH₃ adsorption in the sensing process. A net charge transfer from NH₃ to Ag quickly occurs after adsorption. The hybrid sensor also has an excellent selectivity to NH₃ because it prefers to respond to NH₃ instead of reducing gases such as H₂ and CO. For ammonia sensors based on semiconducting SWCNTs, Ag NP deposition leads to decreases in the sensitivity of SWCNTs due to stronger binding between gas molecules and defects on the SWCNT surface than that between gas molecules and Ag

NPs. Compared with MWCNT/Ag hybrids, SWCNT/Ag hybrids have much higher sensitivity due to the excellent semiconducting properties of SWCNTs. The change in the charge carrier concentration of SWCNTs caused by the electron transfer between gas molecules and SWCNTs results in a significant Fermi level shift of SWCNTs, corresponding to a significant change in the charge carrier concentration. Like Ag NPs, SnO₂ NPs decoration also reduces the sensitivity of SWCNTs for both NH₃ and NO₂, again confirming a high binding energy between SWCNT surface defects and gas molecules and significant effect of defects on SWCNT sensing.

CHAPTER 4 TERNARY HYBRID STRUCTURES BASED ON CNTS FOR GAS SENSING

4.1 Experimental methods

SnO₂ and Ag crystalline NPs were synthesized using a mini-arc plasma setup as introduced in Chapters 2 and 3.[162] SnO powders (99.9% purity, Alfa Aesar) were used as the source material for SnO₂ synthesis. The morphology and structure of the as-produced NPs were characterized by a conventional (phase contrast) TEM (Hitachi H-9000 NAR) operating at an accelerating voltage of 300 kV. HRTEM and SAED were carried out to verify the crystalline structure of the nanoparticles. SnO₂ and Ag NPs were also collected onto MWCNTs forming hybrid nanostructures. TEM and EDS characterization were performed for the hybrid structures as well.

The sensing device assembly and sensing tests were performed in several sequential steps. Firstly, MWCNTs were uniformly suspended in ethanol by sonication. Then a small drop (1 μ l) of the suspension was drop cast on a gold interdigitated electrode. Annealing the samples at 200 °C for 1 h facilitated the Ohmic contact between MWCNTs and gold electrodes. Electrical properties (*I-V* curves, FET measurements) and sensing tests were carried out after annealing. The same annealing and test cycles were conducted after coating SnO₂ and Ag NPs individually. Gas sensing measurements were carried out by sequentially introducing air flow and target gas flow into an airtight chamber in which a sensor was mounted. Since the Ag NPs adsorb and dissociate oxygen when exposed to air at room temperature,[16, 174] the as-prepared Ag NPs will always be considered to have

chemisorbed oxygen for this study. The flow rates for both gases were 2 lpm, which were controlled by mass flow controllers. The resulting changes in current between the electrodes were measured as a function of time at a fixed bias (1 mV). The sensor sensitivity (S) was evaluated as $|R_g - R_a|/R_a$, where R_g is the sensor resistance in the target gas and R_a is the mean sensor resistance in initial air flow which was used as the background/reference.

4.2 Results and discussion

The hybrid was synthesized by *in situ*, sequential assembly of discrete SnO₂ and Ag NPs onto the surface of MWCNTs (Figure 4.1a), which bridge the gold electrode gaps (Figure 4.1b). An SEM image of such a device consisting of the hybrid structure is shown in Figure 4.1c. The EDS spectrum (Figure 4.1d) confirms that the NPs consist of only Sn, O, and Ag. HRTEM imaging was used to obtain the structural information about the hybrid structure (Figure 4.1e). According to the characteristic lattice spacings, the particles can be identified as the rutile (tetragonal) phase SnO₂ and Ag. The SnO₂ nanocrystals are about 5 nm in diameter, and Ag nanocrystals are about 10 nm in diameter. Figure 4.1e also shows that both components in this hybrid structure can contact each other. The distinctive rings and spots on the SAED pattern (Figure 4.1f) further confirm that NPs on the surface of MWCNTs are crystalline. The diffraction rings highlighted in red arcs (from inside to outside) are indexed to rutile SnO₂ (110), (101) and (211) planes. The rings highlighted in green arcs (from inside to outside) are indexed to cubic fcc Ag (111),

(200), (220) and (311) planes.

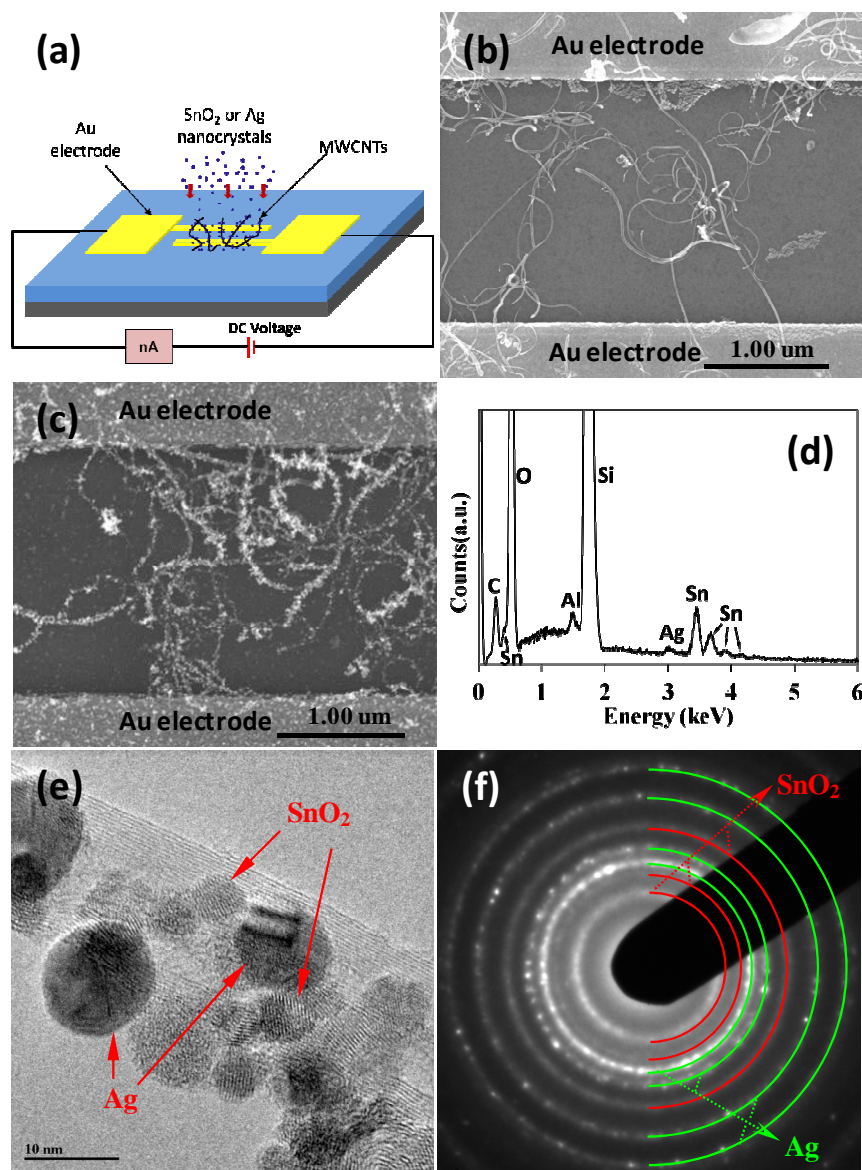


Figure 4.1 Schematic view of a device used for conductometric measurements. (b) and (c) are SEM images showing MWCNTs which are bridging two gold electrodes before and after NPs assembly, respectively. (d) is the EDS spectrum of the hybrid structure. Al and Si are from test support stage and Si wafer, and carbon is from the CNT. (e) and (f) are HRTEM image and SAED pattern of MWCNTs coated with both SnO_2 and Ag NPs.

The FET measurement results on bare MWCNTs and MWCNTs coated with NPs are shown in Figure 4.2. The linear I - V relationships indicate Ohmic contacts between

MWCNTs and gold electrodes (Figure 4.2a). It was found that the device electrical resistance changed greatly after coating SnO₂ NPs. MWCNTs are p-type semiconductors both before and after NPs deposition, which can be seen from Figure 4.2b. For p-type CNTs, resistance decreases with electrons transferring out of CNTs, while resistance increases by electrons transferring into CNTs. Here, the resistance decreased which can be explained as effective electron transfer from MWCNTs into NPs owing to the electron-depletion layer on the surface of SnO₂ NPs through adsorption of O₂. [163] Upon deposition of Ag NPs, the device resistance shows a further decrease. It is well known that Ag can dissociate and chemisorb O₂ in the presence of oxygen molecules under atmospheric conditions. [16] Therefore, nanoscopic electron depletion zones form around Ag NPs. The work function of these regions (5.4–5.6 eV) [169] is higher than that of SnO₂ NPs (4.7 eV) [190] and MWCNTs (4.7–4.9 eV), [16] leading to a net electron transfer from SnO₂ and MWCNTs to Ag NPs and a decrease in the CNT resistance.

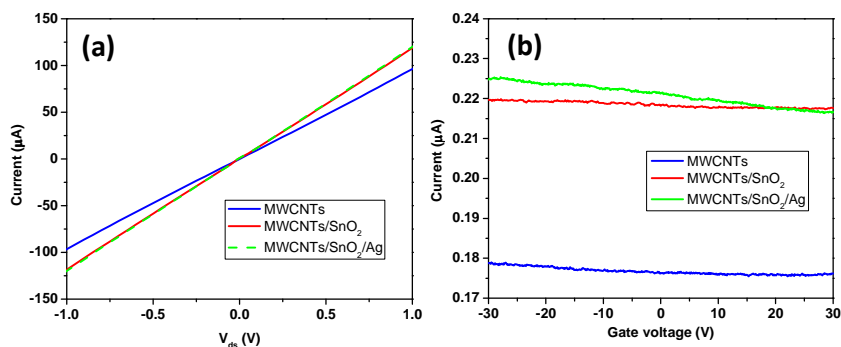


Figure 4.2 *I-V* curve evolution of MWCNTs at different conditions (with and without NP coating). (b) The dependence of current on gate voltage.

The dynamic sensing responses of MWCNTs before and after the deposition of these

specific types of NPs were first measured towards 100 ppm NO₂ at room temperature (Figure 4.3a). Clearly, functionalizing MWCNTs with SnO₂ alone or both SnO₂ and Ag NPs can lead to an enhancement in sensitivity and response time compared with bare MWCNTs (here the response time is defined as the time needed for the device resistance to change by 63.2% of the maximum difference during exposure to testing gas). For bare MWCNTs, the response time is ~ 224 s, which is relatively long. This is not surprising since the interaction between NO₂ and the CNT is quite weak. After NPs deposition, however, the response time was shortened to ~ 126 s and ~ 77 s for hybrid structures of MWCNTs/SnO₂ and MWCNTs/SnO₂/Ag, respectively. NO₂ is a typical oxidizing gas and withdraws electrons upon adsorption. Generally, the attraction of NO₂ to metal oxides is ascribed to the formation of a negatively charged NO₃ complex between NO₂ and atomic oxygen ions which are electron rich on the metal oxide surface. For SnO₂, apart from the fact that exposure to oxygen molecules at high temperature leads to some of the oxygen dissociated and chemisorbed on the surface, superoxide ion (O₂⁻) is the dominated oxygen ion species on the surface at room temperature.[139, 191] These chemisorbed oxygen ions are critical for the response of the sensor.[16]

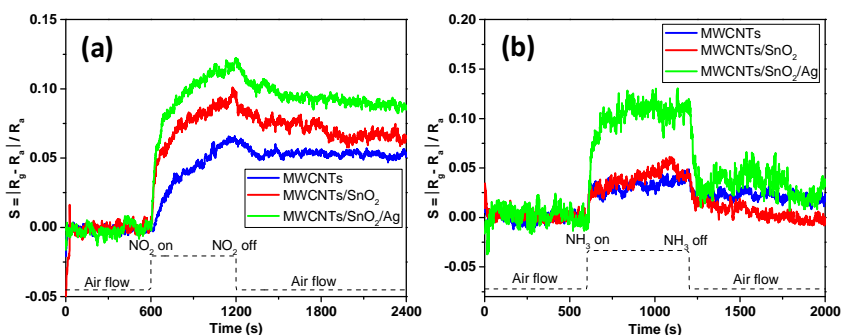


Figure 4.3 Sensing responses for bare MWCNTs and MWCNTs with partially covered NPs to (a) 100 ppm NO₂ and (b) 1% NH₃ at room temperature.

As shown in the experiment, Ag further enhanced the sensitivity to NO_2 . It is well known that Ag is a commonly used catalyst in surface chemistry and can be easily oxidized with exposure to air.[174] These surface oxygen ions around the Ag NPs lead to the formation of electron depletion zones (nano-Schottky barriers), which result in a change in the work function of Ag. The change of oxidation state of Ag (upon adsorption and desorption of the analyte) finally affects the electronic state of the MWCNTs, leading to a resistance change. This sensing mechanism is called “electronic sensitization”, which was proposed previously for promoters.[192]

With the above analysis, besides increasing the surface area of MWCNTs/ SnO_2 /Ag structures, the deposited Ag NPs greatly raise the quantity of chemisorbed oxygen on the surface of the hybrid structure, which leads to a greater and faster electron withdrawing from the structure when exposed to NO_2 . This process shifts the Fermi level of the CNTs further towards the valence band and finally it leads to the greater and faster resistance decrease of MWCNTs. However, due to the high binding energies of NO_2 on Ag and SnO_2 , it is reasonable that the recovery of the sensor toward NO_2 is quite slow as seen from Figure 4.3a. The full recovery time is fairly long, about 20 h. UV light has been used to shorten the recovery time by decreasing the desorption barrier.[83] Figure 4.4 shows the dynamic response of MWCNTs/ SnO_2 /Ag to 100 ppm NO_2 at room temperature for three cycles. Although the sensor could not recover to its initial state in a short period of time, it kept responding to NO_2 and the sensitivity increased toward a saturated status. It was reported that the adsorption energy decreases with increasing adsorbate coverage,

meaning that molecular adsorption will gradually decrease to a steady state.[193]

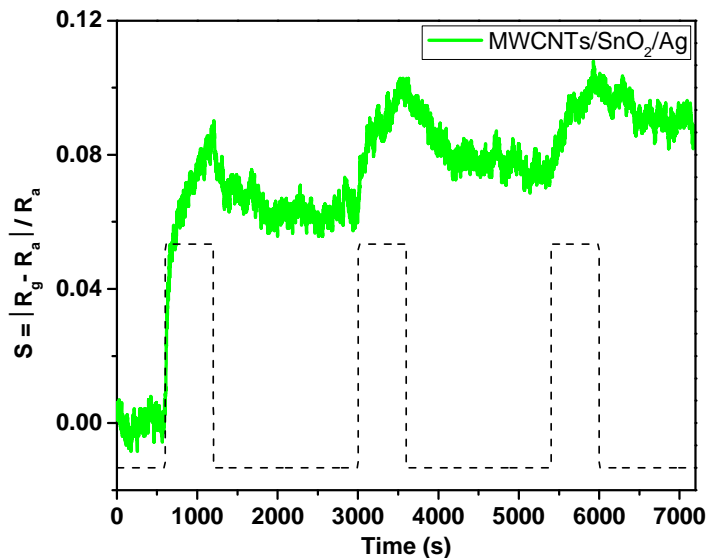


Figure 4.4 Representative sensing response of MWCNTs/SnO₂/Ag hybrid structures to 100 ppm NO₂ at room temperature.

The sensing response of bare MWCNTs, MWCNTs/SnO₂, and MWCNTs/SnO₂/Ag towards 1% NH₃ is shown in Figure 4.3b. All the sensors show a fast response to NH₃ at room temperature. After deposition of SnO₂ on MWCNTs, the sensitivity has no obvious change. However, after deposition of Ag NPs on MWCNTs, the sensitivity has a huge increase, about 157% that of MWCNTs. It is well known that pure CNTs are sensitive to NH₃ based on both theory and experiments.[194, 195] Nevertheless, the insensitivity of SnO₂ to NH₃ at room temperature is not fully understood and few studies have been reported. Hence, based on our experimental results and analysis, we conclude that Ag is the main promoter for NH₃ sensing in our sensor.

Since the electron affinity of silver (2.0–2.5 eV) is higher than that of tin (1.8 eV),

ammonia is more likely to bond with silver.[175] The NH_3 sensing on the Ag surface could be through the adsorption center $\text{Ag}^{\delta+}-\text{O}^{\delta-}$ forming on the surface of Ag_2O . The unshared electron pair in the molecule could transfer to silver at room temperature, forming $\text{Ag}-\text{N}^{\delta+}$. [175] An alternative mechanism suggests that NH_3 reacts with adsorbed oxygen ions, and is reduced into N_2 , accompanying electrons donation.[196] To further verify the interaction between silver and NH_3 , density functional theory (DFT) calculation was carried out in our group. The results indicate that NH_3 is adsorbed above the hollow region with H atoms pointing downwards and attracted to Ag atoms.

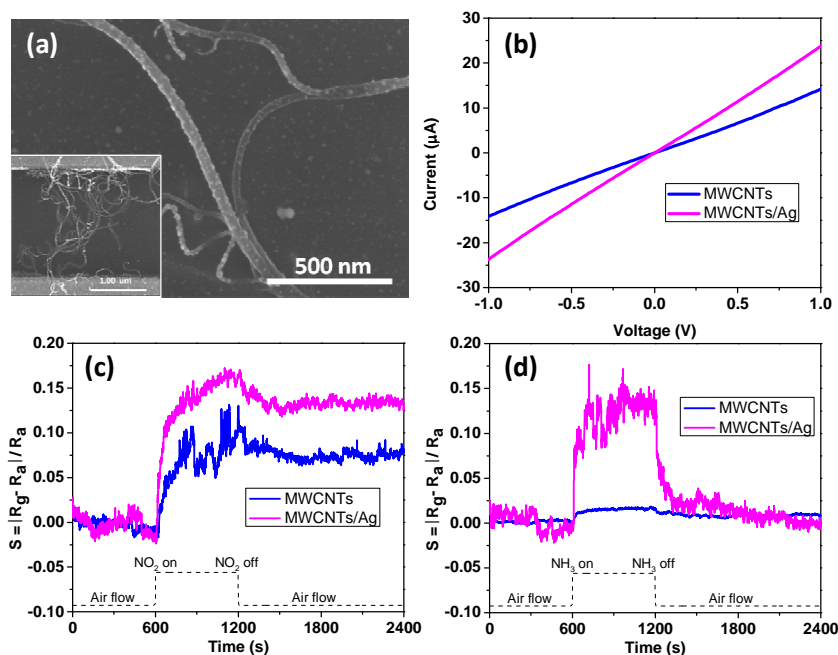


Figure 4.5 (a) SEM image of MWCNTs coated with Ag NPs. Inset is an SEM image showing the hybrid structure bridging two gold electrodes. (b) I - V characteristics of MWCNTs and MWCNTs/Ag. (c) and (d) are sensing responses of bare MWCNTs and MWCNTs/Ag structures to 100 ppm NO_2 and 1% NH_3 at room temperature, respectively.

In light of report that MWCNTs/Ag has better sensitivity than bare MWCNTs for NO_2 , [96] we also synthesized an MWCNTs/Ag hybrid sensor using our method. SEM

images of the structure are shown in Figure 4.5a. Ag NPs uniformly decorate the surface of the MWCNTs. The *I-V* characteristics in Figure 4.5b show that the resistance of MWCNTs decreases after deposition of Ag NPs because of electron transfer from MWCNTs to Ag NPs. The sensing of NO₂ was consistent with the previous report (Figure 4.5c). Furthermore, the sensing to NH₃ was also carried out, and the result showed that the sensitivity increased dramatically after deposition of Ag NPs (Figure 4.5d). Therefore, Ag NPs promote the sensing performance of bare MWCNTs toward NO₂ and NH₃.

Therefore, from experimental data, we can conclude that Ag enhances the sensing performance by “electronic sensitization.” This is true when Ag is in direct contact with MWCNTs because of direct charge transfer between them. It is also applicable to the case when Ag NPs are on top of SnO₂ NPs supported by MWCNTs. The oxidation state change of Ag with surrounding gases influences the electronic state of SnO₂, which then affects the electronic state of MWCNTs, leading to a resistance change for the hybrid nanostructure. To further prove this, a control sample was synthesized. For this sample, bare MWCNTs were tested for gases (NO₂, NH₃) first. Then SnO₂ NPs were deposited on MWCNTs such that they cover the whole surface of MWCNTs (Figure 4.6). Sensing test was carried out again. At last, Ag NPs were decorated on top of SnO₂ NPs, and the sensing test was performed. The *I-V* characteristics (Figure 4.7) were measured for each step and it shows that resistance keeps decreasing with the deposition of SnO₂ and Ag NPs, which suggests charge transfer from MWCNTs to Ag NPs after Ag deposition and a subsequent resistance change in MWCNTs. This is one of the evidences for “electronic sensitization” mechanism because there is no resistance change affected by metal

promoter in “chemical sensitization”, which is an alternative sensing mechanism.[192]

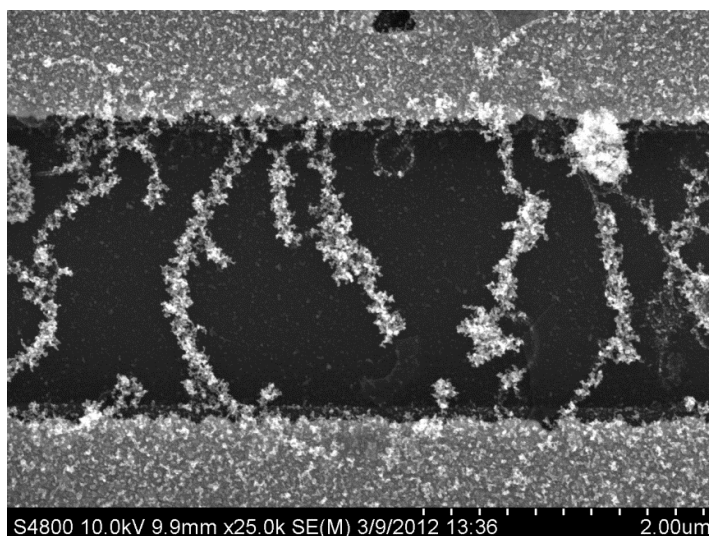


Figure 4.6 SEM image of MWCNTs with full surface coverage of SnO₂ NPs.

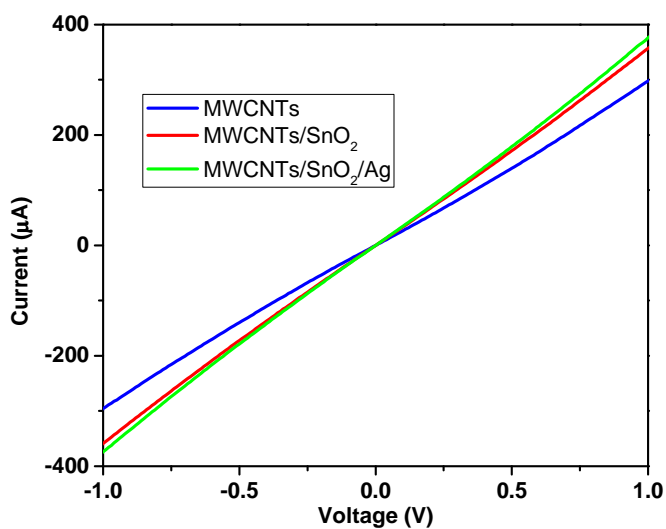


Figure 4.7 *I-V* curve evolution of the control sample, which was obtained by first coating MWCNTs with SnO₂ NPs at a high coverage followed by additional coating of Ag NPs.

The sensing responses of the control sample to 1,250 ppm NO₂ at room temperature are shown in Figure 4.8a. The sensitivity of MWCNTs increased with even full coverage

of SnO₂ NPs. It increased further after the Ag NPs deposition, indicating that charge transferred out of MWCNTs and Ag NPs indirectly changed the resistance of MWCNTs. The control sample was also tested for 1% NH₃. As shown in Figure 4.8b, after covered with SnO₂ NPs, the sensitivity decreased greatly, demonstrating that SnO₂ is insensitive to NH₃. This is consistent with our previous experimental and theoretical calculations. However, after deposition of Ag NPs, the sensitivity increased dramatically because of high sensitivity of Ag to NH₃.

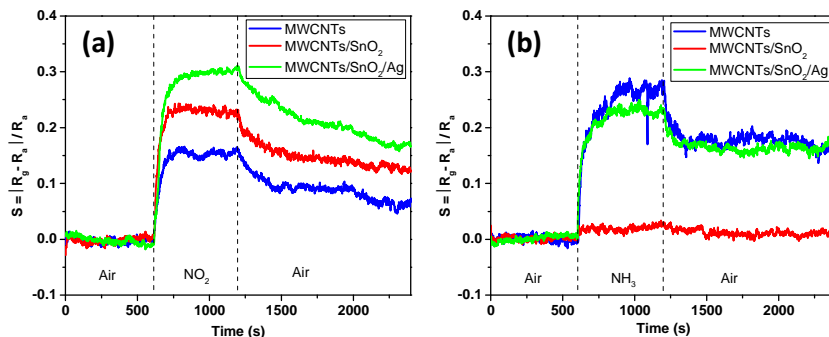


Figure 4.8 Sensing responses of a control sample at room temperature to (a) 1,250 ppm NO₂ and (b) 1% NH₃. For the control sample, MWCNTs were first coated with SnO₂ NPs at a high coverage and then coated with Ag NPs.

4.3 Summary and conclusions

In conclusion, Ag NPs can be used as a room-temperature sensing promoter on MWCNTs. Compared with MWCNTs alone and MWCNTs/SnO₂ hybrid structures, the as-produced ternary MWCNTs/SnO₂/Ag hybrid sensor exhibited higher sensitivity and faster response towards both NO₂ and NH₃ at room temperature. The sensing mechanism of Ag supported by MWCNTs can be explained as “electronic sensitization.” The oxygen

atoms on Ag surface play a critical role in the gas sensing. Meanwhile, NO_2 combines with surface oxygen atoms to form an NO_3 ion complex on the SnO_2 nanocrystal surfaces, but SnO_2 nanocrystals are insensitive to NH_3 at room temperature. Therefore, MWCNTs/Ag is the best hybrid sensor for NH_3 sensing alone. These findings not only cast insights into the mechanism of the Ag-promoted CNT sensors toward NO_2 and NH_3 , but also provide guidance to engineer sensitivity and selectivity of semiconductor sensors for practical applications.

CHAPTER 5 SILVER NANOPARTICLES-DECORATED REDUCED GRAPHENE OXIDE (RGO) FOR GAS SENSORS

5.1 Experimental methods

5.1.1 Preparation of RGO

The RGO was obtained by chemically reducing GO dispersion, which was prepared using a modified Hummers method.[197] Briefly, $\text{H}_3\text{NO}\cdot\text{HCl}$ was added into the GO dispersion and the mixture was continuously stirred at 80 °C for 30 h. Then, the black product was filtered and washed with distilled water and acetone to obtain RGO powders. Finally, the RGO dispersion was prepared by distributing the RGO powders in *N,N*-Dimethylformamide (DMF) with sonication for 2 h.

5.1.2 Sensor fabrication and characterization

Figure 5.1 illustrates the complete sensor fabrication process. Interdigitated gold electrodes were fabricated using e-beam lithography on a silicon substrate with a SiO_2 thin top layer. Then, a tiny drop (1 μl) of RGO dispersion was drop cast on the gold electrodes, and RGO flakes bridged the gold fingers after solvent evaporation. The amount of RGO flakes on gold electrodes can be controlled by adjusting the dispersion concentration. Further annealing treatment at 200 °C for 1 h in Ar flow (1 lpm) was performed to remove the residual DMF and improve the contacts between the RGO and gold electrodes.

To synthesize the RGO/Ag hybrid, we produced Ag NPs using a previously-reported physical vapor deposition process in a mini-arc plasma reactor.[184, 186] The mini-arc plasma was generated between two carbon electrodes driven by a commercial tungsten inert gas (TIG) arc welder (Miller Maxstar 150 STH), and small pieces of Ag (99.999% purity) cut from an Ag wire were used as the source material. The Ag pieces were first vaporized by the mini-arc plasma source. Then, the Ag vapor was carried by an Ar flow downstream and quenched in the gas phase, forming Ag NPs. The as-produced Ag NPs were directly deposited onto the RGO supported by gold electrodes or a TEM grid using an ESFDA process.[198]

The as-produced RGO was characterized in our previous report.[197] The morphology and crystal structure of the RGO/Ag hybrid were studied using a field-emission SEM (Hitachi S4800) and an HRTEM (Hitachi H-9000-NAR) with 0.18 nm point and 0.11 nm lattice resolution operated at an accelerating voltage of 300 kV. The surface chemical composition was characterized by an X-ray photoelectron spectroscope (XPS) (HP 5950A). Raman spectra were taken using a Raman spectrometer (Renishaw 1000B).

5.1.3 Ammonia-sensing measurement

The sensor device was placed in an air-tight chamber with electrical feedthroughs. A constant voltage was added to the electrodes, and the variation of resistance was monitored and recorded with the changes in the gas environment using a Keithley 2602

source meter. Typically, a sensing-measurement cycle has three continuous steps: (1) introducing dry air (2 lpm) as a background, then (2) injecting ammonia gas (2 lpm) to register a sensing signal, and (3) introducing dry air (2 lpm) again for sensor recovery.

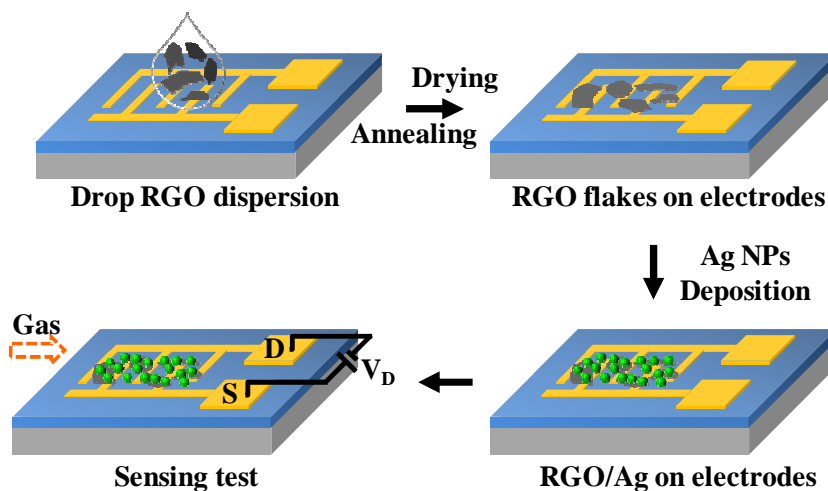


Figure 5.1 Schematic illustration of the process to fabricate RGO/Ag hybrid sensor devices and the subsequent sensing measurements.

5.2 Results and discussion

After the RGO dispersion dried on the gold electrode, the morphology was characterized by SEM. Figure 5.2a shows an SEM image of one typical RGO flake bridging a pair of gold electrode fingers in a sensor device; the wrinkle on the RGO flake is an intrinsic characteristic.[199] After *in situ* deposition of Ag NPs on RGO, RGO/Ag hybrids formed on the device (Figure 5.2b); it is evident that Ag NPs distribute uniformly on the RGO surface. Since the number of Ag NPs can be controlled by deposition time, the loading density shown in Figure 5.2b is relatively high for a deposition time of 15 min. The RGO/Ag hybrids were also characterized by TEM with a sample prepared on a TEM grid.

Figure 5.2c shows a TEM image of RGO/Ag hybrids suspending over the carbon film hole. The size of the Ag NPs ranges from several nanometer to 10 nm over the RGO surface. Some larger NPs of about 20 nm anchor on the edge due to the stronger electrostatic force during the ESFDA process.[198] The inset in Figure 5.2c is an SAED pattern of RGO/Ag hybrids, evidencing a single layer of RGO and good crystallinity of Ag NPs, in which the first four bright continuous rings are indexed to cubic fcc (111), (200), (220), and (311) lattice planes of Ag metal from the inside to the outside.[184] An HRTEM image (Figure 5.2d) further confirms the crystalline structure of Ag NPs, and the measured lattice spacing of 0.235 nm is indexed to (111) plane of Ag.

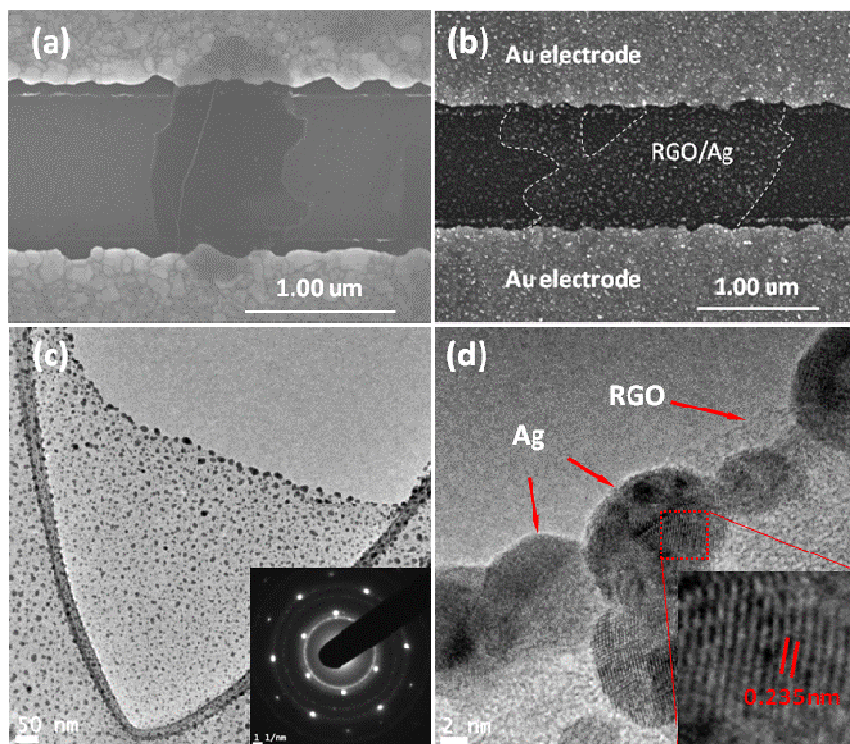


Figure 5.2 (a, b) SEM images of an RGO flake before and after Ag NP deposition bridging a pair of gold electrode fingers. (c) TEM image of an RGO flake decorated with Ag NPs. The inset is an SAED pattern of RGO/Ag hybrids. (d) HRTEM image of RGO/Ag hybrids.

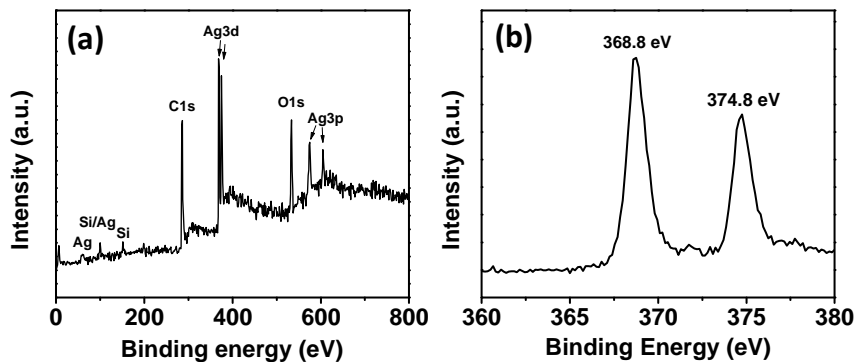


Figure 5.3 (a) XPS spectra of RGO/Ag hybrids. (b) High-resolution XPS spectra of Ag 3d from RGO/Ag hybrids.

The surface composition of the RGO/Ag hybrid nanostructure was examined using XPS (Figure 5.3). The entire XPS survey spectra (Figure 5.3a) clearly show C 1s, O 1s, Ag 3d, and Ag 3p peaks, indicating the hybrids consist of C, O, and Ag elements. The Si peak in the spectra is from the silicon wafer, which was used as the support in the test. According to our previous study, RGO mainly contributes to the C 1s and O 1s signals detected due to the graphene basal plane and the oxygen-containing functional groups.[197] A part of the O signal could be from the oxygen adsorption in air. It was reported that Ag 3d peaks of Ag NPs were composed of Ag metal and Ag⁺ appeared at 368.3 and 374.3 eV.[200] In our study, the Ag 3d peaks are centered at 368.8 and 374.8 eV (Figure 5.3b), which are close to the reported results, indicating metallic Ag and Ag⁺ on the RGO surface. This is also consistent with our theoretical calculation results that the surface of Ag NPs is likely oxidized by oxygen when exposed to air.[186] The RGO/Ag hybrids were also characterized using Raman spectroscopy. Figure 5.4 shows the Raman spectra of RGO before and after the Ag NP decoration. The spectrum of RGO, with a D band to G band intensity ratio of 1.26, is consistent with that of chemically reduced graphene oxide.[114] The similar spectra of RGO with and without the Ag NP decoration

indicate that Ag NPs do not significantly modify the structure of RGO.

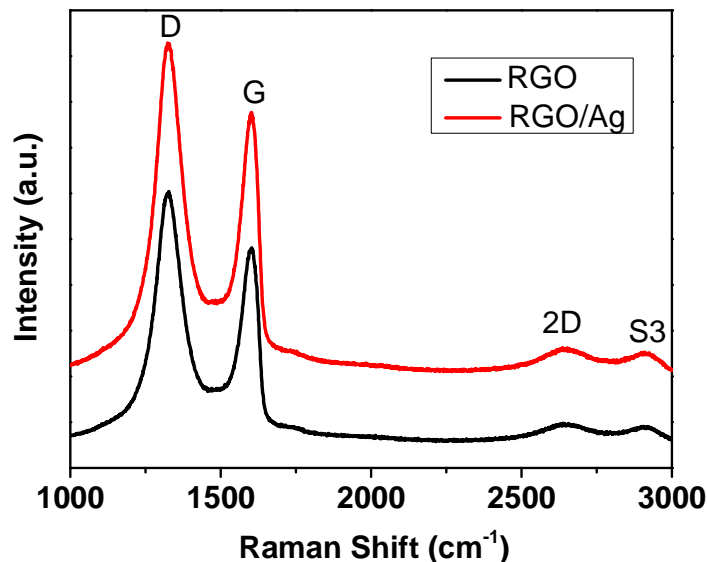


Figure 5.4 Raman spectra of RGO and RGO/Ag hybrids.

Figure 5.5a shows the electrical characteristics of a field-effect transistor (FET) device based on RGO/Ag hybrids. The straight linear I - V curve indicates that the contacts between the RGO/Ag and gold electrodes are Ohmic. To investigate the effect of Ag NPs on RGO, the resistance of the device was measured before and after the deposition of Ag NPs. We found the resistance of this sample increased from 1.3×10^3 to $1.4 \times 10^3 \Omega$, which is the typical trend for all samples. Because the RGO in this study is a p-type semiconductor (Figure 5.6), the increased resistance could be explained by the fact that Ag NPs led to hole depletion zones at their interface between the RGO and Ag NPs, which is consistent with our previous results of depositing SnO_2 NPs on RGO sheets.[201] However, the resistance of MWCNTs decreased when Ag NPs were deposited on them (MWCNTs are p-type semiconductors, same as RGO), possibly because of the oxygen-containing functional groups on RGO. The inset in Figure 5.5a

shows the source-drain current curve of gate voltage dependence for the FET device, which demonstrates that the current decreases slowly with gate voltage sweeping from -30 to 30 V, indicating that the RGO/Ag hybrids are p-type semiconductors and Ag NPs did not change the semiconducting type of RGO.

To demonstrate the sensing enhancement of Ag NPs, the sensing performance of RGO was measured before and after Ag NP deposition, respectively. To ensure comparable results, bare RGO was first tested against NH_3 . Then, the same sensor was tested again after depositing Ag NPs using the same sensing process. The dynamic sensing responses of both bare RGO and RGO/Ag hybrids to 1% NH_3 are shown in Figure 5.5b. The sensitivity is defined as the ratio of resistance change with exposure to the test gas to the initial resistance in air ($\Delta R/R$). The results demonstrate that the sensitivity increased from $5.1 \pm 0.2\%$ for RGO to $17.4 \pm 0.2\%$ for RGO/Ag hybrids with the same exposure time, which clearly indicates the significant sensing enhancement of Ag NPs. This enhancement also can be presented in terms of signal-to-noise ratio (S/N) of RGO and RGO/Ag hybrids. Here, S is defined as the ratio of maximum sensitivity upon NH_3 exposure to the average sensitivity in air before NH_3 exposure. N is defined as the ratio of maximum sensitivity in air to the average sensitivity in air in the first sensing cycle. According to the analysis, the S/N values are 7.6 and 13.6 for RGO and RGO/Ag hybrids, respectively, which suggests that RGO/Ag hybrids are better than RGO for NH_3 detection.

According to our previous study, Ag NPs act as the dominant active adsorption sites for NH_3 and enhance the sensitivity of p-type MWCNTs by “electronic

sensitization.”[184] NH_3 is a typical reducing gas, acting as an electron donor upon interaction with sensors. A net charge transfer from NH_3 to Ag was observed upon adsorption that reduced the oxidation state of Ag,[184] increased the hole depletion zones in RGO, and increased RGO sensitivity. Ag NP deposition on RGO resulted in more active adsorption sites and stronger adsorption ability for NH_3 , which may be responsible for the significant sensing enhancement.

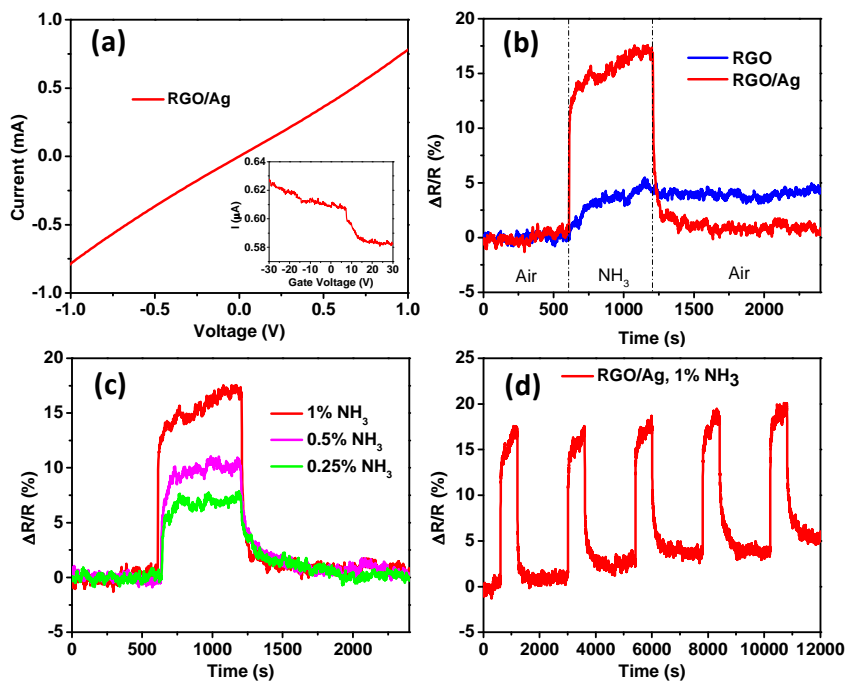


Figure 5.5 (a) I - V characteristic of RGO/Ag hybrids on gold electrodes and the inset is the FET measurement of the sensor device. (b) The room-temperature dynamic-sensing responses of RGO before and after Ag NP deposition. (c) Dynamic responses of RGO/Ag hybrids when exposed to different concentrations of NH_3 . (d) Five-cycle responses of RGO/Ag to 1% NH_3 , indicating a good stability of the sensor.

The sensitivity of RGO/Ag hybrids is also about twice that of hybrids composed of MWCNTs and Ag NPs (9%) with the same deposition time.[184] The sensor's high sensitivity can be attributed to the large specific surface area of RGO, which offers more

surfaces for Ag NP dispersion and leads to more active sites for NH₃ adsorption. The results are consistent with a previous report that demonstrated Pt-decorated graphene sensors are more sensitive than Pt-decorated MWCNTs to H₂. [202] Other properties of RGO may also play an important role in the enhancement, such as high carrier mobility (15,000 cm²V⁻¹s⁻¹). [98]

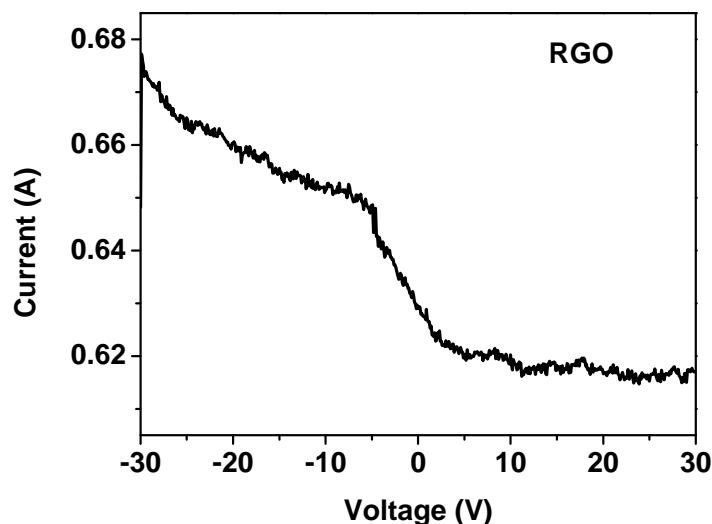


Figure 5.6 FET measurement of pure RGO.

To compare the response time of RGO before and after Ag NP deposition, a response time was defined as the time needed for a sensor to change more than 63.2% of the maximum sensitivity, corresponding with a one-time constant in a first-order dynamic system. [163] Analysis of Figure 5.5b shows the response times are 151 s and 6 s for RGO and RGO/Ag hybrids, respectively. The response time for RGO/Ag hybrids is comparable with that of Ag NP-decorated MWCNTs (7 s) [184] and other fast NH₃ sensors, such as an ultrafast room-temperature NH₃ sensor made of RGO (10 s). [203] The dramatically improved response by Ag NPs can be understood using a similar mechanism with Ag NPs

on MWCNTs.[184] RGO has much higher charge carrier mobility and acts as a conducting channel in the sensor device. The electronic state of RGO can be rapidly changed by the oxidation state of Ag NPs. Both the adsorption of NH_3 on Ag NPs and the electron transfer between NH_3 and Ag are fast, as shown in our previous study.[184] Thus, the adsorption of NH_3 can rapidly change the charge carrier density of RGO and lead to a faster response.

The recovery time of RGO was also improved by Ag NPs. Here, the recovery time was defined as the time needed to recover more than 63.2% of the maximum sensitivity. An analysis of Figure 5.5b demonstrates that an RGO/Ag sensor can fully recover to its initial state within 6.7 min, which is comparable with that of Ag NP-decorated MWCNTs hybrids (7 min).[184] However, it took the RGO overnight or days to obtain full recovery, which is consistent with previous reports.[177, 178] For our RGO/Ag sensor, the recovery time is 10 s, which is also comparable with that of an Ag NP-decorated MWCNTs ammonia sensor (15 s).[184] Therefore, the recovery speed was greatly accelerated by coating with Ag NPs. The long recovery time for the RGO could be attributed to high binding energy between NH_3 molecules and RGO defects and oxygen-containing functional groups. Nevertheless, Ag NPs occupied those active sites and the direct interaction between NH_3 and Ag NPs dominated the sensing process. The rapid recovery speed indicates the desorption barrier from the Ag surface for NH_3 molecules is low and the electron transfer from Ag to NH_3 occurs quickly, which agrees with our previous study.[184] For practical use, a sensor should have distinguishable sensitivities to different gas concentrations. In this study, different concentrations of NH_3

were measured using the same sensor device, and the results suggest the sensor was sensitive to concentration variations; the sensitivity increased from $7.7\pm 0.2\%$ to $17.4\pm 0.2\%$ with increasing gas concentrations ranging from 0.25 to 1% (Figure 5.5c). To study the sensing stability, five sensing cycles were measured to 1% NH_3 using the same sensing process (Figure 5.5d). The sensing responses appear to be quite repeatable.

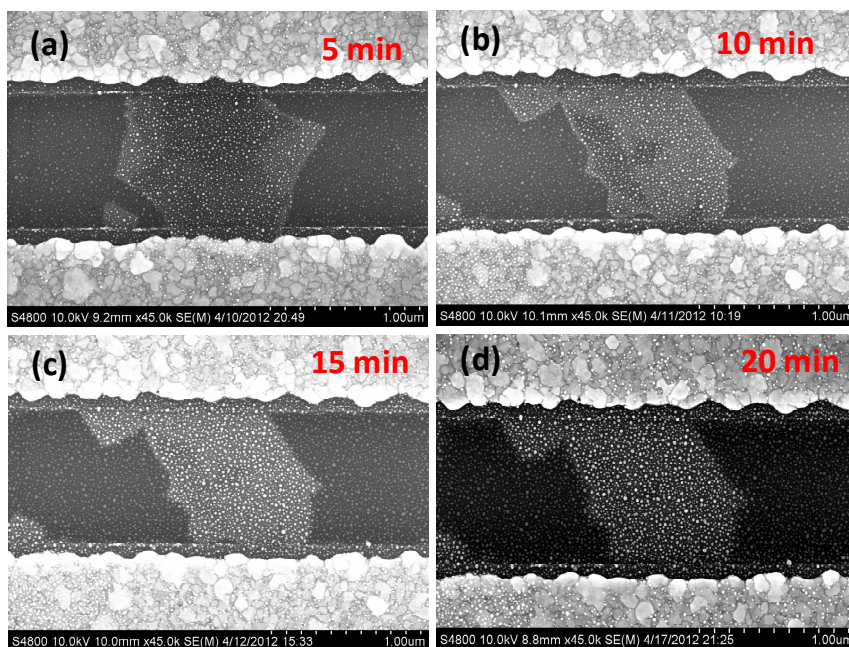


Figure 5.7 SEM images of RGO coated with different loadings of Ag NPs.

According to the results, Ag NPs on the RGO surface serve as the dominating sensing element; therefore, the NP density can significantly affect the sensing performance. To investigate the influence, the sensing response was measured for one sensor device with four Ag NP loadings of 5 min, 10 min, 15 min, and 20 min deposition time, respectively. First, the sensing performance was tested with Ag NPs with 5 min deposition time. Then, the same sensor was measured again with another 5 min Ag NP deposition, and this process continued until coating for 20 min deposition time. Figure 5.7

shows SEM images of the sensor with different Ag NP loadings. The areal density of Ag NPs increases with increasing deposition time, and the Ag NPs distributed uniformly over the entire surface of the RGO, even with a large number of NPs, which is superior to the wet-chemical method that typically causes Ag NP aggregation with a overly high loading.[200] The sensing responses indicate that the sensitivity of RGO was dependent on Ag NP density (Figure 5.8). The RGO loaded with Ag NPs with 15 min deposition time provided the highest sensitivity due to more adsorption sites, whereas longer deposition time (20 min) dramatically decreased the sensitivity, which is consistent with that of Pt-coated RGO.[140] A possible reason for this is related to the high density of Ag

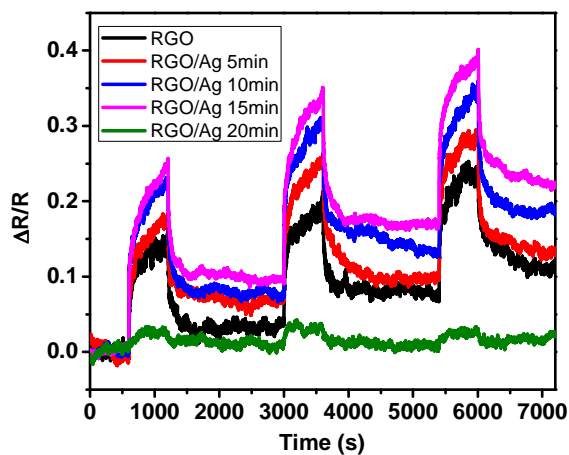


Figure 5.8 Dynamic sensing evolution of RGO/Ag NP hybrids with different Ag NP loadings on the RGO.

NPs on the RGO surface, in which a continuous Ag film formed on the RGO. To further confirm this, a bare gold electrode without RGO was deposited with Ag NPs for 1 h and the morphology was observed using SEM (Figure 5.9). The electrical test showed the electrode gap was still open, suggesting a non-continuous Ag NP film. Until now, it is

unclear why the sensitivity dramatically decreased, and more work is needed to obtain a clear understanding. Nevertheless, a proper loading of Ag NPs with about 15-min deposition time could provide a maximum sensitivity.

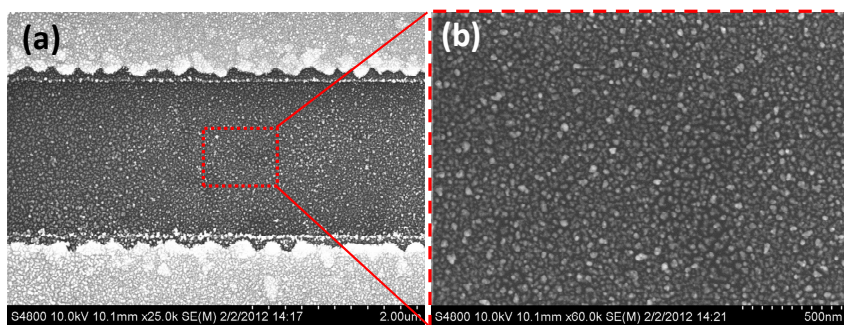


Figure 5.9 SEM images of Ag NPs on a gold electrode with deposition time of 1h. Electrical test showed the circuit was still open.

The response of the RGO sensors before and after Ag NP deposition was also evaluated against NO_2 , because of its strong cross-sensitivity for RGO.[197, 119] Figure 5.10a clearly demonstrates that the resistance change of RGO during exposure to NO_2 decreased due to coating Ag NPs and led to a highly selective ammonia sensor. Interestingly, the sensitivity (real value in Figure 5.10a) kept decreasing for the RGO sensor when exposed to NO_2 ; however, the sensitivity of the RGO/Ag hybrids rapidly decreased for a short time, and then gradually increased in NO_2 flow. For recovery in air, the RGO recovered only a part of the entire resistance change in 20 min, but RGO/Ag hybrids recovered and exceed the resistance change for NO_2 exposure in 5 min. The following five-cycle response to NO_2 was stable and can recover to its initial state in a short time (Figure 5.10b), and the sensitivity is similar with the first cycle. In this study, to the best of our knowledge, this interesting over-recovery of RGO-based gas sensors is

reported here for the first time. To further verify this behavior, another RGO/Ag sample was prepared and tested using the same process. The sensing response to NO_2 is similar to that in Figure 5.10a, but the sensitivity greatly increased for the rising part when exposed to NO_2 , demonstrating an even higher over-recovery (Figure 5.10c). This behavior remained the same in the next several cycles, as shown in Figure 5.10d. To demonstrate the sensing behavior to NH_3 , the same sensor was measured with 1% NH_3 for five cycles (Figure 5.11); the results indicate good sensing, similar to that in Figure 5.5d.

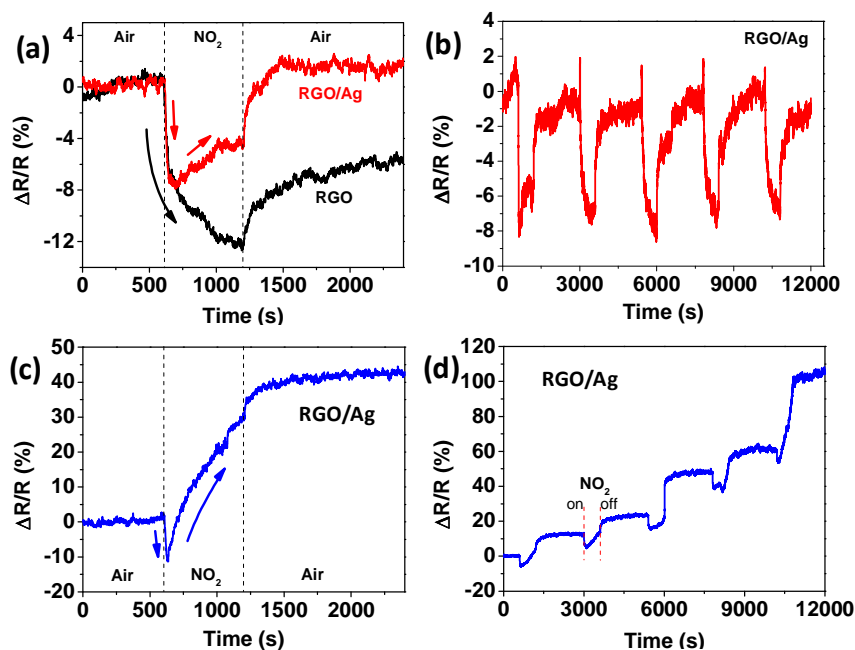


Figure 5.10 Dynamic sensing responses of RGO to NO_2 before and after Ag NP deposition. (b) Five-cycle sensing behavior of RGO/Ag hybrids followed by the first cycle in (a). (c, d) First cycle and the subsequent five-cycle sensing response, respectively, for another RGO/Ag sample with the same Ag NP loading (15 min deposition).

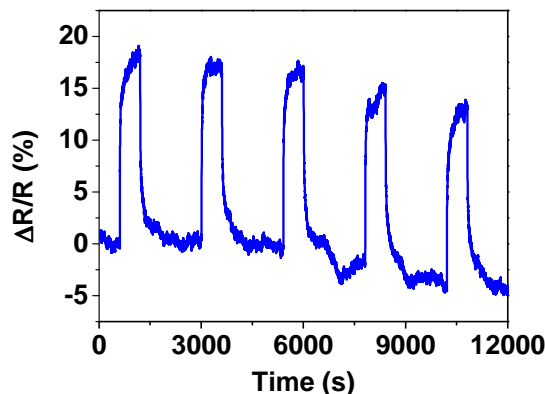


Figure 5.11 Dynamic sensing response to 1% NH_3 for another RGO/Ag hybrid sensor.

Generally, NO_2 is an oxidizing gas and withdraws electrons upon adsorption in the gas-sensing process. Ag NPs were found to improve the response of MWCNTs to NO_2 . [186] It is reasonable that the resistance of the RGO/Ag hybrids decreased at the beginning, as indicated in Figure 5.10a and 5.10c, due to its p-type semiconducting property and an electron transfer from the hybrids to NO_2 . However, the resistance increased in the following major time for NO_2 exposure, suggesting that electrons transferred into the RGO/Ag hybrids. The large increase in resistance shown in Figure 5.10c indicates an even larger number of electrons transferring from the gas to the hybrids, and NO_2 acted like an electron donor. This could be related to the intrinsic property change of RGO by decorating NPs. A similar interesting sensing-response behavior also occurred to SnO_2 NP-decorated RGO hybrids for H_2 detection. Hydrogen is a reducing gas and donates electrons into sensors upon adsorption on SnO_2 -decorated p-type semiconducting MWCNTs. [204] However, the resistance of SnO_2 NP-decorated RGO hybrids decreased after exposure to H_2 , suggesting that electrons transferred out of the RGO, which is the conducting channel for the sensors. [205] Because of the possible

property change, the real resistance of RGO/Ag hybrids decreased less than pure RGO with the same NO_2 exposure due to fewer electrons transferring out of the RGO/Ag hybrids. Further study is warranted to obtain a clear understanding of such a phenomenon.

5.3 Summary and conclusions

We fabricated new ammonia sensors using Ag NP-decorated RGO hybrid nanostructures in a simple and controllable fashion. Ag NPs are uniformly distributed on RGO surface. The RGO/Ag hybrid sensors show higher sensitivity than RGO alone due to the enhancement of Ag NPs. Compared with MWCNTs/Ag hybrid sensors, RGO/Ag hybrids exhibit about twice the sensitivity with a similar Ag NP loading density, which is likely due to the high specific surface area of RGO. Because of the low binding energy between NH_3 and Ag, Ag NP decoration on RGO also achieves fast response (6 s) and recovery speed (10 s) to NH_3 which are much faster than pure RGO. The density of Ag NPs affects the sensitivity, and there is a maximum sensitivity for a proper loading density. Ag NPs also decrease the response (reduced resistance) to NO_2 , resulting in a better selectivity of RGO to NH_3 . In the hybrids, Ag NPs act as the dominant sensing sites and a net electron transfer from NH_3 to Ag reduced the carrier concentration in RGO, leading to an increase in resistance.

CHAPTER 6 DOPED SnO₂ NANOPARTICLES– FUNCTIONALIZED REDUCED GRAPHENE OXIDE FOR GAS SENSORS

6.1 Experimental methods

6.1.1 Synthesis of hybrids

GO was prepared by oxidizing graphite powder (Bay Carbon, SP-1 graphite) under acidic conditions according to the modified Hummers method.[197] In a typical process to prepare In-doped SnO₂ NPs decorated RGO (RGO-IDTO), 8 mg GO was dispersed in 20 ml deionized water, and sonicated for 30 min. Then 0.5 ml InCl₃ (0.05 M) aqueous solution and 2.5 ml SnCl₄ (0.01 M) were added to the GO dispersion in sequence with magnetic stirring (400 rpm). The mixture was sonicated for 10 min to allow for uniform ion adsorption on the GO surface. After that, 15 ml NaBH₄ aqueous solution (30 mg/10 ml) was added drop-wise into the above solution with stirring. Finally, the entire solution was kept at 50 °C on a hotplate for 1 h. The final product was collected by centrifugation. Ru-doped SnO₂ NPs decorated RGO (RGO-RDTO) were also prepared using the same method; 1 ml RuCl₃ (0.05 M) was used as the dopant source, and all the other chemicals and procedures were the same as those used for the RGO-IDTO synthesis.

6.1.2 Characterization

The samples were characterized using a number of techniques. The crystallographic

structure of as-produced nanohybrids was investigated by X-ray diffraction (XRD). Scanning electron microscope (SEM) was carried out with a Hitachi S-4800 electron microscope at an acceleration voltage of 10 kV. The structure of as-produced nanohybrids was characterized by transmission electron microscopy (TEM) (Hitachi H-9000-NAR). High-resolution TEM (HRTEM) and selected area electron diffraction (SAED) (at an acceleration voltage of 300 kV) were used to characterize the crystal structure of the nanohybrids. Energy-dispersive X-ray spectroscopy (EDS Noran Si:Li detector) was used to characterize the elemental composition. The surface chemical composition was characterized by using X-ray photoelectron spectroscopy (XPS) (HP 5950A). Raman spectra were taken using a Raman spectrometer (Renishaw 1000B).

6.1.3 Gas sensor fabrication and sensing test

To prepare gas sensors composed of RGO-IDTO nanohybrids, gold interdigitated electrodes with finger width and inter-finger spacing of 2 μm and thickness of 50 nm were fabricated by an e-beam lithography process on a silicon wafer with a top SiO_2 layer of about 200 nm. The RGO-IDTO nanohybrids were dispersed in *N,N*-Dimethylformamide (DMF), and then a drop (0.1 μl) of the dispersion was cast onto the gold electrode. Low concentration dispersion was used to avoid overlapping RGO sheets. To purify the sensor and improve the electrical contact between the nanohybrids and the gold electrodes, the sensor devices were annealed in a tube furnace at 200 $^\circ\text{C}$ for 1 h before sensing tests.

The gas sensing properties were tested in an air-tight chamber with electrical feedthroughs. A constant voltage was applied to the electrode gap bridged by the nanohybrids. Then the target gas with certified concentrations was flowed into the chamber, and the change in the current passing through the nanohybrids was monitored and recorded using a Keithley 2602 source meter (Keithley, Cleveland, OH). A typical sensing test cycle consisted of three sequential steps. First, a dry air flow was introduced into the sensing test chamber to record a baseline. Then, a target gas diluted in air was injected to register sensor signals. Finally, the sensor was recovered in a dry air flow. All the flow rates were controlled at 2 lpm, and the target gases were diluted in dry air. The sensor sensitivity was defined as $S = \Delta G/G_0$, where ΔG is the change in the sensor conductance before and after the gas exposure and G_0 is the sensor conductance in dry air. The resistance of RGO-IDTO nanohybrids was ~ 2 k Ω (or $G_0 = 0.0005$ S) in dry air before target gas exposure.

6.2 Results and discussion

Figure 6.1 illustrates the preparation procedure of RGO-IDTO nanohybrids. First, indium ions were introduced into the GO dispersion by adding an InCl_3 aqueous solution under magnetic stirring. Then, tin ions were slowly added into the above mixture using SnCl_4 aqueous solution as the source. After sonication, a NaBH_4 solution was slowly dropped into the solution mixture to reduce GO. The obtained solution was then continuously stirred at 50 °C for 1 h and RGO-IDTO nanohybrids were obtained after centrifuging and

washing.

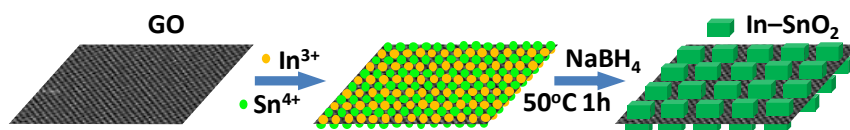


Figure 6.1 Schematic illustration for the preparation process of RGO-IDTO nanohybrids.

The morphology of as-produced RGO-IDTO nanohybrids was first examined by a field-emission SEM. An overview of the RGO-IDTO nanohybrids is shown in Figure 6.2a and b, which clearly indicates that the nanohybrids retain the sheet structure typical for graphene. The nanostructure was further investigated using TEM (Figure 6.2c), showing that the IDTO nanostructures are uniformly coated on the RGO sheet. A typical magnified TEM image is shown in Figure 6.2d, demonstrating that a thin lacy network of IDTO NPs is uniformly distributed on the surface of graphene. The inset of Figure 6.2d is an SAED pattern of RGO-IDTO with well-defined rings composed of two parts. The rings marked with red arcs (from the inside to outside) are indexed to rutile SnO₂ (110), (101), (200), (211), and (112) planes. Meanwhile, the rings marked with green arcs (from the inside to outside) are indexed to {100}- and {110}- type reflections of graphene, consistent with graphene and with the known structure of RGO with disordered oxygen functional groups. The IDTO nanocrystals anchored on the RGO sheets were further analyzed using HRTEM. As shown in Figure 6.2e, IDTO nanocrystals with clear lattice fringes are observed with sizes of about 2–3 nm. The labeled lattice spacing of 0.335 nm corresponds with the unique (110) plane of rutile SnO₂. To examine the elemental composition of NPs, EDS was performed and the result indicates that there is indium in

the nanohybrid. Similar results were obtained for RGO–RDTO nanohybrids, as shown in Figure 6.3. For substitutional doping, the difference in ionic radii should be less than the Hume–Rothery limit (15%).^[206] The ionic sizes of Sn^{4+} , In^{3+} , and Ru^{4+} are 0.083 nm, 0.081 nm, and 0.076 nm, respectively,^[207, 208] with a maximum difference of 8.4%, which lies within the Hume–Rothery limit. Thus, when In and Ru are doped in SnO_2 , In^{3+} and Ru^{4+} can substitute for Sn^{4+} , forming an uniformly stable solid solution, consistent with previous reports.^[208, 209]

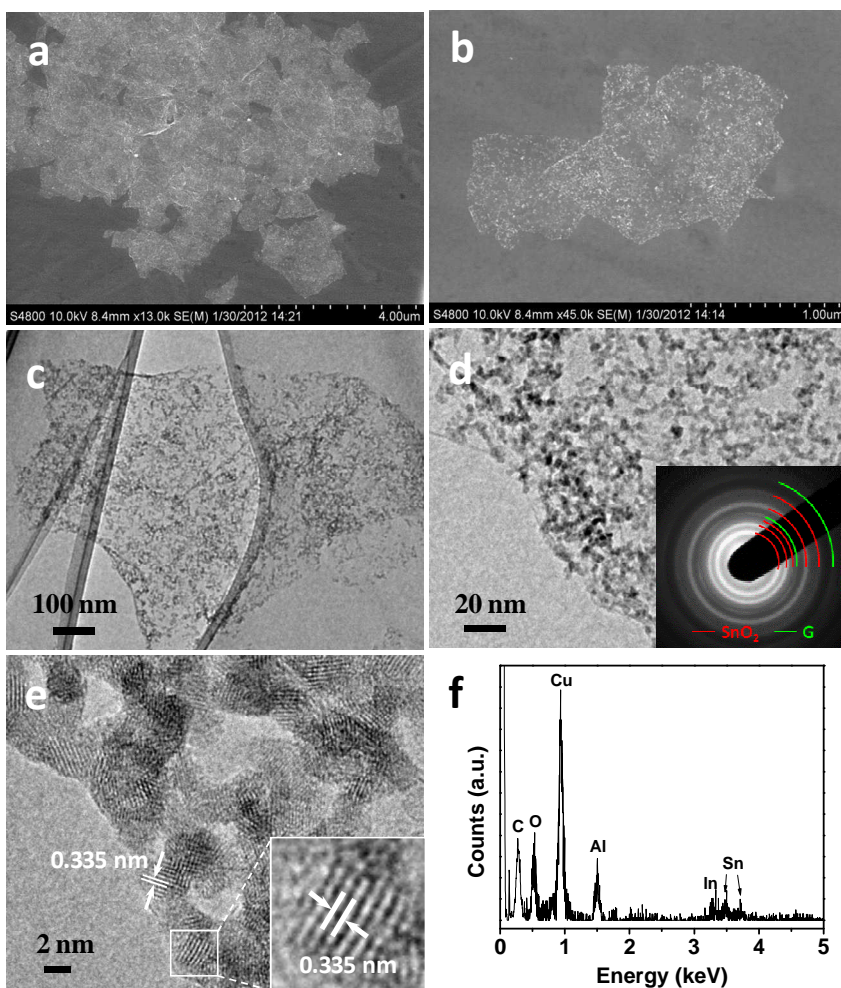


Figure 6.2 (a, b) SEM images of RGO–IDTO. (c, d) TEM images of RGO–IDTO nanohybrids. The inset in image (d) is the SAED pattern of RGO–IDTO. The rings marked with red arcs are

indexed to rutile SnO_2 , and the rings marked with green arc are indexed to graphene. (e) HRTEM image of RGO-IDTO nanohybrids. (f) EDS spectra of RGO-IDTO. Cu and Al are from the sample holder.

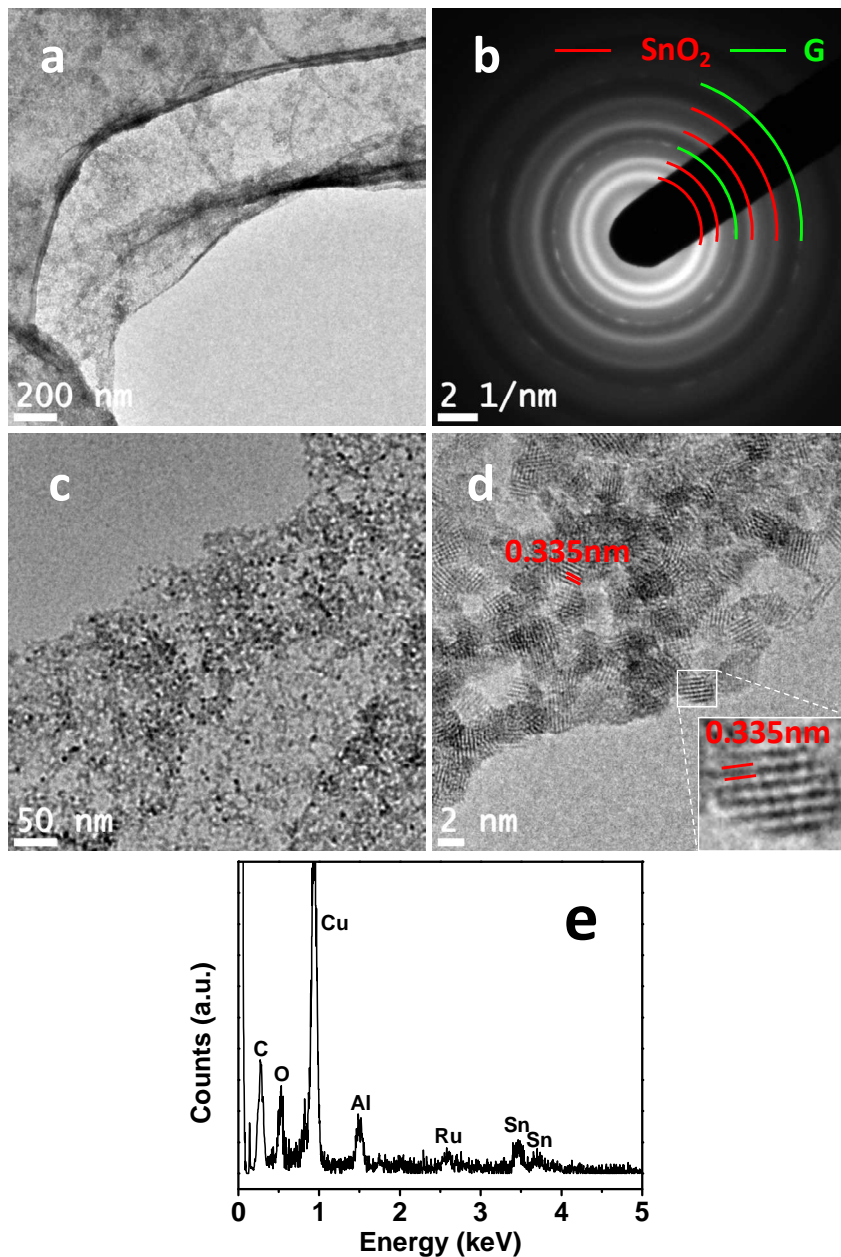


Figure 6.3 (a, c) low magnification TEM images of RGO-RDITO nanohybrids. (b) SAED pattern indexed to rutile SnO_2 and G. (d) HRTEM image of RGO-RDITO nanohybrids. (e) EDS spectrum of RGO-RDITO nanohybrids.

To obtain information about the average crystallographic structure, the RGO-IDTO

nanohybrid was characterized using XRD (Figure 6.4a). For comparison, RGO-SnO₂ without dopants was synthesized using a two-step method published previously.[210] Briefly, Sn⁴⁺ was introduced into the GO dispersion and adsorbed on the surface of GO bonded with oxygen functional groups (e.g., hydroxyl and carbonyl groups) by electrostatic force. Then the precipitate was collected and washed with centrifugation. The product was dried at 80 °C overnight, and RGO-SnO₂ was obtained after annealing treatment at 350 °C for 2 h under argon atmosphere. The XRD pattern in Figure 6.4a demonstrates the presence of crystalline IDTO NPs through the diffraction peaks corresponding with the (110), (101), (200), and (211) planes of rutile SnO₂ (JCPDS 041-1445). The broad peaks indicate that the nanocrystals are tiny, consistent with TEM results. There are no other peaks except for one weak peak around 25.5° corresponding to the (002) plane of few-layer RGO, suggesting that pure IDTO NPs are anchored on the surface of RGO during the synthesis. The XRD pattern of RGO-IDTO is very similar to that of RGO-SnO₂, suggesting that there were no phase changes occurring and no nanoscale separation with indium doping in SnO₂, which is consistent with the previous report.[211] The above results suggest that the dopant ions are homogeneously distributed in the SnO₂ lattice. The XRD pattern of RGO-RDITO shows similar characteristics (Figure 6.5).

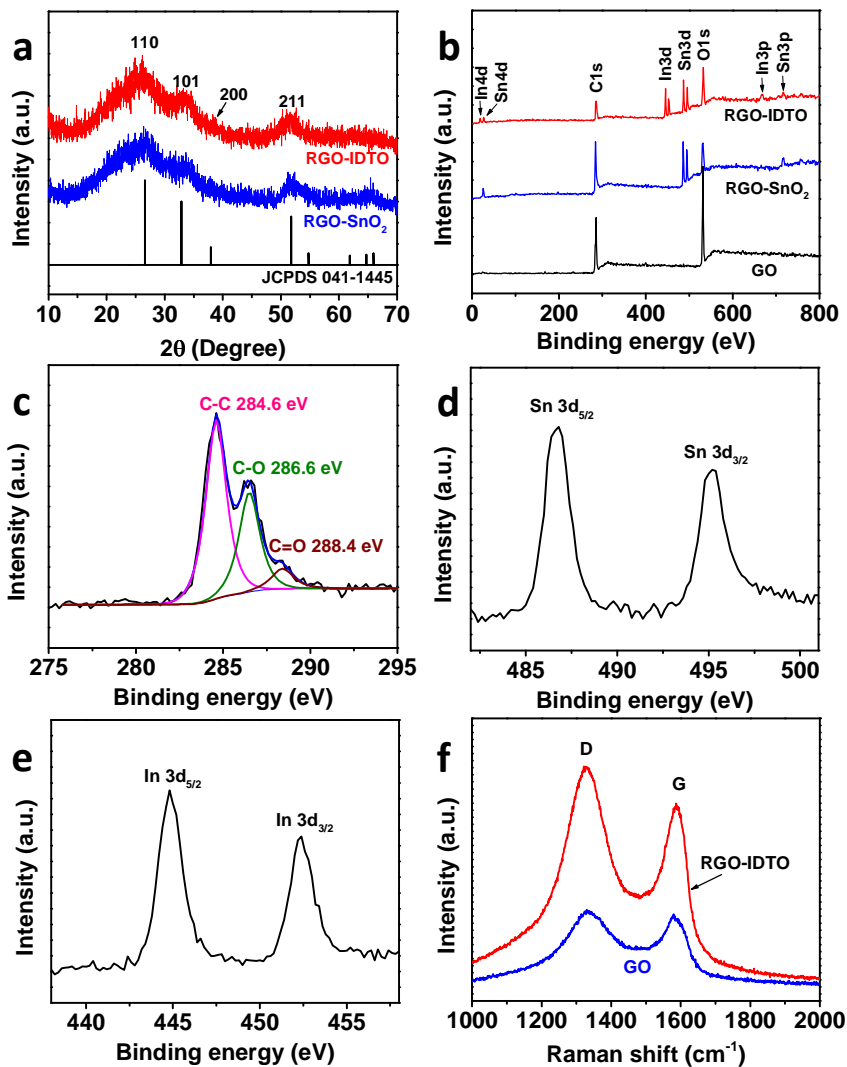


Figure 6.4 (a) XRD patterns of RGO-SnO₂ and RGO-IDTO nanohybrids. (b) XPS spectra of GO, RGO-SnO₂, and RGO-IDTO nanohybrids. (c-e) High-resolution XPS spectra of C 1s (c), Sn 3d (d), and In 3d (e) of the RGO-IDTO nanohybrids. (f) Raman spectra of GO and RGO-IDTO nanohybrids.

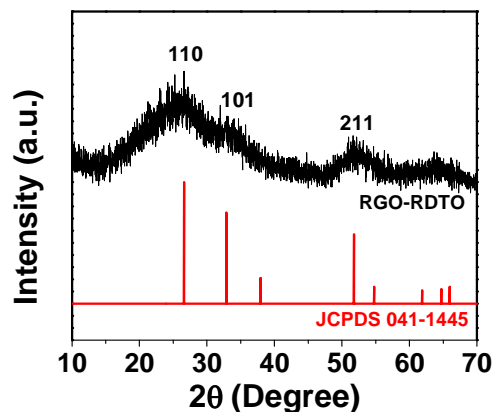


Figure 6.5 XRD pattern of RGO-RDITO nanohybrids.

The surface composition of RGO-IDTO was characterized by XPS. Figure 6.4b shows the entire survey spectra of RGO-IDTO, showing the existence of C, O, In, and Sn in the nanohybrid, consistent with the EDS results. The C/O ratios were 1.8 for the initial GO and 1.6 for RGO-IDTO hybrids based on the XPS analysis. Although our electrical measurements presented later suggest that GO has been effectively reduced to RGO during the synthesis process, it is quite challenging to determine the exact degree of reduction of GO because the oxygen signal in the XPS is from both RGO and IDTO. Figure 6.4c–e show high-resolution XPS spectra of C 1s, Sn 3d, and In 3d, respectively. The complex C 1s XPS spectra can be fitted to three components with peaks centered at 284.6, 286.6, and 288.4 eV, corresponding with C–C, C–O, and C(O)O, respectively. The binding energies of C–O and C(O)O indicate the existence of oxygen groups in RGO.[201] Figure 6.4d presents the Sn 3d level from IDTO, showing two symmetric peaks due to spin–orbit splitting with binding energies of 495.2 and 486.8 eV for the $d_{3/2}$ and $d_{5/2}$ lines, respectively. Similarly, the In 3d level (Figure 6.4e) consists of two peaks centered at 452.4 and 444.8 eV for the $d_{3/2}$ and $d_{5/2}$ lines, respectively. The as-produced RGO-IDTO nanohybrid was also investigated by Raman spectroscopy (Figure 6.4f). The peak at about $1,587\text{ cm}^{-1}$ (G band) corresponds to the in-plane vibration of sp^2 carbon-carbon bonds while the peak at about $1,330\text{ cm}^{-1}$ (D band) is attributed to disorders and defects of the graphitic layer.[212] The D/G intensity ratio (I_D/I_G) indicates the extent of π -conjugation and the defect density in the graphitic layer.[213] The increase of I_D/I_G for RGO-IDTO (1.16) compared with that of GO (1.04) suggests a decrease in

the average size of sp^2 domains and a high concentration of defects, possibly caused by the sonication and reduction process. This increase in I_D/I_G also agrees with other reported results.[214, 215]

Based on our experiments, we believe that the dopant In plays a critical role in the nucleation of the doped tin oxide. For example, when only Sn and GO (no In) were used in the reaction system with the same experimental procedure, the resulting product consisted of aggregated NPs partially covering the RGO surface (Figure 6.6a). The SAED pattern in Figure 6.6b demonstrates that the NPs on RGO have poor crystalline structure, as evidenced by the broad blurry rings. When using In, the time when In is added is important, affecting the final NP dispersion and crystallization. It was found that similar well-defined RGO-IDTO nanohybrid products were obtained when mixing the two ion sources and then adding them into the GO dispersion, as well as when adding In first followed by adding Sn using the same molar ratio of In/Sn=1:1 (Figure 6.2, Figure 6.7a, b). However, when adding Sn before In, the results were similar to those obtained when adding Sn only into the GO dispersion (Figure 6.8). A possible reason is that Sn adsorbs on the GO surface, occupying most of the available ion adsorption sites on the GO surface. Therefore, limited sites are left for In adsorption, resulting in the poor nanoparticle crystallization and dispersion.

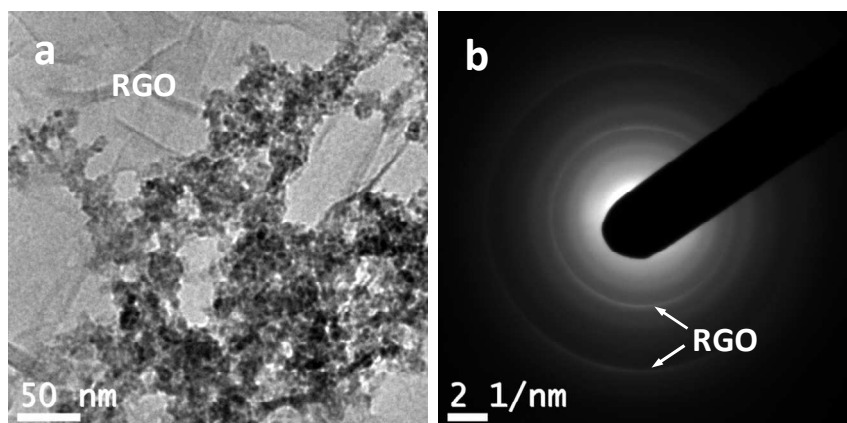


Figure 6.6 TEM image (a) and SAED pattern (b) of product prepared by reducing SnCl_4 on GO using NaBH_4 and the same procedure for preparing RGO-IDTO nanohybrids.

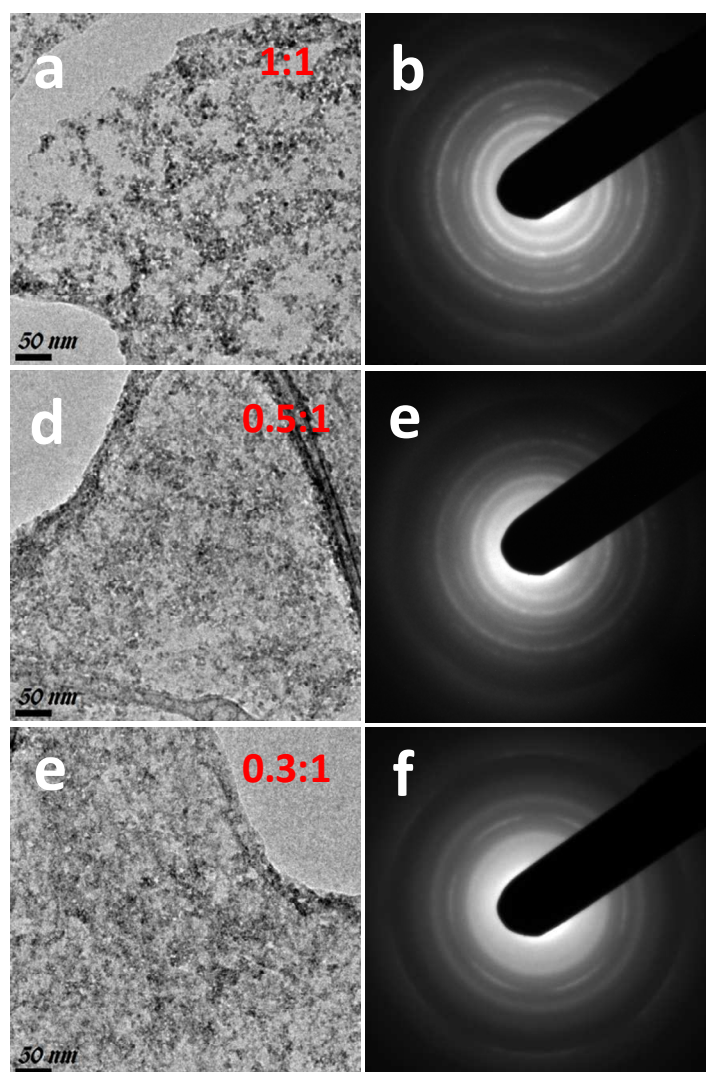


Figure 6.7 TEM images and SAED patterns of RGO-IDTO nanohybrids prepared with In/Sn=1:1 (a, b), 0.5:1 (c, d), 0.3:1 (e, f), respectively.

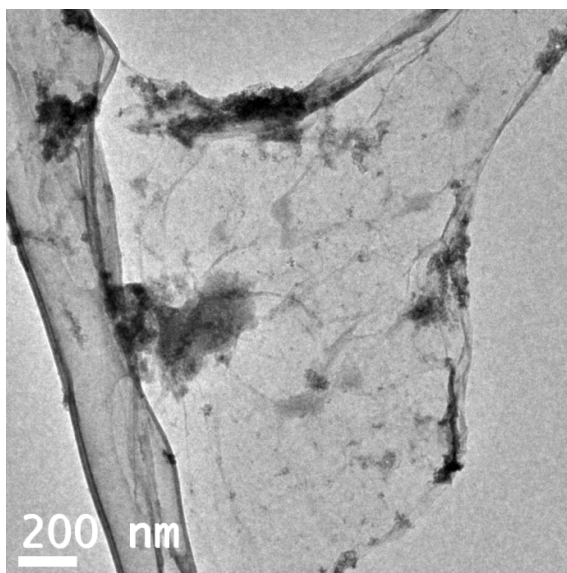


Figure 6.8 TEM image of nanohybrids prepared by adding Sn into the GO dispersion followed by adding In.

Both the presence and the amount of dopant ions play a critical role in the formation of IDTO NPs on the GO surface. To investigate the effect of In on the final product, different amounts of In were used in the synthesis of IDTO NPs while keeping the same amount of Sn, i.e., molar ratios of In/Sn = 1:1, 0.5:1, and 0.3:1. The as-produced nanohybrids were characterized by TEM and SAED, shown in Figure 6.7. It was found that the samples with the largest amount of In (In/Sn=1:1) produced the best crystalline IDTO NPs on the RGO surface (Figure 6.7a, b), as evidenced by the clear nanoparticle distinction and bright sharp SAED rings. The sample synthesized with the smallest amount of In (In/Sn=0.3:1) produced NPs over the RGO surface with broad diffraction rings (Figure 6.7e, f), indicating poor crystallization of IDTO nanoparticles. Therefore, it is reasonable to conclude that In can lower the nucleation energy of NPs, which means that well-defined IDTO nanocrystals would easily form on the GO surface with a higher

concentration of In. We also investigated the function of Ru in the nucleation of RDTO NPs, and found that fine crystalline NPs formed on the RGO when Ru is introduced before adding Sn into the GO dispersion. With the increase of Ru in the solution, a higher density of RDTO nanoparticles formed on the RGO surface (Figure 6.9). Because the dopants encourage the final evenly distributed crystalline NPs on graphene, we propose that the IDTO/RDTO nanocrystals form at positions where dopant ions are located on the GO surface with low nucleation energy at a low temperature.

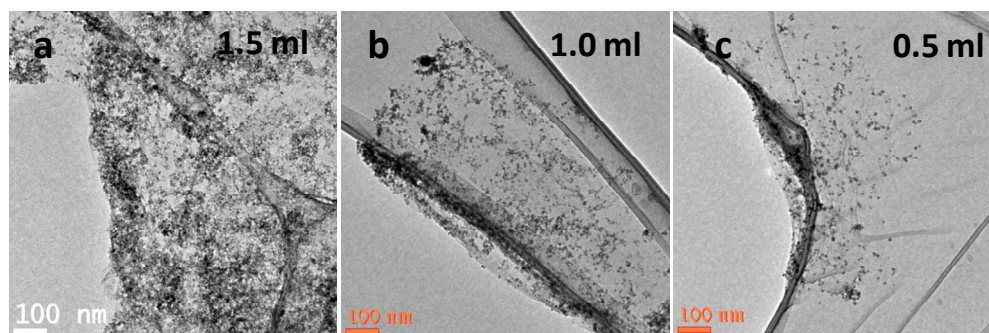


Figure 6.9 TEM images of RGO–RDTO nanohybrids prepared with different amounts of Ru by adding different amounts of RuCl_3 (0.05 M) solutions (e.g., 1.5 ml, 1.0 ml and 0.5 ml) into 8 mg GO dispersion, while adding the same amount of SnCl_4 .

Our previous study showed that SnO_2 nanocrystals enhance the sensing sensitivity of RGO to NO_2 . [201] To prove dopants can further improve the sensing performance, we investigated the sensing properties of RGO–IDTO to NO_2 at room temperature. The dynamic sensing performance of the sensor was measured under different NO_2 concentrations (Figure 6.10a, b). The electrical conductivity of the hybrid sensor increases upon exposure to NO_2 , which is consistent with our previous results for RGO– SnO_2 sensors. Because NO_2 is an oxidizing gas, when NO_2 is adsorbed on SnO_2

surface, we proposed that there is electron transfer from SnO₂ to NO₂. [201, 163] The RGO usually behaves as a p-type semiconductor in air at room temperature and was used as a conducting channel in our device. [197] The electron transfer effectively increases the charge carrier (i.e., hole) concentration in RGO, leading to an increase in electrical conductivity. The results also demonstrate that RGO-IDTO nanohybrids show p-type semiconducting behavior, and the semiconducting type of the RGO was not changed after the IDTO NP decoration.

The sensitivity of the sensor decreases upon exposure to lower concentrations of NO₂. For the NO₂ concentrations investigated (from 0.3 to 100 ppm), the sensing response can be fitted well by an exponential curve, as shown in Figure 6.10c. For low concentration detection, the sensor can respond to a concentration level as low as 0.3 ppm, as shown in Figure 6.10b, which is an order of magnitude lower than the EPA recommended exposure limit (3 ppm). [216] Our sensor thus could be used for room-temperature low concentration NO₂ detection. The recovery process of the sensor, however, is slow, taking overnight to completely recover to the initial state. Further sensor optimization is needed to shorten the recovery time.

To prove the sensing enhancement of dopants to NO₂, the sensitivities were compared for two types of RGO-SnO₂ hybrids fabricated using two different methods. The first series of samples (RGO-SnO₂ I) were synthesized using the hydrothermal method described above. [210] The second series of samples (RGO-SnO₂ II) were synthesized by loading SnO₂ NPs on RGO using a mini-arc plasma source. [201] The sensitivity of the RGO-IDTO nanohybrids is much higher than that of RGO-SnO₂

(Figure 6.10d), indicating that In doping in SnO₂ NPs can greatly enhance the sensitivity. This result can be attributed to the increase of oxygen species (e.g., O^{δ-} adsorbates) on the nanoparticle surface by introducing indium as a dopant. As investigated by density functional theory (DFT) calculations, the interaction between the SnO₂ surface and NO₂ molecules can be described as follows: NO₂ (gas) + O^{δ-} = NO₃^{δ-} (adsorption), where NO₂ is attached to O^{δ-} on the SnO₂ surface, forming a NO₃^{δ-} complex, with electron transfer occurring from the nanoparticle to NO₂. [217] A higher sensitivity suggests more NO₂ molecular adsorption and more electron transfer from the NPs to NO₂. Moreover, it has been found that dopants in SnO₂ increase the number of oxygen vacancies, [218] which in turn can easily dissociate oxygen molecules and thus form chemisorbed oxygen species. [219] Since our samples were exposed to air before testing, oxygen in the air might be dissociated and chemisorbed on the IDTO surface. This is also consistent with other observations that the dopant facilitates adsorption of oxygen molecules and formation of oxygen ions on the SnO₂ surface. [220] The high sensitivity might also be attributed to the tiny size of IDTO nanocrystals due to their large surface-to-volume ratio, which leads to ample adsorption sites in the sensing process and thus an enhanced sensitivity.

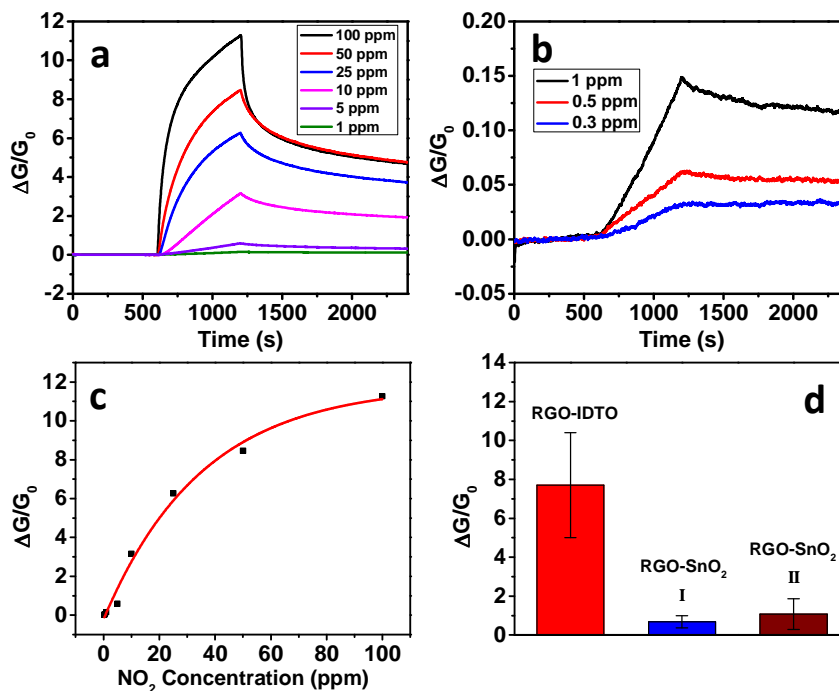


Figure 6.10 (a,b) Dynamic sensing response of RGO-IDTO toward different NO₂ concentrations. (c) Exponential curve of sensitivity as a function of NO₂ concentration. (d) Sensitivity comparison of RGO-IDTO and RGO-SnO₂ nanohybrids to 100 ppm NO₂.

In order to probe the selectivity of RGO-IDTO nanohybrid sensors, the same sensor was measured against several other gases, including H₂S, CO, H₂, and NH₃. The sensing test cycle was the same as that for measuring NO₂, and the dynamic responses are shown in Figure 6.11a. The sensor showed very weak response to all gases except NO₂. The device conductance decreased when the sensor was exposed to NH₃, indicating electron transfer from NH₃ to the nanohybrids. However, the exposure to other gases led to an increase of the conductance, suggesting the electron transfer is in the opposite direction, i.e., from the nanohybrids to the gas molecules. The sensitivity comparison shown in Figure 6.11b demonstrates that the response to other testing gases is negligible compared with that of NO₂, indicating that our sensor has very good selectivity. Here, we suggest a “superposition effect” as one possible mechanism for the high selectivity: Our previous

experimental and theoretical studies showed that SnO₂ selectively enhanced the sensitivity of MWCNTs or RGO to NO₂ at room temperature.[201, 217] It was also reported that multiple In₂O₃ nanowire can achieve selective detection of NO₂ with other chemical gases such as NH₃, O₂, CO, and H₂.[180] Therefore, the differential selectivity of the RGO-IDTO hybrids was maximized by doping indium in SnO₂ for this study due to the same gas selectivity enhancement. However, more work is needed to better understand the underlying mechanism.

For NO₂ detection, other efficient graphene-based hybrid sensors have also been prepared, such as G-WO₃ and RGO-Cu₂O sensors.[221, 222] Compared to the sensing performance of those hybrids, our RGO-IDTO sensor have comparable detection limit with RGO-Cu₂O sensor, which is better than that of G-WO₃. However, the selectivity was not reported for those hybrids, while the RGO-IDTO hybrids reported here have excellent selectivity.

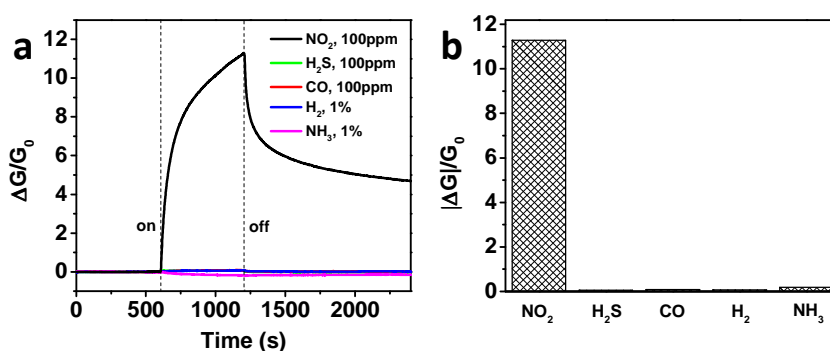


Figure 6.11 Comparison of sensing responses (a) and sensitivity (b) to various gases.

6.3 Summary and conclusions

In summary, RGO-IDTO and RGO-RDTO nanohybrids were successfully synthesized using a simple one-pot aqueous method at low temperature. The morphology characterization results show that In- and Ru-doped SnO₂ NPs are evenly distributed on the RGO surface, and that the dopants are successfully incorporated into the SnO₂ nanocrystals. The size of the doped nanoparticles is very small, about 2–3 nm. The dopants lower the nucleation energy of the ions on GO and lead to crystalline IDTO or RDTO NPs on the RGO surface. Such nanohybrids are very promising for sensitive and selective detection of NO₂. The as-prepared RGO-IDTO showed a much higher sensitivity than RGO-SnO₂, indicating the sensing enhancement function of indium doping. The dopants also induced a large number of oxygen vacancies in the nanocrystals, leading to an increase in the number of surface oxygen ion species that can react with NO₂ gas molecules. The highly selective sensing to NO₂ can be understood as a “superposition effect” of selectivity in the hybrids. This preparation method opens up a simple one-pot approach to synthesize various metal-doped metal oxide nanoparticle-graphene nanohybrids for a wide range of applications such as sensors and catalysis.

CHAPTER 7 SUMMARY AND RECOMMENDATIONS

7.1 Nanoparticle synthesis using mini-arc plasma

Several types of NPs have been synthesized using a mini-arc plasma method. By adjusting the parameters of the system, tungsten oxide NPs, tungsten oxide NRs, tin oxide NPs, mixture of tungsten oxide and tin oxide NPs, and silver NPs were successfully produced. The amount of oxygen in the reactor significantly affected composition and morphology of the as-produced nanomaterials. The control over the nanomaterial morphology and structure was investigated, which provides a thorough understanding of the nanomaterial synthesis process using a mini-arc plasma source and also sheds light on gas-phase nanomaterial synthesis in general. The results from this study can be used to tailor reactor parameters for desired nanomaterial products.

The reactor temperature plays a critical role in the synthesis process. However, the exact temperature in the mini-arc plasma reactor is still unknown or it is not precisely controlled. If the temperature could be measured, the nanoparticle synthesis process can be better controlled and more consistent results can be obtained. To synthesize binary or multi-component nanoparticles with a precise control in composition is still challenging. Therefore, controllable fabrication of multi-component nanoparticles may further expand applications of mini-arc plasma reactors and nanoparticles.

7.2 Silver nanoparticle-decorated CNTs for ammonia sensing

Hybrid structures of silver nanoparticle-decorated CNTs, including MWCNTs and

s-SWCNTs, have been fabricated and demonstrated for room-temperature NH_3 gas sensors. The as-produced MWCNT/Ag NP hybrid sensor showed better sensitivity than MWCNTs and Ag NPs alone. Fast sensing response and recovery were also achieved by the deposition of Ag NPs on MWCNTs. The Ag NPs work as the dominant active sites for NH_3 adsorption in the sensing process. For ammonia sensors based on s-SWCNTs, the SWCNT/Ag NP hybrids exhibit much higher sensitivity than MWCNT/Ag NP hybrids due to the excellent semiconducting properties of SWCNTs. The electron transfer between gas molecules and SWCNTs resulted in significant changes in the charge carrier concentration of SWCNTs, leading to the high sensitivity. Therefore, the CNTs/Ag hybrids are attractive for selective detection of NH_3 at room temperature.

The CNTs assembly on electrodes needs to be improved because the resistance of the devices varies from one to another. Future work is warranted to improve the method for CNT assembly so that device variations can be minimized. A precise control of Ag NP loading density on CNTs and a further study on the effect of the Ag NP loading density on the sensing performance are also needed to optimize the sensing performance of these hybrid structures.

7.3 MWCNTs/SnO₂/Ag hybrid gas sensors

A multi-component hybrid structure consisting of Ag, SnO₂, and MWCNTs has been synthesized by *in situ* NPs deposition using a mini-arc plasma method. Compared with MWCNTs alone and MWCNTs/SnO₂ hybrid structures, the as-produced ternary

MWCNTs/SnO₂/Ag hybrid sensor exhibited higher sensitivity and faster response towards both NO₂ and NH₃ at room temperature. The sensing mechanism of Ag supported by MWCNTs can be explained as “electronic sensitization.” The oxygen atoms on SnO₂ and Ag surface play a critical role in the gas sensing.

These findings provide general guidance to engineer sensitivity and selectivity of CNT-based sensors using binary nanoparticles. However, more understanding on the underlying mechanism is needed in the future because the synergistic interaction between the two types of nanoparticles may have an even higher enhancement effect on sensing than just a simple combination of the two materials. Other metal catalyst nanoparticles may be developed in the future to tune the sensing selectivity of CNT-SnO₂ hybrids; e.g., Pd NPs may be used to enhance the sensor performance for H₂ detection.

7.4 RGO/Ag NP ammonia sensors

RGO/Ag hybrid structures were successfully synthesized *in situ* by direct deposition of Ag NPs onto monolayer RGO. Compared with RGO sensors, these hybrid structures showed enhanced sensing performance to ammonia at room temperature, evidenced by very short response time, high sensitivity, and short recovery time. Compared with MWCNTs/Ag hybrid sensors, RGO/Ag hybrids exhibit higher sensitivity with a similar Ag NP loading density, which is likely due to the high specific surface area of RGO. The density of Ag NPs affects the sensitivity, and there is a maximum sensitivity for a proper loading density. Ag NPs also decrease the response to NO₂, resulting in a better selectivity

of RGO to NH_3 . In the hybrids, Ag NPs act as the dominant sensing sites and a net electron transfer from NH_3 to Ag reduced the carrier concentration in RGO, leading to an increase in resistance.

Because the oxygen-containing functional groups on RGO affect the electrical properties of RGO, future studies may be directed to understand the effect of such oxygen groups on the sensing performance of RGO-based hybrids. Various RGO sheets with different number of oxygen functional groups may be used in the RGO/Ag sensing system to understand their roles in sensing process and optimize the sensing performance.

7.5 Doped SnO_2 -decorated RGO for gas sensors

RGO-IDTO and RGO-RDTO nanohybrids were successfully synthesized using a simple one-pot aqueous method at low temperature. The morphology characterization results show that In- and Ru-doped SnO_2 NPs are evenly distributed on the RGO surface, and that the dopants are successfully incorporated into the SnO_2 nanocrystals. The size of the doped nanoparticles is very small, 2–3 nm. Such nanohybrids are very promising for sensitive and selective detection of NO_2 . The as-prepared RGO-IDTO showed a much higher sensitivity than RGO- SnO_2 , indicating the sensing enhancement function of indium doping. The highly selective sensing to NO_2 can be understood as a “superposition effect” of selectivity in the hybrids. This preparation method opens up a simple one-pot approach to synthesize various metal-doped metal oxide nanoparticle-graphene nanohybrids for a wide range of applications such as sensors and catalysis.

However, the nature of the doping in the resulting nanocrystals and the exact mechanism of doping in the enhancement of sensing performance are unclear. Future studies should be directed to illuminate these key aspects to further understand the doping effect. For example, nanocrystals with different amount of dopants may be synthesized and the influence of the dopant concentration on the sensing performance may be investigated to optimize the sensitivity and the selectivity.

7.6 Comparison of various nanocarbon-based materials for gas sensing

In this dissertation, several types of nanocarbons (MWCNTs, SWCNTs, and RGO) were used in the hybrid gas sensors through combining them with various nanoparticles. The intrinsic properties of both nanocarbons and nanoparticles significantly influence the tunability of sensing performance of these gas sensors. Table 7.1 shows a summary of sensitivity values, response time values, and selectivity (if available) of various nanocarbon-based materials studied in this dissertation, together with some results from previous work by our group on RGO/SnO₂ hybrids (marked with *). To ensure comparability, all the materials are summarized for their sensing responses to 100 ppm NO₂ and 1% NH₃, which are typical oxidizing and reducing pollutants, respectively. The sensitivities are normalized as $S=\Delta G/G_0$ for NO₂, and $S=\Delta R/R_0$ for NH₃ to ensure positive values for the sensitivity. Note that the NP loading density may not be exactly the same for all cases under comparison. Furthermore, all the listed sensitivity values are the maximum values observed in the current study to illustrate the sensing potential of each

material. Response times are normalized as the time needed for the sensor to change over 63.2% of the maximum sensitivity (corresponding to one time constant in a first-order dynamic system).

Table 7.1 Summary of sensitivity, selectivity, and response time for various nanocarbon-based materials

	NO ₂ (100 ppm)					NH ₃ (1%)				
	Materials	S	t (s)	SL	Ref.	Materials	S	t (s)	SL	Ref.
1	SWCNTs	24.4	209		CW	SWCNTs	60	210		CW
2	RGO/In-SnO ₂	11	114	NO ₂ over NH ₃ , H ₂ , CO, H ₂ S	CW [223]	SWCNTs/Ag	3.5	6		CW
3	SWCNTs/SnO ₂	8.8	234		CW	SWCNTs/SnO ₂	1.3	47		CW
4	RGO/SnO ₂ *	1.87	60	NO ₂ over NH ₃	[201]	RGO/SnO ₂ *	0.42	30		[201]
5	RGO*	1.56	100		[201]	RGO/Ag	0.18	6	NH ₃ over NO ₂	CW [224]
6	MWCNTs/SnO ₂ /Ag	0.43	77		CW [186]	MWCNTs/SnO ₂ /Ag	0.12	47		CW [186]
7	MWCNTs/SnO ₂	0.31	126		CW [186]	MWCNTs/Ag	0.09	7	NH ₃ over NO ₂ , H ₂ , CO	CW [184]
8	MWCNTs	0.19	224		CW [186]	RGO	0.05	151		CW [224]
9	RGO/Ag	0.07	15		CW [224]	MWCNTs	0.05	387		CW [184]
10	MWCNTs/Ag	0.04	76		CW [184]	MWCNTs/SnO ₂	0.05	31		CW [186]
11						RGO/In-SnO ₂	0.03	203		CW [223]

*denotes previous work from our research group; S, sensitivity; t, response time; SL, selectivity; CW, current work.

Through comparing the hybrid sensors with the same type of nanoparticles, e.g.,

SnO₂ for NO₂ and Ag for NH₃ as highlighted in red in Table 7.1, semiconducting SWCNTs-based sensors have the highest sensitivity, followed by RGO- and MWCNTs-based sensors, suggesting that semiconducting SWCNTs are the most attractive for gas sensing and thus offer superior tunability in sensing performance. This can be attributed to the relatively low charge carrier concentration in semiconducting SWCNTs; a net electron transfer induced by gas adsorption can result in a substantial change in the charge carrier concentration and thus the electrical conductance. However, RGO and MWCNTs exhibit more metallic than semiconducting behavior and have relatively higher charge carrier concentrations so that small electron transfer cannot significantly modify the electrical conductance of RGO or MWCNTs.

A significant contribution of nanoparticles in the nanocarbon-based hybrids is their capability to tune the sensing selectivity and the response time. For example, hybrids of Ag NP-decorated MWCNTs show selectivity for sensing NH₃; In-doped SnO₂ NPs greatly improve the selectivity of RGO/In-SnO₂ hybrid sensors for NO₂. Doped metal oxides on nanocarbons could be an efficient pathway to improve the hybrid sensor selectivity as suggested from the sensing performance of RGO/In-SnO₂ hybrid sensors. Except when defects dominate the sensitivity of nanocarbons (e.g., s-SWCNTs), nanoparticle decoration on nanocarbons typically not only improves the sensitivity and selectivity but also enhances the response time. For example, the response times for bare SWCNTs, MWCNTs, and RGO to 1% NH₃ are all on the order of minutes. After Ag NPs decoration, the response times are around 6 s. Therefore, carefully selected nanoparticles have great potential to regulate the sensing performance of nanocarbon-based gas sensors.

ACKNOWLEDGEMENT

Firstly I would like to thank my supervisor, Prof. Junhong Chen, for his considerable guidance during my Ph.D. study. He gives me huge support not only in my research, but also in my life. Furthermore, I acknowledge the financial support from the National Science Foundation (CMMI-0856753 and CMMI-0900509). The SEM imaging and EDS were conducted at the Electron Microscope Laboratory of University of Wisconsin-Milwaukee (UWM). TEM analyses were conducted in the UWM HRTEM Laboratory. XRD, XPS, and RAMAN analyses were conducted in the Advanced Analysis Facility (AAF) of UWM. The sensor electrodes were fabricated in the Center for Nanoscale Materials of Argonne National Laboratory. I thank Prof. Marija Gajdardziska-Josifovska and Mr. Donald Roberson for technical support with TEM analyses; Dr. H. A. Owen for technical support with SEM analyses; Mr. Steven E. Hardcastle for technical support with XRD, XPS, and RAMAN analyses. The RGO was provided by Dr. Shun Mao (UWM). The gold electrodes were provided by Dr. Ganhua Lu, Dr. Kehung Chen and Dr. Yang Zhang. I also thank all the members in my lab who gave me support during my Ph.D. program.

REFERENCES

- [1] Liu S J and Tubino M, *Analytica Chimica Acta* **1998**, 366, 5.
- [2] Iftimie N, Rezlescu E, Popa P D and Rezlescu N, *Journal of Optoelectronics and Advanced Materials* **2006**, 8, 1001.
- [3] Albert K J, Lewis N S, Schauer C L, Sotzing G A, Stitzel S E, Vaid T P and Walt D R, *Chemical Reviews* **2000**, 100, 2595.
- [4] Kryshstal R G, Kundin A P, Medved A V and Shemet V V, *Technical Physics* **2002**, 47, 1316.
- [5] Slater J M, Paynter J and Watt E J, *Analyst* **1993**, 118, 379.
- [6] Srivastava A, Singh V, Dhand C, Kaur M, Singh T, Witte K and Scherer U W, *Sensors* **2006**, 6, 262.
- [7] Waghuley S A, Yenorkar S M, Yawale S S and Yawale S P, *Sensors and Actuators B-Chemical* **2008**, 128, 366.
- [8] Xue M Q, Ma X L, Xie Z A, Duan L T, Jiang Y Q, Zhang M N and Cao T B, *Chemistry-an Asian Journal* **2010**, 5, 2266.
- [9] Inoue T, Ohtsuka K, Yoshida Y, Matsuura Y and Kajiyama Y, *Sensors and Actuators B-Chemical* **1995**, 25, 388.
- [10] Kim Y S, Ha S C, Kim K, Yang H, Choi S Y, Kim Y T, Park J T, Lee C H, Choi J, Paek J and Lee K, *Applied Physics Letters* **2005**, 86, 213105.
- [11] Kunimoto A, Abe N, Uchida H and Katsube T, *Sensors and Actuators B-Chemical* **2000**, 65, 122.
- [12] Zhang W Y, Uchida H, Katsube T, Nakatsubo T and Nishioka Y, *Sensors and Actuators B-Chemical* **1998**, 49, 58.
- [13] Agbor N E, Cresswell J P, Petty M C and Monkman A P, *Sensors and Actuators B-Chemical* **1997**, 41, 137.
- [14] Martucci A, Bassiri N, Guglielmi M, Armelao L, Gross S and Pivin J C, *Journal of Sol-Gel Science and Technology* **2003**, 26, 993.
- [15] Choi K J and Jang H W, *Sensors* **2010**, 10, 4083.

- [16] Batzill M and Diebold U, *Progress in Surface Science* **2005**, 79, 47.
- [17] Yu K, Wu Z C, Zhao Q R, Li B X and Xie Y, *Journal of Physical Chemistry C* **2008**, 112, 2244.
- [18] Kiyonaga T, Akita T and Tada H, *Chemical Communications* **2009**, 15, 2011.
- [19] Mao S, Lu G H, Yu K H and Chen J H, *Carbon* **2010**, 48, 479.
- [20] Du N, Zhang H, Ma X Y and Yang D, *Chemical Communications* **2008**, 6182.
- [21] Duan X F, Huang Y, Cui Y, Wang J F and Lieber C M, *Nature* **2001**, 409, 66.
- [22] Rumyantseva M N, Gaskov A M, Rosman N, Pagnier T and Morante J R, *Chemistry of Materials* **2005**, 17, 893.
- [23] Reyes L, Hoel A, Saukko S, Heszler P, Lantto V and Granqvist C G, *Sensors and Actuators B-Chemical* **2006**, 117, 128.
- [24] Ahn M W, Park K S, Heo J H, Park J G, Kim D W, Choi K J, Lee J H and Hong S H, *Applied Physics Letters* **2008**, 93, 263103.
- [25] Choi Y J, Hwang I S, Park J G, Choi K J, Park J H and Lee J H, *Nanotechnology* **2008**, 19, 095508.
- [26] Sadek A Z, Choopun S, Wlodarski W, Ippolito S J and Kalantar-zadeh K, *Ieee Sensors Journal* **2007**, 7, 919.
- [27] Jeong S Y, Kim K K, An K H, Hwang H R, Han C S, Yun M H and Lee Y H, *Nano* **2006**, 1, 235.
- [28] Chen J, Xu L N, Li W Y and Gou X L, *Advanced Materials* **2005**, 17, 582.
- [29] Liu J Y, Guo Z, Meng F L, Luo T, Li M Q and Liu J H, *Nanotechnology* **2009**, 20, 125501.
- [30] Chu X F, Jiang D L and Zheng C M, *Sensors and Actuators B-Chemical* **2007**, 123, 793.
- [31] Zhang J T, Liu J F, Peng Q, Wang X and Li Y D, *Chemistry of Materials* **2006**, 18, 867.
- [32] Firooz A A, Mahjoub A R and Khodadadi A A, *Sensors and Actuators B-Chemical* **2009**, 141, 89.
- [33] Moshfegh A Z, *Journal of Physics D-Applied Physics* **2009**, 42, 233001.

- [34] Waszczuk P, Barnard T M, Rice C, Masel R I and Wieckowski A, *Electrochemistry Communications* **2002**, 4, 599.
- [35] Nakayama K, Tanabe K and Atwater H A, *Applied Physics Letters* **2008**, 93, 121904.
- [36] Li H, Xu J Q, Zhu Y H, Chen X D and Xiang Q, *Talanta* **2010**, 82, 458.
- [37] Lu G H, Huebner K L, Ocola L E, Gajdardziska-Josifovska M and Chen J H, *Journal of Nanomaterials* **2006**, 2006, 20.
- [38] Sun J F, Guo L, Bao Y and Xie J W, *Biosensors & Bioelectronics* **2011**, 28, 152.
- [39] Jin S and Ye K M, *Biotechnology Progress* **2007**, 23, 32.
- [40] Jang H D, Seong C M, Chang H K and Kim H C, *Current Applied Physics* **2006**, 6, 1044.
- [41] Chiu H C and Yeh C S, *Journal of Physical Chemistry C* **2007**, 111, 7256.
- [42] Fan H Y and Reid S A, *Chemistry of Materials* **2003**, 15, 564.
- [43] Mochida T, Kikuchi K, Kondo T, Ueno H and Matsuura Y, *Sensors and Actuators B-Chemical* **1995**, 25, 433.
- [44] Keskinen H, Tricoli A, Marjamaki M, Makela J M and Pratsinis S E, *Journal of Applied Physics* **2009**, 106, 084316.
- [45] Strobel R and Pratsinis S E, *Journal of Materials Chemistry* **2007**, 17, 4743.
- [46] Zhu L Y, Lu G H, Mao S, Chen J H, Dikin D A, Chen X Q and Ruoff R S, *Nano* **2007**, 2, 149.
- [47] Zheng N F and Stucky G D, *Journal of the American Chemical Society* **2006**, 128, 14278.
- [48] Wei X W, Zhu G X, Liu Y J, Ni Y H, Song Y and Xu Z, *Chemistry of Materials* **2008**, 20, 6248.
- [49] Lu Y, Yin Y D, Mayers B T and Xia Y N, *Nano Letters* **2002**, 2, 183.
- [50] Iijima S, *Nature* **1991**, 354, 56.
- [51] Ebbesen T W and Ajayan P M, *Nature* **1992**, 358, 220.
- [52] Tanaka M and Watanabe T, *Thin Solid Films* **2008**, 516, 6645.

- [53] Hao C C, Xiao F and Cui Z L, *Journal of Nanoparticle Research* **2008**, 10, 47.
- [54] Shimizu Y, Kawaguchi K, Sasaki T and Koshizaki N, *Applied Physics Letters* **2009**, 94, 191504.
- [55] Chazelas C, Coudert J F, Jarrige J and Fauchais P, *Journal of the European Ceramic Society* **2006**, 26, 3499.
- [56] Banerjee I, Karmakar S, Kulkarni N V, Nawale A B, Mathe V L, Das A K and Bhoraskar S V, *Journal of Nanoparticle Research* **2010**, 12, 581.
- [57] Cvelbar U, Chen Z Q, Sunkara M K and Mozetic M, *Small* **2008**, 4, 1610.
- [58] Ono H and Iizuka S, *Thin Solid Films* **2009**, 518, 1016.
- [59] Ogawa H, Nishikawa M and Abe A, *Journal of Applied Physics* **1982**, 53, 4448
- [60] Ionescu R, Hoel A, Granqvist C G, Llobet E and Heszler P, *Sensors and Actuators B-Chemical* **2005**, 104, 132.
- [61] Rahman M M, Jamal A, Khan S B and Faisal M, *Biosensors & Bioelectronics* **2011**, 28, 127.
- [62] Rahman M M, Jamal A, Khan S B and Faisal M, *Journal of Physical Chemistry C* **2011**, 115, 9503.
- [63] Coey J M D, Venkatesan M and Fitzgerald C B, *Nature Materials* **2005**, 4, 173.
- [64] Vaishampayan M V, Deshmukh R G, Walke P and Mulla I S, *Materials Chemistry and Physics* **2008**, 109, 230.
- [65] Dolbec R and El Khakani M A, *Applied Physics Letters* **2007**, 90, 173114.
- [66] Kumar V, Sen S, Muthe K P, Gaur N K, Gupta S K and Yakhmi J V, *Sensors and Actuators B-Chemical* **2009**, 138, 587.
- [67] Canevali C, Mari C M, Mattoni M, Morazzoni F, Nodari L, Ruffo R, Russo U and Scotti R, *Journal of Physical Chemistry B* **2005**, 109, 7195.
- [68] Thostenson E T, Ren Z F and Chou T W, *Composites Science and Technology* **2001**, 61, 1899.
- [69] Jones D E H, *Nature* **1996**, 381, 384.

- [70] Donaldson K, Aitken R, Tran L, Stone V, Duffin R, Forrest G and Alexander A, *Toxicological Sciences* **2006**, 92, 5.
- [71] Jorio A, Saito R, Hafner J H, Lieber C M, Hunter M, McClure T, Dresselhaus G and Dresselhaus M S, *Physical Review Letters* **2001**, 86, 1118.
- [72] Hou P X, Xu S T, Ying Z, Yang Q H, Liu C and Cheng H M, *Carbon* **2003**, 41, 2471.
- [73] Ajayan P M and Iijima S, *Nature* **1992**, 358, 23.
- [74] Iijima S and Ichihashi T, *Nature* **1993**, 363, 603.
- [75] Chiang M R, Liu K S, Lai T S, Tsai C H, Cheng H F and Lin I N, *Journal of Vacuum Science & Technology B* **2001**, 19, 1034.
- [76] Kanzow H, Schmalz A and Ding A, *Chemical Physics Letters* **1998**, 295, 525.
- [77] Journet C and Bernier P, *Applied Physics a-Materials Science & Processing* **1998**, 67, 1.
- [78] Deng W Q, Xu X and Goddard W A, *Nano Letters* **2004**, 4, 2331.
- [79] Wei Y Y, Eres G, Merkulov V I and Lowndes D H, *Applied Physics Letters* **2001**, 78, 1394.
- [80] Takagi D, Homma Y, Hibino H, Suzuki S and Kobayashi Y, *Nano Letters* **2006**, 6, 2642.
- [81] Collins P G and Avouris P, *Scientific American* **2000**, 283, 62.
- [82] Deheer W A, Chatelain A and Ugarte D, *Science* **1995**, 270, 1179.
- [83] Li J, Lu Y J, Ye Q, Cinke M, Han J and Meyyappan M, *Nano Letters* **2003**, 3, 929.
- [84] Slobodian P, Riha P, Lengalova A, Svoboda P and Saha P, *Carbon* **2011**, 49, 2499.
- [85] Minot E D, Janssens A M, Heller I, Heering H A, Dekker C and Lemay S G, *Applied Physics Letters* **2007**, 91, 093507.
- [86] Che G L, Lakshmi B B, Fisher E R and Martin C R, *Nature* **1998**, 393, 346.
- [87] Lee S M and Lee Y H, *Applied Physics Letters* **2000**, 76, 2877.
- [88] Ruoff R S and Lorents D C, *Carbon* **1995**, 33, 925.
- [89] Zhao J J, *Current Nanoscience* **2005**, 1, 169.

- [90] Collins P G, Bradley K, Ishigami M and Zettl A, *Science* **2000**, 287, 1801.
- [91] Goldoni A, Petaccia L, Gregoratti L, Kaulich B, Barinov A, Lizzit S, Laurita A, Sangaletti L and Larciprete R, *Carbon* **2004**, 42, 2099.
- [92] Valentini L, Armentano I, Kenny J M, Cantalini C, Lozzi L and Santucci S, *Applied Physics Letters* **2003**, 82, 961.
- [93] Hoa N D, Quy N V and Kim D, *Sensors and Actuators B-Chemical* **2009**, 142, 253.
- [94] Kong J, Chapline M G and Dai H J, *Advanced Materials* **2001**, 13, 1384.
- [95] Yang M, Kim D H, Kim W S, Kang T J, Lee B Y, Hong S, Kim Y H and Hong S H, *Nanotechnology* **2010**, 21,
- [96] Espinosa E H, Lonescu R, Bittencourt C, Felten A, Erni R, Van Tendeloo G, Pireaux J J and Llobet E, *Thin Solid Films* **2007**, 515, 8322.
- [97] Novoselov K S, Geim A K, Morozov S V, Jiang D, Zhang Y, Dubonos S V, Grigorieva I V and Firsov A A, *Science* **2004**, 306, 666.
- [98] Geim A K and Novoselov K S, *Nature Materials* **2007**, 6, 183.
- [99] Bhaviripudi S, Jia X T, Dresselhaus M S and Kong J, *Nano Letters* **2010**, 10, 4128.
- [100] Li X S, Cai W W, An J H, Kim S, Nah J, Yang D X, Piner R, Velamakanni A, Jung I, Tutuc E, Banerjee S K, Colombo L and Ruoff R S, *Science* **2009**, 324, 1312.
- [101] Chae S J, Gunes F, Kim K K, Kim E S, Han G H, Kim S M, Shin H J, Yoon S M, Choi J Y, Park M H, Yang C W, Pribat D and Lee Y H, *Advanced Materials* **2009**, 21, 2328.
- [102] Lee S, Lee K and Zhong Z H, *Nano Letters* **2010**, 10, 4702.
- [103] Brar V W, Zhang Y, Yayon Y, Ohta T, McChesney J L, Bostwick A, Rotenberg E, Horn K and Crommie M F, *Applied Physics Letters* **2007**, 91, 122102.
- [104] Gomez-Navarro C, Weitz R T, Bittner A M, Scolari M, Mews A, Burghard M and Kern K, *Nano Letters* **2007**, 7, 3499.
- [105] Hummers Jr. W S and Offeman R E, *Journal of the American Chemical Society* **1958**, 80, 1339.
- [106] Kosynkin D V, Higginbotham A L, Sinitskii A, Lomeda J R, Dimiev A, Price B K and Tour J M, *Nature* **2009**, 458, 872.

- [107] Li X L, Wang X R, Zhang L, Lee S W and Dai H J, *Science* **2008**, 319, 1229.
- [108] Bolotin K I, Sikes K J, Jiang Z, Klima M, Fudenberg G, Hone J, Kim P and Stormer H L, *Solid State Communications* **2008**, 146, 351.
- [109] Morozov S V, Novoselov K S, Katsnelson M I, Schedin F, Elias D C, Jaszczak J A and Geim A K, *Physical Review Letters* **2008**, 100, 16602.
- [110] Balandin A A, Ghosh S, Bao W Z, Calizo I, Teweldebrhan D, Miao F and Lau C N, *Nano Letters* **2008**, 8, 902.
- [111] Kim K S, Zhao Y, Jang H, Lee S Y, Kim J M, Kim K S, Ahn J H, Kim P, Choi J Y and Hong B H, *Nature* **2009**, 457, 706.
- [112] Wang X, Zhi L J and Mullen K, *Nano Letters* **2008**, 8, 323.
- [113] Lu G H, Ocola L E and Chen J H, *Nanotechnology* **2009**, 20, 445502.
- [114] Fowler J D, Allen M J, Tung V C, Yang Y, Kaner R B and Weiller B H, *ACS Nano* **2009**, 3, 301.
- [115] Farmer D B, Chiu H Y, Lin Y M, Jenkins K A, Xia F N and Avouris P, *Nano Letters* **2009**, 9, 4474.
- [116] Cui L L, Lu X F, Chao D M, Liu H T, Li Y X and Wang C, *Physica Status Solidi a-Applications and Materials Science* **2011**, 208, 459.
- [117] Stankovich S, Dikin D A, Dommett G H B, Kohlhaas K M, Zimney E J, Stach E A, Piner R D, Nguyen S T and Ruoff R S, *Nature* **2006**, 442, 282.
- [118] Wang H L, Cui L F, Yang Y A, Casalongue H S, Robinson J T, Liang Y Y, Cui Y and Dai H J, *Journal of the American Chemical Society* **2010**, 132, 13978.
- [119] Lu G H, Ocola L E and Chen J H, *Applied Physics Letters* **2009**, 94, 083111.
- [120] Zhang L S, Wang W D, Liang X Q, Chu W S, Song W G, Wang W and Wu Z Y, *Nanoscale* **2011**, 3, 2458.
- [121] Johnson J L, Behnam A, Pearton S J and Ural A, *Advanced Materials* **2010**, 22, 4877.
- [122] Zhang Z Y, Zou R J, Song G S, Yu L, Chen Z G and Hu J Q, *Journal of Materials Chemistry* **2011**, 21, 17360.
- [123] Jiang Z X, Wang J J, Meng L H, Huang Y D and Liu L, *Chemical Communications* **2011**,

47, 6350.

- [124] Cho W S, Moon S I, Lee Y D, Lee Y H, Park J H and Ju B K, *Ieee Electron Device Letters* **2005**, 26, 498.
- [125] Cho W S, Moon S I, Paek K K, Lee Y H, Park J H and Ju B K, *Sensors and Actuators B-Chemical* **2006**, 119, 180.
- [126] Kong J, Franklin N R, Zhou C W, Chapline M G, Peng S, Cho K J and Dai H J, *Science* **2000**, 287, 622.
- [127] Pengfei Q F, Vermesh O, Grecu M, Javey A, Wang O, Dai H J, Peng S and Cho K J, *Nano Letters* **2003**, 3, 347.
- [128] Sasaki I, Minami N, Karthigeyan A and Iakoubovskii K, *Analyst* **2009**, 134, 325.
- [129] Kauffman D R, Sorescu D C, Schofield D P, Allen B L, Jordan K D and Star A, *Nano Letters* **2010**, 10, 958.
- [130] Mubeen S, Zhang T, Chartuprayoon N, Rheem Y, Mulchandani A, Myung N V and Deshusses M A, *Analytical Chemistry* **2010**, 82, 250.
- [131] Li W, Hoa N D and Kim D, *Sensors and Actuators B-Chemical* **2010**, 149, 184.
- [132] Star A, Joshi V, Skarupo S, Thomas D and Gabriel J C P, *Journal of Physical Chemistry B* **2006**, 110, 21014.
- [133] Brahim S, Colbern S, Gump R, Moser A and Grigorian L, *Nanotechnology* **2009**, 20, 235502.
- [134] Brahim S, Colbern S, Gump R and Grigorian L, *Journal of Applied Physics* **2008**, 104, 024502.
- [135] Nguyen L H, Phi T V, Phan P Q, Vu H N, Nguyen-Duc C and Fossard F, *Physica E-Low-Dimensional Systems & Nanostructures* **2007**, 37, 54.
- [136] Mangu R, Rajaputra S and Singh V P, *Nanotechnology* **2011**, 22, 215502.
- [137] Hashmi A S K and Hutchings G J, *Angewandte Chemie-International Edition* **2006**, 45, 7896.
- [138] Yamazoe N, *Sensors and Actuators B-Chemical* **1991**, 5, 7.
- [139] Kolmakov A, Klenov D O, Lilach Y, Stemmer S and Moskovits M, *Nano Letters* **2005**, 5,

667.

- [140] Vedala H, Sorescu D C, Kotchey G P and Star A, *Nano Letters* **2011**, 11, 2342.
- [141] Tjoa V, Jun W, Dravid V, Mhaisalkar S and Mathews N, *Journal of Materials Chemistry* **2011**, 21, 15593.
- [142] Song H J, Zhang L C, He C L, Qu Y, Tian Y F and Lv Y, *Journal of Materials Chemistry* **2011**, 21, 5972.
- [143] Chen J H, Lu G H, Zhu L Y and Flagan R C, *Journal of Nanoparticle Research* **2007**, 9, 203.
- [144] Bursill L A, *Journal of Solid State Chemistry* **1983**, 48, 256.
- [145] Simchi A, Ahmadi R, Reihani S M S and Mahdavi A, *Materials & Design* **2007**, 28, 850.
- [146] Kimura Y, Miura H, Tsukamoto K, Li C R and Maki T, *Journal of Crystal Growth* **2011**, 316, 196.
- [147] Cui S M, Lu G H, Mao S, Yu K H and Chen J H, *Chemical Physics Letters* **2010**, 485, 64.
- [148] Hartanto A B, Ning X, Nakata Y and Okada T, *Applied Physics a-Materials Science & Processing* **2004**, 78, 299.
- [149] Pimtong-Ngam Y, Jiemsirilers S and Supothina S, *Sensors and Actuators a-Physical* **2007**, 139, 7.
- [150] Mahoney W and Andres R P, *Materials Science and Engineering a-Structural Materials Properties Microstructure and Processing* **1995**, 204, 160.
- [151] Collins G S, Kachnowski T, Benczer-Koller N and Pasternak M, *Physical Review B* **1979**, 19, 1369.
- [152] Huh M Y, Kim S H, Ahn J P, Park J K and Kim B K, *Nanostructured Materials* **1999**, 11, 211.
- [153] Lu B, Wang C S and Zhang Y H, *Applied Physics Letters* **1997**, 70, 717.
- [154] Yang A, Tao X M, Pang G K H and Siu K G G, *Journal of the American Ceramic Society* **2008**, 91, 257.
- [155] Rellinghaus B, Lindackers D, Kockerling M, Roth P and Wassermann E F, *Phase Transitions* **2003**, 76, 347.

- [156] Buesser B, Heine M C and Pratsinis S E, *Journal of Aerosol Science* **2009**, 40, 89.
- [157] Joshi R K, Kruis F E and Dmitrieva O, *Journal of Nanoparticle Research* **2006**, 8, 797.
- [158] Dai Z R, Gole J L, Stout J D and Wang Z L, *Journal of Physical Chemistry B* **2002**, 106, 1274.
- [159] Dai Z R, Pan Z W and Wang Z L, *Solid State Communications* **2001**, 118, 351.
- [160] Khakpash N, Simchi A and Kohi P, *Journal of Alloys and Compounds* **2009**, 470, 289.
- [161] Tao X M, Yang A, Pang G K H and Siu K G G, *Journal of the American Ceramic Society* **2008**, 91, 257.
- [162] Cui S M, Mattson E C, Lu G H, Hirschmugl C, Gajdardziska-Josifovska M and Chen J H, *Journal of Nanoparticle Research* **2012**, 14, 744.
- [163] Lu G H, Ocola L E and Chen J H, *Advanced Materials* **2009**, 21, 2487.
- [164] Mao S, Cui S M, Yu K H, Wen Z H, Lu G H and Chen J H, *Nanoscale* **2012**, 11, 1275.
- [165] Zhang Y, Cui S M, Chang J B, Ocola L E and Chen J H, *Nanotechnology* **2013**, 24, 025503.
- [166] Odom T W, Huang J L, Kim P and Lieber C M, *Nature* **1998**, 391, 62.
- [167] Bachtold A, Strunk C, Salvetat J P, Bonard J M, Forro L, Nussbaumer T and Schonenberger C, *Nature* **1999**, 397, 673.
- [168] Peng N, Zhang Q, Chow C L, Tan O K and Marzari N, *Nano Letters* **2009**, 9, 1626.
- [169] Raju N R C, Kumar K J and Subrahmanyam A, *Journal of Physics D-Applied Physics* **2009**, 42, 135411.
- [170] Giovannetti G, Khomyakov P A, Brocks G, Karpan V M, van den Brink J and Kelly P J, *Physical Review Letters* **2008**, 101, 026803.
- [171] Murray B J, Walter E C and Penner R M, *Nano Letters* **2004**, 4, 665.
- [172] Robinson J A, Snow E S, Badescu S C, Reinecke T L and Perkins F K, *Nano Letters* **2006**, 6, 1747.
- [173] Zhao J J, Buldum A, Han J and Lu J P, *Nanotechnology* **2002**, 13, 195.

- [174] Bartolucci F, Franchy R, Barnard J C and Palmer R E, *Physical Review Letters* **1998**, 80, 5224.
- [175] Petrov V V, Nazarova T N, Korolev A and Kopilova N F, *Sensors and Actuators B-Chemical* **2008**, 133, 291.
- [176] Lu G H, Yu K H, Ocola L E and Chen J H, *Chemical Communications* **2011**, 47, 7761.
- [177] Schedin F, Geim A K, Morozov S V, Hill E W, Blake P, Katsnelson M I and Novoselov K S, *Nature Materials* **2007**, 6, 652.
- [178] Lu G H, Park S, Yu K H, Ruoff R S, Ocola L E, Rosenmann D and Chen J H, *ACS Nano* **2011**, 5, 1154.
- [179] Durkop T, Getty S A, Cobas E and Fuhrer M S, *Nano Letters* **2004**, 4, 35.
- [180] Zhang D H, Liu Z Q, Li C, Tang T, Liu X L, Han S, Lei B and Zhou C W, *Nano Letters* **2004**, 4, 1919.
- [181] Del Bubba M, Arias C A and Brix H, *Water Research* **2003**, 37, 3390.
- [182] Xue Y Q and Datta S, *Physical Review Letters* **1999**, 83, 4844.
- [183] Ellison M D, Crotty M J, Koh D, Spray R L and Tate K E, *Journal of Physical Chemistry B* **2004**, 108, 7938.
- [184] Cui S M, Pu H H, Lu G H, Wen Z H, Mattson E C, Hirschmugl C, Gajdardziska-Josifovska M, Weinert M and Chen J H, *Acs Applied Materials & Interfaces* **2012**, 4, 4898.
- [185] Kim S, Lee H R, Yun Y J, Ji S, Yoo K, Yun W S, Koo J Y and Ha D H, *Applied Physics Letters* **2007**, 91, 093126.
- [186] Cui S M, Pu H H, Mattson E C, Lu G H, Mao S, Weinert M, Hirschmugl C J, Gajdardziska-Josifovska M and Chen J H, *Nanoscale* **2012**, 4, 5887.
- [187] Arab M, Berger F, Picaud F, Ramseyer C, Glory J and Mayne-L'Hermite M, *Chemical Physics Letters* **2006**, 433, 175.
- [188] Snow E S, Perkins F K and Robinson J A, *Chemical Society Reviews* **2006**, 35, 790.
- [189] Chen R J, Franklin N R, Kong J, Cao J, Tomblor T W, Zhang Y G and Dai H J, *Applied Physics Letters* **2001**, 79, 2258.

- [190] Liu P, Sun Q, Zhu F, Liu K, Jiang K, Liu L, Li Q and Fan S, *Nano Letters* **2008**, 8, 647.
- [191] Gurlo A, *Chemphyschem* **2006**, 7, 2041.
- [192] Mulheran P A and Harding J H, *Modelling and Simulation in Materials Science and Engineering* **1992**, 1, 39.
- [193] An W, Wu X J and Zeng X C, *Journal of Physical Chemistry C* **2008**, 112, 5747.
- [194] Chung J Y, Lee K H, Lee J, Troya D and Schatz G C, *Nanotechnology* **2004**, 15, 1596.
- [195] Leenaerts O, Partoens B and Peeters F M, *Physical Review B* **2008**, 77, 125416.
- [196] Rout C S, Hegde M, Govindaraj A and Rrao C N, *Nanotechnology* **2007**, 18, 205504.
- [197] Mao S, Yu K H, Cui S M, Bo Z, Lu G H and Chen J H, *Nanoscale* **2011**, 3, 2849.
- [198] Cui S M, Mattson E C, Lu G H, Hirschmugl C, Gajdardziska-Josifovska M and Chen J H, *Journal of Nanoparticle Research* **2012**, 14, 744.
- [199] Fasolino A, Los J H and Katsnelson M I, *Nature Materials* **2007**, 6, 858.
- [200] Tian J Q, Liu S, Zhang Y W, Li H Y, Wang L, Luo Y L, Asiri A M, Al-Youbi A O and Sun X P, *Inorganic Chemistry* **2012**, 51, 4742.
- [201] Mao S, Cui S M, Lu G H, Yu K H, Wen Z H and Chen J H, *Journal of Materials Chemistry* **2012**, 22, 11009.
- [202] Kaniyoor A, Jafri R I, Arockiadoss T and Ramaprabhu S, *Nanoscale* **2009**, 1, 382.
- [203] Lu G H, Yu K H, Ocola L E and Chen J H, *Chemical Communications* **2011**, 47, 7761.
- [204] Mao S, Cui S M, Yu K H, Wen Z H, Lu G H and Chen J H, *Nanoscale* **2012**, 4, 1275.
- [205] Russo P A, Donato N, Leonardi S G, Baek S, Conte D E, Neri G and Pinna N, *Angewandte Chemie-International Edition* **2012**, 51, 11053.
- [206] Hume-Rothery W 1969 *The structure of metals and alloys* (London: Institute of Metals)
- [207] Shigesato Y, Hayashi Y and Haranoh T, *Applied Physics Letters* **1992**, 61, 73.
- [208] Ramgir N S, Hwang Y K, Mulla I S and Chang J S, *Solid State Sciences* **2006**, 8, 359.
- [209] Nguyen P, Ng H T, Kong J, Cassell A M, Quinn R, Li J, Han J, McNeil M and

- Meyyappan M, *Nano Letters* **2003**, 3, 925.
- [210] Zhang L S, Jiang L Y, Yan H J, Wang W D, Wang W, Song W G, Guo Y G and Wan L J, *Journal of Materials Chemistry* **2010**, 20, 5462.
- [211] Wang Y D, Brezesinski T, Antonietti M and Smarsly B, *ACS Nano* **2009**, 3, 1373.
- [212] Kudin K N, Ozbas B, Schniepp H C, Prud'homme R K, Aksay I A and Car R, *Nano Letters* **2008**, 8, 36.
- [213] Stankovich S, Dikin D A, Piner R D, Kohlhaas K A, Kleinhammes A, Jia Y, Wu Y, Nguyen S T and Ruoff R S, *Carbon* **2007**, 45, 1558.
- [214] Xu C H, Sun J and Gao L, *Nanoscale* **2012**, 4, 5425.
- [215] Zhang M, Lei D, Du Z F, Yin X M, Chen L B, Li Q H, Wang Y G and Wang T H, *Journal of Materials Chemistry* **2011**, 21, 1673.
- [216] Brunekreef B and Holgate S T, *Lancet* **2002**, 360, 1233.
- [217] Cui S, Pu H, Mattson E C, Lu G, Mao S, Weinert M, Hirschmugl C J, Gajdardziska-Josifovska M and Chen J, *Nanoscale* **2012**, 4, 5887.
- [218] Acciarri M, Barberini R, Canevali C, Mattoni M, Mari C M, Morazzoni F, Nodari L, Polizzi S, Ruffo R, Russo U, Sala M and Scotti R, *Chemistry of Materials* **2005**, 17, 6167.
- [219] Slater B, Catlow C R A, Williams D E and Stoneham A M, *Chemical Communications* **2000**, 1235.
- [220] Wan Q and Wang T H, *Chemical Communications* **2005**, 3841.
- [221] Srivastava S, Jain K, Singh V N, Singh S, Vijayan N, Dilawar N, Gupta G and Senguttuvan T D, *Nanotechnology* **2012**, 23, 205501.
- [222] Deng S, Tjoa V, Fan H M, Tan H R, Sayle D C, Olivo M, Mhaisalkar S, Wei J and Sow C H, *Journal of the American Chemical Society* **2012**, 134, 4905.
- [223] Cui S M, Wen Z H, Mattson E C, Mao S, Chang J B, Weinert M, Hirschmugl C, Gajdardziska-Josifovska M and Chen J H, *Journal of Materials Chemistry A* **2013**, 1, 4462.
- [224] Cui S M, Mao S, Wen Z H, Chang J B, Zhang Y and Chen J H, *Analyst* **2013**, 138, 2877.

CURRICULUM VITAE

Shumao Cui

Place of birth: China

Education:

B.A., Shaanxi University of Science & Technology, July 2005

Major: Materials Engineering

M.S., Xi'an Jiaotong Univeristy, July 2008

Major: Materials Physics and Chemistry

Dissertation title: Tuning the Performance of Nanocarbon-based Gas Sensors through Nanoparticle Decoration

Research experience:

1. Nanocarbon-based hybrid gas sensors (2010-2013)

Research objective: to synthesize and characterize various nanoparticles (e.g., Ag, SnO₂) decorated nanocarbons, including carbon nanotubes (CNTs) and graphene for highly selective and sensitive gas sensors; to test the sensing performance for various gases (NO₂, NH₃, and H₂); to explore the possible sensing mechanisms.

2. One-dimensional tungsten oxide (2008-2010)

Research objective: to synthesize one-dimensional (1D) tungsten oxide crystals (wires, wire bundles, and tubes) by physical vapor deposition method using a mini-arc plasma as the heat source and to decipher the growth process.

3. PM304 self-lubricating composite (2007-2008)

Research objective: to synthesize high property PM304 self-lubricating composites with fine phases on Ni-based superalloy by a rapid sintered method; then to characterize the structure and investigate the lubricating properties of the as-prepared material.

4. Nanocrystalline CuCr, WCu alloy electrical contact materials (2006-2007)

Research objective: to fabricate superior nanocrystalline CuCr, WCu contact materials using ball-milling and hot-press method and to measure the electrical properties.

5. Porous metal materials (2005-2006)

Research objective: to fabricate porous metals using carbon as template.

Publications:

1. **S. M. Cui**, S. Mao, Z. H. Wen, J. B. Chang, Y. Zhang, J. H. Chen, *Analyst*, 2013, 138, 2877-2882.
2. **S. M. Cui**, Z. H. Wen, E. C. Mattson, S. Mao, J. B. Chang, M. Weinert, C. Hirschmugl, M. Gajdardziska-Josifovska and J. H. Chen, *J. Mater. Chem. A*, 2013, 1, 4462-4467.

3. Y. Zhang, **S. M. Cui**, J. B. Chang, L. E. Ocola and J. H. Chen, *Nanotechnology*, 2013, 24, 025503.
4. J. Chang, S. Mao, Y. Zhang, **S. Cui**, D. A. Steeber and J. Chen, *Biosens. Bioelectron.*, 2013, 42, 186-192.
5. **S. M. Cui**, H. H. Pu, E. C. Mattson, G. H. Lu, S. Mao, M. Weinert, C. J. Hirschmugl, M. Gajdardziska-Josifovska and J. H. Chen, *Nanoscale*, 2012, 4, 5887-5894.
6. **S. M. Cui**, H. H. Pu, G. H. Lu, Z. H. Wen, E. C. Mattson, C. Hirschmugl, M. Gajdardziska-Josifovska, M. Weinert and J. H. Chen, *ACS Appl. Mater. Inter.*, 2012, 4, 4898-4904.
7. **S. M. Cui**, E. C. Mattson, G. H. Lu, C. Hirschmugl, M. Gajdardziska-Josifovska and J. H. Chen, *J. Nanopart. Res.*, 2012, 14, 744.
8. Z. H. Wen, **S. M. Cui**, H. J. Kim, S. Mao, K. H. Yu, G. H. Lu, H. H. Pu, O. Mao and J. H. Chen, *J. Mater. Chem.*, 2012, 22, 3300-3306.
9. S. Mao, **S. M. Cui**, K. H. Yu, Z. H. Wen, G. H. Lu and J. H. Chen, *Nanoscale*, 2012, 11, 1275-1279.
10. Z. H. Wen, S. Q. Ci, F. Zhang, X. L. Feng, **S. M. Cui**, S. Mao, S. L. Luo, Z. He and J. H. Chen, *Adv. Mater.*, 2012, 24, 1399-1404.
11. S. Mao, **S. M. Cui**, G. H. Lu, K. H. Yu, Z. H. Wen and J. H. Chen, *J. Mater. Chem.*, 2012, 22, 11009-11013.
12. M. Mashock, K. H. Yu, **S. M. Cui**, S. Mao, G. H. Lu and J. H. Chen, *ACS Appl. Mater. Inter.*, 2012, 4, 4192-4199.
13. Z. H. Wen, **S. M. Cui**, H. H. Pu, S. Mao, K. H. Yu, X. L. Feng and J. H. Chen, *Adv. Mater.*, 2011, 23, 5445-5450.
14. Z. Bo, **S. M. Cui**, K. H. Yu, G. H. Lu, S. Mao and J. H. Chen, *Rev. Sci. Instrum.*, 2011, 82.
15. E. C. Mattson, H. H. Pu, **S. M. Cui**, M. A. Schofield, S. Rhim, G. H. Lu, M. J. Nasse, R. S. Ruoff, M. Weinert, M. Gajdardziska-Josifovska, J. H. Chen and C. J. Hirschmugl, *ACS Nano*, 2011, 5, 9710-9717.
16. S. Mao, K. H. Yu, **S. M. Cui**, Z. Bo, G. H. Lu and J. H. Chen, *Nanoscale*, 2011, 3, 2849-2853.
17. Z. Bo, K. H. Yu, G. H. Lu, **S. M. Cui**, S. Mao and J. H. Chen, *Energ. Environ. Sci.*, 2011, 4, 2525-2528.
18. **S. M. Cui**, G. H. Lu, S. Mao, K. H. Yu and J. H. Chen, *Chem. Phys. Lett.*, 2010, 485, 64-68.

Awards and Honors:

- ◆ 2012-2013 Graduate Dissertation Fellowship Award
- ◆ 2008-2013 Chancellor's Graduate Student Award in University of Wisconsin-Milwaukee (5 times)